Dynamics of shallow flows with and without background rotation

Please check the document version of this publication:

Dynamics of shallow flows
with and without background rotation

Dynamics of shallow flows with and without background rotation

PROEFSCHRIFT

door

Matías Durán Matute

geboren te Guadalajara, Mexico

Dit proefschrift is goedgekeurd door de promotor:

prof.dr.ir. G.J.F. van Heijst

Copromotoren:
dr.ir. L.P.J. Kamp
en
dr.ir. R.R. Trieling

A Inés
y Octavio

Contents

Chapter 1

Introduction

Large-scale flows in the ocean and the atmosphere possess three special characteristics: they are stratified in density; they are affected by the Earth's rotation; and they are shallow (their depth is much smaller than their horizontal length scales). The importance of these three characteristics resides partly in that they can enforce the two-dimensionality of flows. In other words, if any of these three characteristics is important enough, flows could present some special features characteristic of two-dimensional (2D) flows.

1.1   Characteristics of two-dimensional flows

Among the distinctive characteristics of 2D flows, the dual-cascade in 2D turbulence derived by Kraichnan (1967) might be the most renowned. This dual-cascade consists of a direct enstrophy cascade towards smaller scales and an inverse energy cascade towards larger scales. This property owes its existence to the absence of vortex stretching in 2D flows, which causes 2D turbulence to be essentially different from its three-dimensional (3D) counterpart in which the energy simply cascades from larger to smaller scales where it is dissipated by viscosity.

A significant numerical effort has been put into validating the prediction of the dual-cascade in 2D turbulence. The first direct numerical simulations of forced 2D turbulence aimed at confirming the existence of the dual-cascade were performed by Lilly (1969) in a periodic domain. In spite of the low resolution (64^2 grid points), the results of these simulations indicated the presence of the two cascades. With the increment of computing power, higher resolutions have been achieved allowing to better observe the inverse energy cascade or the direct enstrophy cascade (see e.g. Frisch & Sulem, 1984; Smith & Yakhot, 1993). Recently, Boffetta (2007) reported on simulations of statistically steady 2D turbulence in a periodic domain with a very high resolution (up to $16,348^2$ grid points) where the dual-cascade was clearly visible over two decades.

Figure 1.1 – *Picture of hurricane Bonnie over the Atlantic Ocean taken from the Endeavour in September 1992. NASA Photo ID: STS047-151-618.*

Another distinctive characteristic property of 2D flows, which is closely linked to the inverse energy cascade, is the process of self-organization, through which the flow organizes itself into large coherent structures or vortices, as first reported by Mattaeus & Montgomery (1980). The study of this process has led to theoretical predictions on the temporal evolution of vortex statistics in freely evolving 2D turbulence, which were initially derived by Batchelor (1969) in spectral space, and later reinterpreted in real space by Carnevale et al. (1991). These theories predict the evolution of the number, size, and strength of vortices in a 2D turbulent flow. Numerical simulations have also been set up to corroborate this theory, consistently yielding power laws as predicted by theory (Carnevale et al., 1991; Weiss & McWilliams, 1993; Dritschel, 1993; Clercx & Nielsen, 2000; Bracco et al., 2000). However, the exponents for the power laws depend on different factors such as the initial conditions (van Bokhoven et al., 2007).

Hurricanes are a notorious example of the large coherent structures formed in the atmosphere. They reach an average diameter of 500 km, while the height of the troposphere is merely in the order of 10 km. Figure 1.1 shows an image of hurricane Bonnie (September 1992) over the Atlantic Ocean and clearly illustrates the size and the shallowness of this type of flows.

Over the years, there has also been a large interest in the stability of 2D spatially periodic flows due to their high degree of symmetry. As for the case of 2D turbulence, the first theoretical studies were based on the idealized assumption of a perfectly 2D unbounded fluid and were independent of attempts to realize these flows in the laboratory. These studies predicted the types and thresholds of instabilities in Kolmogorov flows and arrays of vortices (Meshalkin & Sinai, 1961; Gotoh & Yamada, 1984; Takaoka, 1989; Sivashinsky & Yakhot, 1985).

For a more comprehensive overview about the topics treated in this introduction, the reader is referred to: Danilov & Gurarie (2000), Tabeling (2002), and Clercx & van Heijst (2009) for more details on 2D turbulence. Dolzhanskii et al.

(1990) and Thess (1992) provide a comprehensive overview about the stability of 2D spatially periodic flows. For an extensive overview on experiments in shallow layers, the reader is referred to Kellay & Goldburg (2002).

1.2 Laboratory experiments on two-dimensional flows

As theories and numerical simulations on 2D flows increased in number, there has been a growing interest on corroborating their results in the laboratory. Inspired by geophysical flows, experimentalists have used stratification (e.g. Maassen et al., 2003), background rotation (e.g Afanasyev & Wells, 2005), and shallow-layer configurations (e.g. Tabeling et al., 1991) in attempts to obtain 2D flows in the laboratory. Commonly, flows with only one of these characteristics are studied in the laboratory. In the present work, the attention is focused on the use of both shallowness and background rotation.

The two-dimensionality of shallow flows is usually attributed to vertical confinement. It is commonly thought that if the depth of the fluid is sufficiently small, the vertical velocities are restrained and that they can be neglected as compared to the horizontal velocities. Until recently, this argument, which rests in the continuity equation for incompressible fluids and dimensional analysis (see Pedlosky, 1987), was believed to ensure the 2D behavior of shallow flows.

The two-dimensionality of flows subjected to strong background rotation is usually attributed to the Taylor–Proudman theorem, which states that strong rotation reduces the velocity gradients in the direction parallel to the axis of rotation. However, this theorem only applies strictly to quasi-stationary flows and does not predict if a flow that is initially 3D will become 2D. Even though the formation of columnar structures as predicted by the Taylor–Proudman theorem was observed already more than 150 year ago (see Velasco Fuentes, 2009), the mechanism through which flows subjected to background rotation become 2D still attracts much interest (see e.g. Staplehurst et al., 2008).

Moreover, no perfect 2D flow for the study of 2D turbulence or the stability of 2D periodic flows can be realized in the laboratory. This is due, for example, to the presence of solid boundaries and free-surface deformations. For this reason, the term *quasi-two-dimensional* (Q2D) has been introduced to describe a flow that is not perfectly 2D but can still be approximately modeled by the 2D vorticity equation where the vertical motions are parametrized. In general, the use of both thin-layer configurations and background rotation to obtain Q2D flows in the laboratory has shown promising results, but many critical questions about the three-dimensionality of these flows remain unanswered.

1.2.1 Shallow flows

The first experimental studies on shallow Q2D flows where aimed at studying the stability of 2D periodic flows (Bodarenko et al., 1979; Tabeling et al., 1987). In these experiments, a thin electrolytic layer was used as a working fluid. To generate the desired flow, an array of magnets was positioned below the tank containing the electrolyte, and an electric current was driven through the fluid. The interaction between the magnetic field and the electric current generates a Lorentz force that drives the flow. In spite of the shallow layer configuration, the results of these experiments did not confirm the theoretical predictions for the stability of 2D periodic flows. This disagreement is due to the effect of the boundaries in the experiments, that where not taken into account in the theoretical models (Bodarenko et al., 1979; Sommeria, 1986; Dolzhanskiy, 1987). Hence, a new theory was derived, that incorporates the effects of these boundaries (specially friction at the bottom), showing good agreement with experimental results (Thess, 1992).

In the study of the inverse energy cascade, the pioneering experimental work by Sommeria (1986) in an electrically driven thin layer of mercury deserves special mentioning. This work was the first attempt to observe the inverse energy cascade in the laboratory, and probably, it also inspired later experimental work in shallow layers of electrolytes. In these experiments, an inverse energy cascade was found spanning for about half a decade, and in addition, the process of self-organization was clearly observed. The setup consisted of a tank filled with a thin layer of mercury and positioned in the gap of an electromagnet producing a homogeneous vertical magnetic field. At the bottom of the tank, a squared network of electric sources and sinks was placed. Due to the interaction of the magnetic field and the electric current through the fluid, a Lorentz force sets the fluid into motion. However, due to the properties of mercury, the two-dimensionality of the flow is not only enforced by the small fluid depth, but more importantly, by the action of the strong magnetic field on the fluid (Sommeria, 1982).

In the early 80's, experiments on turbulence in soap films were performed by Couder (1984). An extreme shallowness is achieved in soap films since their thickness is in the order of micrometers while the horizontal length scales of the flow are of the order of millimeters or centimeters, depending on the generation mechanism. In the experiments, a large number of vortices were created by towing a comb through the film. After the comb passed, a strong interaction between the vortices was observed. In particular, the merging of like-sign vortices, which is associated with the process of self-organization in 2D turbulence, was clearly visible. In addition, different theoretical predictions for 2D turbulence have been corroborated in recent experiments on soap films where the soap film is in motion and passes through a comb. In fact, through this type of soap films experiments, the exponent of the direct enstrophy cascade was first validated experimentally for decaying turbulence (Kellay et al., 1995), and the dual-cascade scenario was confirmed for forced turbulence (Rutgers, 1998).

Even though turbulent soap-film flows show good agreement with 2D turbu-

lence theory, there are known shortcomings that generate concern about their degree of two-dimensionality. Such shortcomings are, for example, variations in the film thickness and the effects of air drag (Kellay & Goldburg, 2002).

In the 90's, experiments on shallow layers of electrolytes were performed to test the theoretical predictions for 2D turbulence. In these experiments, the predictions on the scaling of vortex statistics presented by Carnevale et al. (1991) were first tested by Tabeling et al. (1991). It was observed that bottom friction had an important effect on the evolution of the flow, as it was previously observed for experiments on the stability of periodic 2D flows. This observation resulted in a growing interest in the role of boundaries on the evolution of 2D turbulence (van Heijst & Clercx, 2009b; Clercx & van Heijst, 2009).

To minimize the effect of bottom friction, a stably stratified two-layer fluid has been used. For example, Tabeling and co-workers used it in an attempt to validate the scaling of the vortex statistics predicted by Carnevale et al. (1991) (Hansen et al., 1998), and to measure the inverse energy cascade (Paret & Tabeling, 1997). Since then, this two-layer setup has been regarded as the best setup to study Q2D flows, and has been regularly used until now. For example, the formation of a condensate was observed recently in a two-layer setup where the fluid was continuously forced (Shats et al., 2005).

The two-dimensionality of shallow flows has been strongly tested recently. In a two-layer configuration (an electrolytic layer at the bottom and a non-conductive layer above), Paret et al. (1997) measured a negligible momentum exchange between the layers, and thus, they concluded that the flow can be regarded as Q2D. However, the dependence of the two-dimensionality on the Reynolds number, which was later suggested by Satijn et al. (2001), was not taken into account.

Thanks to the development of new experimental techniques, namely Stereoscopic Particle Image Velocimetry (SPIV), all three velocity components have been measured at different planes inside shallow flows. This type of velocity measurements inside dipolar vortices generated electromagnetically — as in the experiments on Q2D turbulence mentioned above — have revealed larger than expected vertical velocities and complicated 3D structures for very shallow layers (Akkermans et al., 2008a,b) and even in a two-layer configuration (Akkermans et al., 2010). In addition, for decaying turbulence in a shallow fluid layer, it was found that these flows are characterized by long-lived meandering currents, which are associated with 3D motions (Cieslik et al., 2009). These recent studies question the assumption of the two-dimensionality of shallow fluid layers.

1.2.2 Rotating flows

In flows subjected to background rotation, the formation of columnar structures was observed more than 150 years ago by Lord Kelvin (see the historical note by Velasco Fuentes, 2009) anticipating the analytical results of what is now known as the Taylor–Proudman theorem. Even though this theorem is only strictly valid for stationary flows, it has been observed that strong rotation tends to organize

turbulent flows in columnar vortices (Hopfinger, 1982). In addition, it has been shown that strong rotation suppresses the dissipation of the turbulent kinetic energy (Jacquin et al., 1990) and promotes the flux of kinetic energy towards large scales (Morize et al., 2005).

Besides the experimental work on rotating turbulence, there is an ample body of work, which is mainly motivated by geophysical applications, on the evolution of vortices and other structures in flows subjected to background rotation. In this work, the formation of columnar vortical structures has been clearly observed, with these structures showing good agreement with 2D models (see e.g. the work by Kloosterziel & van Heijst, 1992 or the review by van Heijst & Clercx, 2009a).

In spite of the agreement between rotating turbulence and 2D theories, and the formation of columnar structures in rotating flows, background rotation has a few limitations when used to produce Q2D flows in the laboratory. For example, there are asymmetries between cyclonic and anticyclonic vortices (Zavala Sansón & van Heijst, 2000; Morize et al., 2005), and there are secondary motions driven by the Ekman boundary layers found next to the boundaries perpendicular to the rotation axis (see Pedlosky, 1987). More importantly, the question why a 3D flow becomes Q2D when subjected to background rotation remains. Although most researchers agree that inertial oscillations play a crucial role in the formation of the columnar structures, and although linear dynamics are predominant during this process, the importance of non-linear dynamics is still unclear (Davidson et al., 2006; Staplehurst et al., 2008). For a single vortex tube which is initially perturbed and subjected to strong background rotation, the vortex relaxes rapidly to a columnar structure for small perturbation due to the inertial oscillations. When the vortex perturbation is large, non-linear inertial oscillations tend to break the tube before it becomes a columnar structure (Carnevale et al., 1997).

1.3   Aim and outline of this thesis

The present work furthers the understanding of the effects of shallowness and background rotation on the two-dimensionality of flows. To achieve this goal, it was necessary to find appropriate ways to determine when a flow can be considered as Q2D. For these purposes, we study the evolution and dynamics of simple vortical structures (monopolar and dipolar vortices), which are considered as the building blocks of more complicated flows such as 2D turbulence.

In Chapter 2, some theoretical aspects, that are key to the understanding of this study, are introduced before presenting the main results of this work. These theoretical aspects are concerned with the definition of 2D flows, and the different arguments commonly used to justify the two-dimensionality of both shallow flows and flows subjected to background rotation.

In Chapter 3, we revise the usual argument used to justify the two-dimensionality of shallow flows by analytically studying a decaying axisymmetric swirl flow (i.e. a monopolar vortex). In contrast with this argument based on scale analysis

of the continuity equation, we show that the dynamics of the flow is crucial to determine if a shallow flow can be considered as Q2D. In Chapter 4, the study of axisymmetric swirl flows is continued with the inclusion of background rotation. This chapter presents a systematic analysis of the effects of both shallowness and rotation on the degree of two-dimensionality of decaying vortical structures.

Chapter 5 is concerned with the dynamics of inertial oscillations in confined decaying axisymmetric vortices subjected to background rotation. Inertial oscillations are an important 3D component of flows studied in this thesis since they can have a significant effect on the flow evolution.

The thesis continues with the study of a dipolar vortex. Chapter 6 is devoted to the case of decaying dipolar vortices, while stationary dipolar structures without background rotation are studied in Chapter 7 and with background rotation in Chapter 8. The main objective in Chapter 6 is to generalize the results obtained in Chapter 3 to more complicated vortical structures through the use of both numerical simulations and laboratory experiments. On the other hand, Chapters 7 and 8 are aimed at determining the range of validity of the use of linear damping to parametrize the vertical dependence of the flow, i.e. the validity of assuming the flow as Q2D. In these chapters, the stationary dipolar structure is generated using time-independent electromagnetic forcing in the laboratory.

Finally, the main conclusions are summarized in Chapter 9.

Chapter 2

Theoretical preliminaries

The current chapter presents some theoretical background relevant for the understanding of this thesis. This background is concerned with the relevant equations, the definitions of two-dimensional (2D) flows and quasi-two-dimensional (Q2D) flows as understood in this thesis, and a description of previous attempts to quantify the degree of two-dimensionality in different flows.

2.1 Fundamental equations

In the present thesis, we consider the motion of an incompressible Newtonian fluid. The equations governing this motion are those stating the conservation of momentum (the Navier–Stokes equation) and mass (the continuity equation), which can be written as

$$\frac{\partial \boldsymbol{v}}{\partial t} + \boldsymbol{v} \cdot \boldsymbol{\nabla} \boldsymbol{v} = -\frac{\boldsymbol{\nabla} p}{\rho} + \nu \nabla^2 \boldsymbol{v} + \frac{\boldsymbol{F}}{\rho}, \tag{2.1}$$

$$\boldsymbol{\nabla} \cdot \boldsymbol{v} = 0, \tag{2.2}$$

respectively, where $\boldsymbol{v}$ is the fluid velocity; t is time; ν is the kinematic viscosity of the fluid; p is the pressure; ρ is the uniform density of the fluid; and $\boldsymbol{F}$ are external body forces (per unit volume).

In (2.1), the material derivative of the velocity $\mathrm{D}\boldsymbol{v}/\mathrm{D}t = \partial \boldsymbol{v}/\partial t + \boldsymbol{v} \cdot \boldsymbol{\nabla} \boldsymbol{v}$ expresses the acceleration associated with a given fluid element, where $\boldsymbol{v} \cdot \boldsymbol{\nabla} \boldsymbol{v}$ is known as the convective acceleration. On the right hand side of (2.1), the mass per unit volume is given by the density ρ, while the different forces acting on a fluid element are the pressure gradient force $\boldsymbol{\nabla} p$, the viscous forces arising from viscous stresses $\nu \nabla^2 \boldsymbol{v}$, and the external body forces $\boldsymbol{F}$, which result from the fluid being placed in a certain force field.

9

It is sometimes convenient to take the curl of (2.1) to rewrite this equation in terms of the vorticity $\boldsymbol{\omega} = \boldsymbol{\nabla} \times \boldsymbol{v}$, which yields

$$\frac{\mathrm{D}\boldsymbol{\omega}}{\mathrm{D}t} = (\boldsymbol{\omega} \cdot \boldsymbol{\nabla})\boldsymbol{v} + \nu\nabla^2\boldsymbol{\omega} + \frac{1}{\rho}\boldsymbol{\nabla} \times \boldsymbol{F}. \tag{2.3}$$

The first term on the right hand side, $(\boldsymbol{\omega} \cdot \boldsymbol{\nabla})\boldsymbol{v}$, is known as the *vortex stretching term* and represents the stretching and tilting of vortex lines.

To understand the physical mechanism of vortex stretching, consider a thin vortex tube with vorticity $\boldsymbol{\omega}$; let $v_\parallel$ be the velocity component parallel to the vortex tube and s a coordinate measured along the tube. Then,

$$(\boldsymbol{\omega} \cdot \boldsymbol{\nabla})v_\parallel = |\boldsymbol{\omega}|\frac{\mathrm{d}v_\parallel}{\mathrm{d}s}. \tag{2.4}$$

If $\mathrm{d}v_\parallel/\mathrm{d}s > 0$, the vortex tube is stretched, and from (2.3), we see that $|\boldsymbol{\omega}|$ increases. This mechanism is responsible for the formation of small intense vorticity filaments in 3D flows.

Now, let $v_\perp$ be a velocity component perpendicular to the vortex tube, so that

$$(\boldsymbol{\omega} \cdot \boldsymbol{\nabla})v_\perp = |\boldsymbol{\omega}|\frac{\mathrm{d}v_\perp}{\mathrm{d}s}. \tag{2.5}$$

This term describes the tilting of the vortex tube in the direction of $v_\perp$ by the velocity gradient $\mathrm{d}v_\perp/\mathrm{d}s$. From (2.3), it is possible to see that the tilting of a vortex tube in the direction of $v_\perp$ will generate vorticity in this direction.

2.2 Two-dimensional flows

In this thesis, we define 2D flows as flows governed on a plane by the vorticity equation

$$\frac{\mathrm{D}\omega_n}{\mathrm{D}t} = \nu\nabla^2\omega_n + \frac{1}{\rho}(\boldsymbol{\nabla} \times \boldsymbol{F}) \cdot \hat{\boldsymbol{n}}, \tag{2.6}$$

where $\hat{\boldsymbol{n}}$ is the unit vector perpendicular to the plane of motion, and $\omega_n = \boldsymbol{\omega} \cdot \hat{\boldsymbol{n}}$ is the vorticity component perpendicular to that plane. Note that both vortex stretching and tilting are now absent from (2.6). This is the hallmark of 2D flows. In other words, this is at the base of the inverse energy cascade and the process of self-organization in 2D turbulence. In 2D flows, ω_n is point-wise conserved along Lagrangian trajectories for an inviscid fluid ($\nu = 0$) in the absence of nonconservative body forces ($\boldsymbol{\nabla} \times \boldsymbol{F} = 0$).

Consider now a flow in Cartesian coordinates (x, y, z) for which the velocity is given by $\boldsymbol{v} = (v_x, v_y, v_z)$ and the vorticity by $\boldsymbol{\omega} = (\omega_x, \omega_y, \omega_z)$. If the velocity is independent of the z-coordinate, so that $\boldsymbol{v} = \boldsymbol{v}(x, y, t)$, the evolution of the

vorticity component in the z-direction is governed by (2.6), where now $\omega_n = \omega_z$, and by the continuity equation

$$\frac{\partial v_x}{\partial x} + \frac{\partial v_y}{\partial y} = 0. \tag{2.7}$$

In the literature about 2D turbulence, horizontal planar flows on the (x,y)-plane, for which $\boldsymbol{v} = [v_x(x,y,t), v_y(x,y,t), 0]$ and $\boldsymbol{\omega} = [0, 0, \omega_z(x,y,t)]$, are usually considered (see e.g. the review by Clercx & van Heijst, 2009). Note, however, that it is not necessary that $v_z = 0$ for the evolution of ω_z to be governed by (2.6) and (2.7); instead, it is sufficient that $\partial v_z / \partial z = 0$.

A 2D flow could be defined in more general terms as a flow in which the velocity depends only on two spatial coordinates. For illustration purposes, we consider an arbitrary reference frame defined by the unit vectors $\{\boldsymbol{e}_1, \boldsymbol{e}_2, \boldsymbol{e}_3\}$, where the position of a point is defined by the vector $\boldsymbol{x} = (x_1, x_2, x_3)$, and the velocity by the vector $\boldsymbol{v} = (v_1, v_2, v_3)$. If $\boldsymbol{v} = \boldsymbol{v}(x_1, x_2, t)$, there is no vortex stretching in the x_3-direction, i.e.

$$\omega_3 \frac{\partial v_3}{\partial x_3} = 0. \tag{2.8}$$

However, the evolution of ω_3 can still be influenced by vortex tilting. This is the case, for example, for azimuthally symmetric swirl flows in cylindrical coordinates for which the velocity depends only on the vertical and radial coordinates. In the current thesis, these flows will not be referred to as 2D flows.

2.3 The Coriolis force and the Taylor–Proudman theorem

For flows subjected to background rotation, it is usually convenient to consider the motion relative to the rotating frame of reference. If the frame rotates at a steady angular velocity $\boldsymbol{\Omega}$, the fluid motion is governed by the Navier–Stokes equation in the rotating frame

$$\frac{\partial \boldsymbol{v}}{\partial t} + \boldsymbol{v} \cdot \boldsymbol{\nabla} \boldsymbol{v} + 2\boldsymbol{\Omega} \times \boldsymbol{v} = -\frac{\boldsymbol{\nabla} p}{\rho} - \boldsymbol{\Omega} \times (\boldsymbol{\Omega} \times \boldsymbol{x}) + \nu \nabla^2 \boldsymbol{v} + \frac{\boldsymbol{F}^*}{\rho}, \tag{2.9}$$

and the continuity equation (2.2), with $\boldsymbol{x}$ the position vector and $\boldsymbol{F}^*$ other external body forces. The effects of background rotation are represented by the Coriolis acceleration $(2\boldsymbol{\Omega} \times \boldsymbol{v})$ and the centrifugal acceleration $[-\boldsymbol{\Omega} \times (\boldsymbol{\Omega} \times \boldsymbol{x})]$. The latter term can be written as the gradient of a scalar

$$-\boldsymbol{\Omega} \times (\boldsymbol{\Omega} \times \boldsymbol{x}) = -\nabla \left(\frac{1}{2} |\boldsymbol{\Omega} \times \boldsymbol{x}|^2 \right), \tag{2.10}$$

and therefore, can be incorporated in the pressure gradient $\boldsymbol{\nabla} P = \boldsymbol{\nabla}(p - |\boldsymbol{\Omega} \times \boldsymbol{x}|^2/2)$, where P is commonly referred to as the reduced pressure. Then, the momentum equation becomes

$$\frac{\partial \boldsymbol{v}}{\partial t} + \boldsymbol{v} \cdot \boldsymbol{\nabla} \boldsymbol{v} + 2\boldsymbol{\Omega} \times \boldsymbol{v} = -\frac{\boldsymbol{\nabla} P}{\rho} + \nu \nabla^2 \boldsymbol{v} + \frac{\boldsymbol{F}^*}{\rho}. \tag{2.11}$$

For sufficiently strong rotation so that the viscous forces, the convective acceleration, and the external body forces can be neglected with respect to the Coriolis acceleration, (2.11) reduces to

$$\rho 2\boldsymbol{\Omega} \times \boldsymbol{v} = -\boldsymbol{\nabla} P \tag{2.12}$$

for quasi-steady motions. In this case, the flow is governed by a balance of the Coriolis force and the pressure gradient force, which is known as the geostrophic balance. Taking the curl of (2.12) results in the so-called Taylor–Proudman theorem

$$(\boldsymbol{\Omega} \cdot \nabla)\boldsymbol{v} = 0, \tag{2.13}$$

which states that the velocity is independent of the coordinate parallel to the direction of the rotation axis.

To facilitate the physical understanding of the Taylor–Proudman theorem, it is convenient to consider a Cartesian coordinate system rotating at a rate $\boldsymbol{\Omega} = (0, 0, \Omega)$. In this case, each velocity component is independent of the vertical coordinate

$$\frac{\partial \boldsymbol{v}}{\partial z} = 0, \tag{2.14}$$

which is a sufficient condition for the absence of both vortex stretching and tilting in the evolution of ω_z, and hence, to consider the flow in the (x, y)-plane as a 2D flow.

2.4   The two-dimensionality of shallow flows

Traditionally, the two-dimensionality of shallow flows is founded on a scale analysis of the continuity equation for an incompressible fluid (2.2), which reads

$$\frac{\partial v_x}{\partial x} + \frac{\partial v_y}{\partial y} = -\frac{\partial v_z}{\partial z}, \tag{2.15}$$

in Cartesian coordinates, where z is the vertical coordinate and $\boldsymbol{v} = (v_x, v_y, v_z)$ is the fluid velocity. If L is a typical horizontal length scale of the flow, and H is a typical vertical length scale (commonly the depth of the fluid), then (2.15) implies that

$$\frac{[v_x]}{L} \sim \frac{[v_y]}{L} \sim \frac{[v_z]}{H}, \tag{2.16}$$

where the brackets denote the order of magnitude of the enclosed quantity. Consequently,

$$[v_z] \sim \frac{H}{L}[v_x] \sim \frac{H}{L}[v_y]. \tag{2.17}$$

This suggests that for shallow flows ($H/L \ll 1$) the vertical velocities are much smaller than the horizontal velocities and that the ratio of vertical to horizontal velocities scales with the aspect ratio $\delta \equiv H/L$. This argument is used to neglect the vertical velocities in shallow flows and consider such flows as 2D.

In contrast with the Taylor–Proudman theorem, the argument to consider shallow flows as 2D only implies something about the magnitude of the vertical velocity. Meanwhile, its vertical gradient is assumed to be of the order of H^{-1}. However, we must remember that the hallmark of 2D flows is the absence of vortex stretching, which in the z-direction is written as

$$\omega_z \frac{\partial v_z}{\partial z},$$

and unless $v_z = 0$, the importance of this term is given by the vertical gradient of the vertical velocity.

2.5   Quasi-two-dimensional flows

In reality, neither background rotation nor shallowness can create perfect 2D flows in the laboratory. This is due, for example, to the presence of boundaries (van Heijst & Clercx, 2009b).

For flows subjected to strong background rotation (with the rotation axis in the vertical direction), the presence of horizontal no-slip boundaries is a clear obstacle for the formation of perfect two-dimensional flows since a geostrophic flow, which satisfies the Taylor–Proudman theorem, cannot satisfy the conditions at the boundaries. Therefore, a thin boundary layer must exist between the geostrophic flow and the solid boundary where $\partial \boldsymbol{v}/\partial z \neq 0$. Inside this type of boundary layers, known as Ekman boundary layers, there is a balance between the Coriolis force and viscous forces, resulting in a layer with a typical thickness $(\nu/\Omega)^{1/2}$. Furthermore, Ekman boundary layers have the particularity that they pump fluid from the boundary layer into the geostrophic interior or vice versa. This process is described by the Ekman suction condition that states that in the interior the vertical velocity is

$$v_z(x,y) = \frac{1}{2}\mathrm{Ek}^{1/2}\omega_z(x,y) \tag{2.18}$$

with $\mathrm{Ek} \equiv \nu/(\Omega H^2)$ the Ekman number. Other 3D phenomena found in rotating flows are inertial oscillations (Thomson, 1880) and 3D vortex instabilities such as the centrifugal instability (Kloosterziel & van Heijst, 1991).

Shallow flows are not perfectly 2D simply because of their finite thickness — which translates into a finite magnitude of the vertical velocities — and the presence of horizontal boundaries — which play a crucial role in the flow evolution (van Heijst & Clercx, 2009b). For example, if a flow is bounded by a solid boundary at the bottom and a free surface, there will be a vertical gradient in the horizontal velocity; by continuity there will also be a vertical gradient in the vertical velocity, and hence, vortex stretching in the z-direction.

However, in some special cases it is possible to parametrize or neglect the three-dimensional motions. For these cases, the term *quasi-two-dimensional* (Q2D) was coined. Dolzhanskii et al. (1992) defined a Q2D flow as a flow which is governed on a plane by the vorticity equation

$$\frac{\mathrm{D}\omega_n}{\mathrm{D}t} = -\lambda\omega_n + \frac{1}{\rho}(\boldsymbol{\nabla} \times \boldsymbol{F}) \cdot \hat{\boldsymbol{n}}, \tag{2.19}$$

where $\hat{\boldsymbol{n}}$ is the unit vector perpendicular to the plane of motion, and $\omega_n = \boldsymbol{\omega} \cdot \hat{\boldsymbol{n}}$ is the vorticity component perpendicular to that plane. In (2.19), the viscous terms or the vortex stretching terms are replaced by a linear damping term $-\lambda\omega_n$ where λ is a constant, which depends on the underlying physics. For example, for a flow confined by a no-slip bottom and subjected to strong background rotation (with the rotation vector pointing in the same direction as $\hat{\boldsymbol{n}}$), $\lambda = (\Omega\nu)^{1/2}/H$ with H the depth of the fluid. It has been observed that linear damping can play an important role in flows governed by (2.19). For example, it modifies the energy spectra of continuously forced 2D turbulence (Boffetta et al., 2005). However, many flow features of freely evolving 2D turbulence are independent of the value of λ (Clercx et al., 2003).

2.6 Quantifying the degree of two-dimensionality of flows

Recently, the two-dimensionality of shallow flows, and hence, the validity of (2.19) to describe such flows have been questioned. This has promoted many attempts aimed to quantify the degree of two-dimensionality of shallow flows, in particular shallow vortices.

For the shallow flows considered in the current thesis, the horizontal length scales are much larger than the fluid depth, and the axis of rotation is along the vertical direction. Hence, it can be expected a priori that the flow will behave as a 2D flow on a horizontal cross section. It is of interest then to quantify the degree of two-dimensionality of the flow in a horizontal plane, i.e. to quantify how close is the flow behavior on a horizontal plane to the behavior of a perfect 2D flow.

For shallow flows, it is natural to measure the relative magnitude of the vertical velocities as compared to the horizontal velocities, since the usual argument used to justify the two-dimensionality of these flows suggests that the vertical velocities should be negligible as compared to the horizontal velocities. A quantity commonly

found in the literature is the normalized kinetic energy associated with the vertical velocity component. For an axisymmetric monopolar vortex, Satijn et al. (2001) defined the ratio

$$Q_z(t) = \frac{\displaystyle\int_V v_z^2(r, z, t)\mathrm{d}V}{\displaystyle\int_V v_\theta^2(r, z, t)\mathrm{d}V}, \tag{2.20}$$

where the kinetic energy associated with the vertical velocity components v_z is integrated over the volume V and normalized with the kinetic energy associated with the azimuthal velocity component v_θ.

In dipolar vortices, it has been found more convenient to consider the kinetic energy associated with the vertical velocity component in a horizontal cross-section $z = z_0$ and normalize it with the kinetic energy associated with the horizontal velocity components:

$$Q_z(t; z_0) = \frac{\displaystyle\int_S v_z^2(x, y, z = z_0, t)\mathrm{d}x\mathrm{d}y}{\displaystyle\int_S [v_x^2(x, y, z = z_0, t) + v_y^2(x, y, z = z_0, t)]\mathrm{d}x\mathrm{d}y}, \tag{2.21}$$

where S is the surface of integration (Akkermans et al., 2008a,b). Sous et al. (2005) considered a similar quantity on a vertical cross-section.

Another popular quantity to characterize the two-dimensionality of flows is the horizontal divergence. For example, Sous et al. (2005) and Akkermans et al. (2008a,b) considered the normalized horizontal divergence integrated over a horizontal plane. The advantage of considering the horizontal divergence instead of the kinetic energy associated with the vertical velocity component is that the vortex stretching in the vertical direction is directly proportional to the former.

The usual way to determine if a flow can be considered as Q2D is to calculate the values of the previously mentioned quantities and to compare these values with a certain threshold below which the flow is said to be Q2D. However, Akkermans et al. (2008a) already realized that this approach has several shortcomings. For example, the value of the different quantities depends on the size of the integration domain and the position of the plane (i.e. the value of z_0) where the quantities are evaluated. Furthermore, it was noted that the horizontal divergence suggests deviations from Q2D behavior in a different way as the normalized kinetic energy associated with the vertical velocity. Finally, the information given by integral quantities is limited to average values in the whole flow domain, and do not reveal the local importance of 3D motions in different flow regions.

Satijn et al. (2001) considered another criterion, in which the deformation of the radial profile of an axisymmetric monopolar vortex is compared to the initial radial distribution. Since this deformation is directly due to vortex stretching, it directly quantifies the effects of 3D motions on the evolution of the vortex.

However, this quantity grows continuously in time rendering the definition of a threshold not a trivial task.

Strangely, an approach similar to the one just mentioned to quantify the two-dimensionality of vortices has not been used for vortices subjected to background rotation. However, 3D effects in this type of flows — e.g. 3D instabilities (Kloosterziel & van Heijst, 1991), the non-linear effects due to Ekman pumping (Zavala Sansón & van Heijst, 2000), and the effects of free-surface deformations (Maas, 1993) — have been extensively studied.

Chapter 3

Decaying axisymmetric swirl flows[i]

3.1 Introduction

As doubts about the two-dimensionality of shallow flows emerge (Satijn et al., 2001; Akkermans et al., 2008a,b; Cieslik et al., 2009), it is just natural to revise the usual argument used to justify considering all shallow flows as Q2D. To test this argument, which was presented in Section 2.4, we focus on shallow axisymmetric swirl flows like monopolar vortices, which are considered as the building blocks of Q2D turbulence. The flow, on top of a no-slip horizontal bottom, is initialized with a specific azimuthal velocity distribution and is subsequently left to evolve freely. It is well known that in such a swirling flow a secondary flow arises with both radial and vertical velocity components[ii]. Of particular interest is the scaling, commonly used to quantify the degree of two-dimensionality of the flow, of both the radial and vertical velocities with respect to the primary azimuthal motion.

The degree of two-dimensionality of a shallow axisymmetric monopolar vortex has been previously quantified in numerical simulations using three criteria based on: (i) the ratio of the kinetic energies associated with the radial and the azimuthal velocity components, (ii) the ratio of the kinetic energies associated with the vertical and the azimuthal velocity components, and (iii) the deformation of the vorticity profile as compared to the initial profile. It was found that the degree of two-dimensionality depends not only on the aspect ratio but also on the Reynolds number (Satijn et al., 2001). This explains partly why some shallow

---

[i]The contents of this chapter have been adopted from Duran-Matute et al. (2010) with minor modifications.

[ii]Einstein (1926) presented the solution of the tea leaves paradox (why do tea leaves at the bottom of a tea cup migrate to the center of the cup after the water is stirred) and explained the formation of meanders in the course of rivers (Baer's law) by the presence of secondary motions in those flows.

flows behave in a Q2D way, while some others do not, and it is also a sign that the scaling of the vertical velocity cannot be simply derived from geometrical arguments based on the continuity equation. Clearly, it is still not well understood why some shallow flows do not behave in a Q2D way.

In this chapter, the velocity components are expanded in powers of the aspect ratio δ, and at lowest order a simplified version of the axisymmetric Navier–Stokes equations is found for shallow swirl flows where advection and radial diffusion are neglected. Then, these equations are solved analytically for a realistic initial azimuthal velocity profile. The analytical results are then compared with numerical simulations of the full axisymmetric Navier–Stokes equations. This allows us to derive the proper scaling for shallow axisymmetric flows and to find the range of validity for this scaling.

The chapter is organized as follows: Section 3.2 presents the governing equations and the geometry pertinent to the problem. In Section 3.3, we present a perturbation approach leading in lowest order to a simplified Navier–Stokes equation that is solved analytically in Section 3.4. Section 3.5 is devoted to the results from numerical simulations of a Lamb–Oseen monopolar vortex, which serve to quantify the range of validity of the analytical results. Finally, the conclusions are presented in Section 3.6.

3.2   Governing equations and geometry

We consider a freely evolving flow governed by the Navier–Stokes equations

$$\frac{\mathrm{D}\boldsymbol{v}}{\mathrm{D}t} = -\frac{1}{\rho}\boldsymbol{\nabla}p + \nu\nabla^2\boldsymbol{v} \tag{3.1}$$

and the continuity equation for an incompressible fluid

$$\boldsymbol{\nabla}\cdot\boldsymbol{v} = 0, \tag{3.2}$$

where $\mathrm{D}/\mathrm{D}t$ is the material derivative, $\boldsymbol{v}$ is the velocity, ν is the kinematic viscosity, p is the pressure, and ρ is the density of the fluid.

Since we are interested in axisymmetric swirl flows, it is convenient to use cylindrical coordinates (r, θ, z); the velocity is then written as $\boldsymbol{v} = (v_r, v_\theta, v_z)$, and the vorticity as $\boldsymbol{\omega} = \boldsymbol{\nabla} \times \boldsymbol{v} = (\omega_r, \omega_\theta, \omega_z)$.

The fluid is vertically confined by a no-slip bottom ($\boldsymbol{v} = 0$ at $z = 0$) and a rigid, flat surface (at $z = H$) that is assumed to be stress-free; see figure 3.1.

The flow is initialized with a particular axisymmetric azimuthal velocity profile $v_\theta(r, z, t = 0) \neq 0$ while $v_r(r, z, t = 0) = v_z(r, z, t = 0) = 0$; afterwards, the flow is left to freely evolve.
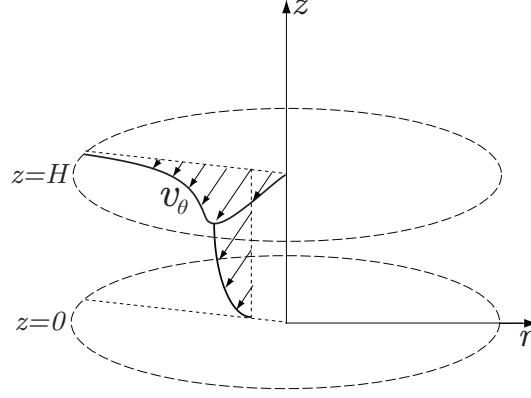
Figure 3.1 – *Sketch of the problem's geometry.*

3.3 Shallow swirl-flow approximation

In order to non-dimensionalize the governing equations (3.1) and (3.2), we introduce the following nondimensional variables denoted by primes:

$$t' = \frac{\nu}{H^2}t, \qquad r' = \frac{r}{L_0}, \qquad z = \frac{z}{H},$$

$$[v_\theta', v_r', v_z'] = \frac{1}{U}[v_\theta, v_r, v_z], \qquad \omega_\theta' = \frac{H}{U}\omega_\theta,$$

where U is a typical velocity scale of the flow, and L_0 is a typical radial length scale.

Since we consider a flow with azimuthal symmetry ($\partial/\partial\theta = 0$), we can rewrite (3.1) and (3.2) in terms of v_θ' and ω_θ', so that we obtain

$$\frac{\partial v_\theta'}{\partial t'} + \delta^2 \mathrm{Re}\left(v_r'\frac{\partial v_\theta'}{\partial r'} + \frac{v_\theta' v_r'}{r'}\right) + \delta\,\mathrm{Re}\,v_z'\frac{\partial v_\theta'}{\partial z'}$$
$$= \delta^2\left[\frac{\partial^2 v_\theta'}{\partial r'^2} + \frac{\partial}{\partial r'}\left(\frac{v_\theta'}{r'}\right)\right] + \frac{\partial^2 v_\theta'}{\partial z'^2}, \tag{3.3}$$

$$\frac{\partial \omega_\theta'}{\partial t'} + \delta^2 \mathrm{Re}\left(v_r'\frac{\partial \omega_\theta'}{\partial r'} - \frac{\omega_\theta' v_r'}{r'}\right) + \delta\,\mathrm{Re}\,v_z'\frac{\partial \omega_\theta'}{\partial z'} - \delta^2\mathrm{Re}\frac{1}{r'}\frac{\partial v_\theta'^2}{\partial z'}$$
$$= \delta^2\left[\frac{\partial^2 \omega_\theta'}{\partial r'^2} + \frac{\partial}{\partial r'}\left(\frac{\omega_\theta'}{r'}\right)\right] + \frac{\partial^2 \omega_\theta'}{\partial z'^2}, \tag{3.4}$$

$$\delta\frac{1}{r'}\frac{\partial}{\partial r'}(r'v_r') + \frac{\partial v_z'}{\partial z'} = 0, \tag{3.5}$$

$$\omega_\theta' = \frac{\partial v_r'}{\partial z'} - \delta\frac{\partial v_z'}{\partial r'}, \tag{3.6}$$

with $\delta \equiv H/L_0$ the aspect ratio and $\mathrm{Re} \equiv UL_0/\nu$ the Reynolds number. To simplify notation, the primes will be omitted from here on.

Note that the continuity equation (3.5) does not provide any relation between the azimuthal velocity and the vertical velocity. Consequently, the scaling of the ratio of the azimuthal velocity to the vertical velocity must be determined by the flow dynamics.

In this context, the term

$$\frac{\delta^2 \mathrm{Re}}{r} \frac{\partial v_\theta^2}{\partial z} = \frac{2\delta^2 \mathrm{Re}}{r} v_\theta \frac{\partial v_\theta}{\partial z} \tag{3.7}$$

in (3.4) is of special interest since it couples the azimuthal velocity v_θ to both the radial velocity v_r and the vertical velocity v_z, implying that a vertical gradient in v_θ will drive a secondary flow in the (r, z)-plane.

To study the limit of shallow flows ($\delta \ll 1$), we propose an asymptotic expansion of the variables in powers of δ:

$$\omega_\theta = \sum_{n=0}^{\infty} \delta^n \omega_{\theta,n}, \quad v_\theta = \sum_{n=0}^{\infty} \delta^n v_{\theta,n}, \quad v_r = \sum_{n=0}^{\infty} \delta^n v_{r,n}, \quad v_z = \sum_{n=0}^{\infty} \delta^n v_{z,n}. \tag{3.8}$$

In the current chapter, we consider for simplicity that $\mathrm{Re} = \mathcal{O}(1)$ for $\delta \downarrow 0$, while a more general perturbation analysis is given in Chapter 4.

By substituting (3.8) into (3.5), we immediately obtain that $v_{z,0} = 0$. Substitution of (3.8) into (3.4) yields

$$\frac{\partial \omega_{\theta,0}}{\partial t} - \frac{\partial^2 \omega_{\theta,0}}{\partial z^2} = 0 \tag{3.9}$$

at zeroth order, $\omega_{\theta,1} = 0$ at first order, and

$$\frac{\partial \omega_{\theta,2}}{\partial t} + \mathrm{Re}\left(v_{r,0} \frac{\partial \omega_{\theta,0}}{\partial r} + \frac{v_{r,0}\omega_{\theta,0}}{r} + v_{z,1} \frac{\partial \omega_{\theta,0}}{\partial z} \right) - \mathrm{Re}\frac{1}{r}\frac{\partial v_{\theta,0}^2}{\partial z}$$
$$= \frac{\partial^2 \omega_{\theta,0}}{\partial r^2} + \frac{\partial}{\partial r} r^{-1} \omega_{\theta,0} + \frac{\partial^2 \omega_{\theta,2}}{\partial z^2} \tag{3.10}$$

at second order.

Note, from (3.9), that $\omega_{\theta,0}$ is not affected by the primary motion and only depends on the initial condition for ω_θ. In fact, if $v_r = v_z = 0$ at $t = 0$, then $\omega_{\theta,0} = \omega_{\theta,1} = 0$ and $v_{r,0} = v_{r,1} = v_{z,1} = v_{z,2} = 0$. Substituting these results into (3.10) yields

$$\frac{\partial \omega_{\theta,2}}{\partial t} - \frac{\partial^2 \omega_{\theta,2}}{\partial z^2} = \mathrm{Re}\frac{1}{r}\frac{\partial v_{\theta,0}^2}{\partial z}. \tag{3.11}$$

It can be seen from this equation that a vertical gradient in v_θ will drive a secondary flow that at lowest order ($\delta \downarrow 0$) scales as follows

$$\omega_\theta = \delta^2 \omega_{\theta,2}, \quad v_r = \delta^2 v_{r,2}, \quad v_z = \delta^3 v_{z,3}, \tag{3.12}$$

provided that $\omega_\theta = 0$ at $t = 0$. Therefore, it is convenient to define the new variables

$$\tilde{\omega}_\theta = \frac{\omega_\theta}{\delta^2 \mathrm{Re}}, \quad \tilde{v}_r = \frac{v_r}{\delta^2 \mathrm{Re}}, \quad \tilde{v}_z = \frac{v_z}{\delta^3 \mathrm{Re}}, \quad \tilde{v}_\theta = v_\theta, \tag{3.13}$$

through which (3.3)–(3.4) simplify to

$$\frac{\partial \tilde{v}_\theta}{\partial t} - \frac{\partial^2 \tilde{v}_\theta}{\partial z^2} = 0, \tag{3.14}$$

$$\frac{\partial \tilde{\omega}_\theta}{\partial t} - \frac{\partial^2 \tilde{\omega}_\theta}{\partial z^2} = \frac{1}{r} \frac{\partial \tilde{v}_\theta^2}{\partial z}, \tag{3.15}$$

where $\tilde{\omega}$, $\tilde{v}_r$, $\tilde{v}_z$, $\tilde{v}_\theta$ are all of $\mathcal{O}(1)$ for $\delta \downarrow 0$. This implies that the velocity components scale to lowest order as

$$\frac{v_r}{v_\theta} = \mathcal{O}(\delta^2 \mathrm{Re}), \tag{3.16}$$

and

$$\frac{v_z}{v_\theta} = \mathcal{O}(\delta^3 \mathrm{Re}). \tag{3.17}$$

If we consider the azimuthal velocity as the typical horizontal velocity — a common choice — the latter result contradicts the usual assumption that the ratio of vertical to horizontal velocity should scale with δ. Not only does the vertical velocity scale with δ^3, but it also depends linearly on the Reynolds number of the primary motion. The range of validity for the scaling proposed in (3.16) and (3.17) will be studied using numerical simulations in Section 3.5.

3.4 Analytical solution for a shallow swirl-flow

Equation (3.14) is a diffusion equation, where both radial diffusion and advection by the secondary motion have been neglected as compared to (3.3). Since at lowest order the evolution of the main flow is independent of the secondary flow, flows governed by (3.14) and (3.15) can be considered as Q2D.

To analyze the two-dimensionality and the evolution of shallow swirl-flows, (3.14) and (3.15) are solved analytically. For this, we consider as initial condition a swirl flow with a Poiseuille-like vertical structure and a radial dependence which is, at this stage, arbitrary:

$$\tilde{v}_\theta(r, z, 0) = R(r) \sin(\pi z / 2), \tag{3.18}$$

where $R(r)$ is such that $\mathrm{d}R(r)/\mathrm{d}r$ is of the same order of magnitude as $R(r)$. This is achieved by choosing the appropriate radial length scale L_0. Furthermore, for the secondary motion we consider

$$\tilde{\omega}_\theta(r, z, 0) = 0. \tag{3.19}$$

The Poiseuille-like vertical profile was used as initial condition since the vertical structure of shallow axisymmetric vortices dominated by bottom friction tends quickly to such a profile (Satijn et al., 2001).

The solution of (3.14) that satisfies the no-slip boundary condition at the bottom ($\tilde{v}_\theta = 0$ at $z = 0$), the stress-free boundary condition at the top ($\partial\tilde{v}_\theta/\partial z = 0$, at $z = 1$), and the initial condition (3.18) is given by

$$\tilde{v}_\theta(r,z,t) = R(r)\sin\left(\frac{\pi}{2}z\right)\exp\left(-\frac{\pi^2}{4}t\right).\tag{3.20}$$

We note that the azimuthal velocity $\tilde{v}_\theta$ decays exponentially at a rate $\lambda_R = \pi^2/4$ [equivalent to $\pi^2\nu/(4H^2)$ in dimensional form], which is in some studies referred to as the external friction parameter. For shallow flows, it is also known as the Rayleigh friction parameter, and it is commonly used to parametrize the vertical dependence of shallow flows in 2D equations with a linear friction term (Dolzhanskii et al., 1992; Satijn et al., 2001).

By substituting (3.20) into (3.15), we obtain an equation for the secondary flow that is driven by the primary swirl:

$$\frac{\partial\tilde{\omega}_\theta}{\partial t} - \frac{\partial^2\tilde{\omega}_\theta}{\partial z^2} = \frac{\pi}{2}\frac{R^2(r)}{r}\sin(\pi z)\exp\left(-\frac{\pi^2}{2}t\right).\tag{3.21}$$

To solve (3.21) with the appropriate boundary conditions, it is useful to introduce the streamfunction $\tilde{\psi}$ facilitated by (3.5) and defined by

$$\tilde{v}_r = -\frac{1}{r}\frac{\partial\tilde{\psi}}{\partial z},\tag{3.22}$$

$$\tilde{v}_z = \frac{1}{r}\frac{\partial\tilde{\psi}}{\partial r}.\tag{3.23}$$

From this and (3.6), $\tilde{\omega}_\theta$ is given by

$$\tilde{\omega}_\theta = -\frac{1}{r}\frac{\partial^2\tilde{\psi}}{\partial z^2} - \delta^2\frac{\partial}{\partial r}\left(\frac{1}{r}\frac{\partial\tilde{\psi}}{\partial r}\right),\tag{3.24}$$

which at lowest order ($\delta\downarrow 0$) reduces to

$$\tilde{\omega}_\theta = -\frac{1}{r}\frac{\partial^2\tilde{\psi}}{\partial z^2}.\tag{3.25}$$

The evolution of the secondary flow is now governed by the following equation:

$$\frac{\partial^4\Psi}{\partial z^4} - \frac{\partial}{\partial t}\frac{\partial^2\Psi}{\partial z^2} = \sin(\pi z)\exp\left(-\frac{\pi^2}{2}t\right),\tag{3.26}$$
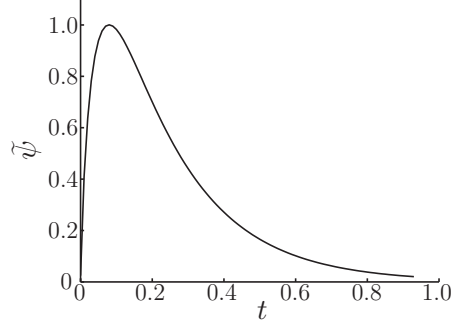
Figure 3.2 – *Normalized streamfunction as a function of time.*

where

$$\Psi(z,t) = \frac{2}{\pi} \frac{\tilde{\psi}(r,z,t)}{R^2(r)}, \tag{3.27}$$

with the boundary conditions

$$\Psi(0,t) = 0, \quad \Psi(1,t) = 0, \quad \left.\frac{\partial \Psi(z,t)}{\partial z}\right|_{z=0} = 0, \quad \left.\frac{\partial^2 \Psi(z,t)}{\partial z^2}\right|_{z=1} = 0, \tag{3.28}$$

and the initial condition

$$\Psi(z,0) = 0. \tag{3.29}$$

The detailed procedure to solve the initial-value problem (3.26)–(3.29) is given in Appendix A, and the solution is

$$
\begin{aligned}
\Psi(z,t) = {} & \frac{2\sin(\pi z)}{\pi^4} \mathrm{e}^{-\pi^2 t/2} + \frac{2}{\pi^3 \left[\tan\left(\frac{\pi}{\sqrt{2}}\right) - \frac{\pi}{\sqrt{2}}\right]} \\
& \times \left\{ \tan\left(\frac{\pi}{\sqrt{2}}\right)\left[1 - z - \cos\left(\frac{\pi}{\sqrt{2}}z\right)\right] + \sin\left(\frac{\pi}{\sqrt{2}}z\right) \right\} \mathrm{e}^{-\pi^2 t/2} \\
& - \sum_{n=0}^{\infty} \frac{4\gamma_n}{\pi \tan^2(\gamma_n)(\pi^2 - \gamma_n^2)(\pi^2 - 2\gamma_n^2)} \\
& \times \left\{ \tan(\gamma_n)[1 - z - \cos(\gamma_n z)] + \sin(\gamma_n z) \right\} \mathrm{e}^{-\gamma_n^2 t},
\end{aligned}
\tag{3.30}
$$

where γ_n are solutions of the transcendental equation $\tan(\gamma_n) = \gamma_n$.

Figure 3.2 shows the temporal evolution of the normalized stream function at an arbitrary location in the (r,z)-plane and which is characteristic for the overall behavior of $\tilde{\psi}$. Initially, the normalized streamfunction shows a rapid increase as the secondary motion is set up by the primary flow. During this transient period, the infinite series in (3.30) forms the dominant contribution to $\tilde{\psi}$. For longer times,

the behavior of the secondary motion is dominated by the first and second terms on the right-hand side of (3.30) since $\pi^2/2 \ll \gamma_n^2$. Note that the second term is present in the solution because the first term alone does not satisfy the boundary condition at the no-slip bottom.

From the streamfunction $\tilde{\psi}$, we can calculate both the radial and vertical velocity components:

$$v_r = -\frac{\delta^2 \mathrm{Re}}{r}\frac{\partial \tilde{\psi}}{\partial z} = -\frac{\pi \delta^2 \mathrm{Re}}{2}\frac{R^2(r)}{r}\frac{\partial \Psi(z,t)}{\partial z}, \tag{3.31}$$

$$v_z = \frac{\delta^3 \mathrm{Re}}{r}\frac{\partial \tilde{\psi}}{\partial r} = \frac{\pi \delta^3 \mathrm{Re}}{2r}\frac{\partial R^2(r)}{\partial r}\Psi(z,t), \tag{3.32}$$

which will be compared in the next section to results from numerical simulations.

3.5   Numerical study

Numerical simulations were performed to determine the range of validity of the analytical results presented in the preceding sections. A finite-element code, COMSOL, was used to solve the full Navier–Stokes equations (For more details see COMSOL AB, 2008). The flow was assumed to be incompressible and azimuthally symmetric ($\partial/\partial\theta = 0$).

The initial azimuthal flow was taken to be

$$v_\theta(r,z,0) = R(r)\sin\left(\frac{\pi}{2}z\right), \tag{3.33}$$

where the radial dependence was specified as

$$R(r) = \frac{1}{2r}\left[1 - \exp\left(-r^2\right)\right]. \tag{3.34}$$

Such vortex is known as a Lamb–Oseen vortex, and it was chosen because of its similarity to some vortices created in the laboratory (see e.g. Hopfinger & van Heijst, 1993). However, as shown in Section 3.3, the scaling of v_r and v_z is independent of the radial profile for $\delta \downarrow 0$.

The computational domain extends in the (r,z)-plane for $0 \leq r \leq 12$ and $0 \leq z \leq 1$. The radial length of the container is approximately ten times the radius of maximum velocity of the Lamb–Oseen vortex and large enough to neglect the effects of this boundary on the secondary motion.

As boundary conditions, we considered relevant symmetry conditions for $r = 0$, and we applied a stress-free condition at $r = 12$ to further reduce the influence of this lateral boundary. In the vertical, a stress-free condition was applied at $z = 1$, and a no-slip boundary condition at the bottom ($z = 0$). At the top boundary, a *rigid-lid* approximation is implemented, so excluding free-surface deformations.

We performed simulations at Reynolds number Re = 100, 1000 and 2500 where the typical velocity U is defined as $U \equiv L_0\hat{\omega}_0$, with $\hat{\omega}_0$ the maximum of the vertical
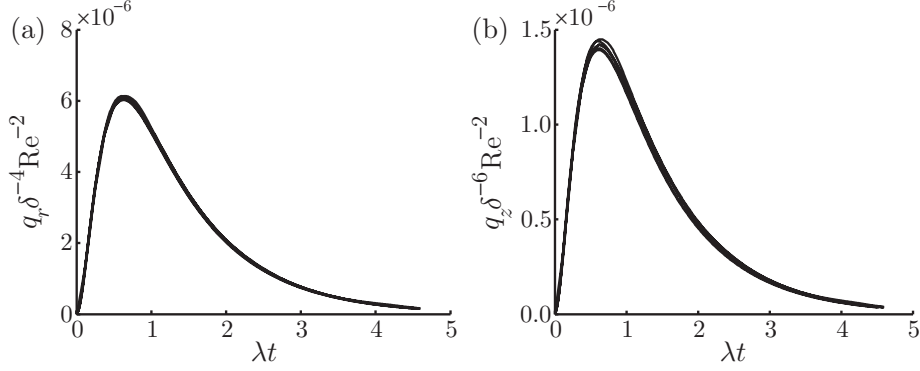
Figure 3.3 – *(a) Kinetic energy ratio $q_r/\delta^4\mathrm{Re}^2$ as a function of time for $\mathrm{Re} = 1000,\ 2500$ and $\delta^2\mathrm{Re} = 1, 2, 5$. (b) Kinetic energy ratio $q_z/\delta^6\mathrm{Re}^2$ as a function of time for $\mathrm{Re} = 1000,\ 2500$ and $\delta^2\mathrm{Re} = 1, 2, 5$. Time is normalized with $1/\lambda$.*

vorticity component at $t = 0$. In addition, for each Re-value the aspect ratio δ was varied within the range $1 \leq \delta^2\mathrm{Re} \leq 160$.

To study the scaling of the velocity components, we define the kinetic energy for each velocity component v_i (where $i = r, \theta, z$) as

$$E_i = \pi \int_0^1 \int_0^{12} v_i^2 r \mathrm{d}r \mathrm{d}z, \tag{3.35}$$

and the kinetic energy ratio associated with each velocity component v_i as

$$q_i = \frac{E_i}{E_\theta}. \tag{3.36}$$

In addition, a typical decay rate λ for each numerical solution is obtained by fitting the exponential function $\exp(-2\lambda t)$ to E_θ.

Figure 3.3 shows (a) the value of $q_r/(\delta^4\mathrm{Re}^2)$ and (b) the value of $q_z/(\delta^6\mathrm{Re}^2)$ as a function of time for $\mathrm{Re} = 1000,\ 2500$ and $\delta^2\mathrm{Re} = 1, 2, 5$. Clearly, the six curves collapse to one curve in each graph. This means that the evolution of q_r is self-similar when scaling q_r with $(\delta^2\mathrm{Re})^2$ for $\delta^2\mathrm{Re} = 1,\ 2,\ 5$, and that the evolution of q_z is self-similar when scaling q_z with $(\delta^3\mathrm{Re})^2$ for the same values $\delta^2\mathrm{Re} = 1,\ 2,\ 5$. This is consistent with the analytical solution obtained in the previous section [see (3.31) and (3.32)] for $\delta \downarrow 0$.

To quantify the range of validity of the observed self-similarity, we now focus on characteristic values of the quantities q_r and q_z, namely $\max(q_r)$ and $\max(q_z)$.

Figure 3.4 (a) shows the maximum value of the kinetic energy associated with the radial velocity, i.e. $\max(q_r)$, for simulations with $\mathrm{Re} = 100,\ 1000$ and 2500 as a function of $\delta\,\mathrm{Re}^{1/2}$ together with the results obtained from the analytical expressions (3.20), (3.31), and (3.32). As can be seen, for $\delta\,\mathrm{Re}^{1/2} \lesssim 3$, the numerical results coincide well with the analytical solution; hence, $\max(q_r)$ scales like $\delta^4\mathrm{Re}^2$.

(a)

(b)
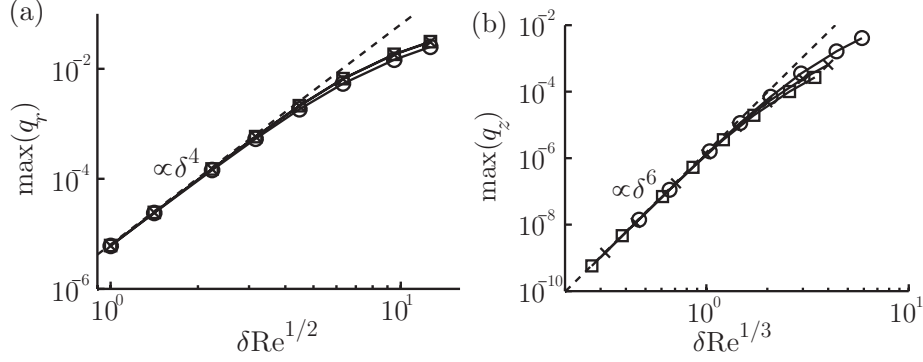
Figure 3.4 – *Values of (a)* $\max(q_r)$ *as a function of* $\delta \mathrm{Re}^{1/2}$ *and (b)* $\max(q_z)$ *as a function of* $\delta \mathrm{Re}^{1/3}$ *for* $\mathrm{Re} = 100$ *(○),* $\mathrm{Re} = 1000$ *(×), and* $\mathrm{Re} = 2500$ *(□). The dashed line represents the analytical solution given by* (3.31) *and* (3.32)*, and* (3.20)*.*

For larger values of $\delta \, \mathrm{Re}^{1/2}$, there is a change in the slope of the curve given by the numerical results. For high Re-values (e.g. Re = 1000, 2500), this change in the slope is due to the increasing importance of advection. However, for these large Re-values the results tend to the same curve, suggesting that the radial velocity only depends on $\delta^2 \mathrm{Re}$. On the other hand, for low Re-values (e.g. Re = 100), the numerical results show a larger change in the slope. This can be explained since the aspect ratio is not small, and hence, horizontal diffusion can not be neglected, and the approximation (3.25) does not hold.

The results obtained so far are reminiscent of the flow in curved pipes studied initially by Dean (1927). Such a flow is governed by two characteristic parameters: a geometrical parameter $\delta_D = a/R_D$, where a is the radius of the pipe, and R_D is the radius of curvature of the pipe; and a dynamical quantity, the Reynolds number Re_D. Following this analogy, a straight pipe would be equivalent to an axisymmetric flow in a plane where, in both cases, no secondary motion exists. Furthermore, a loosely coiled pipe ($\delta_D \ll 1$) corresponds to a shallow flow $\delta \ll 1$. Dean expanded the Navier–Stokes equation in powers of δ_D and found that for $\delta_D \ll 1$ only one parameter $\kappa = \delta_D^{1/2}\mathrm{Re}_D$ — known now as the Dean number — governs the flow. This gives rise to the so-called Dean number similarity. As found in the present paper, the governing parameter for shallow axisymmetric flows is $\delta^2 \mathrm{Re}$.

The graph in figure 3.4 (b) shows the maximum of the kinetic energy associated with the vertical velocity, i.e. $\max(q_z)$, for simulations with Re = 100, 1000 and 2500 as a function of $\delta \, \mathrm{Re}^{1/3}$ together with the analytical results given by (3.20), (3.31), and (3.32). As can be seen, for small values of $\delta \, \mathrm{Re}^{1/3}$, the values of $\max(q_z)$ agree with the analytical results, indicating that the vertical velocity scales with $\delta^3 \mathrm{Re}$. This contradicts the usual assumption that the vertical velocity scales with δ. However, this scaling breaks down for $\delta \, \mathrm{Re}^{1/3} \gtrsim 1$ due to the effects of the advection associated with the secondary motion in the (r, z)-plane.
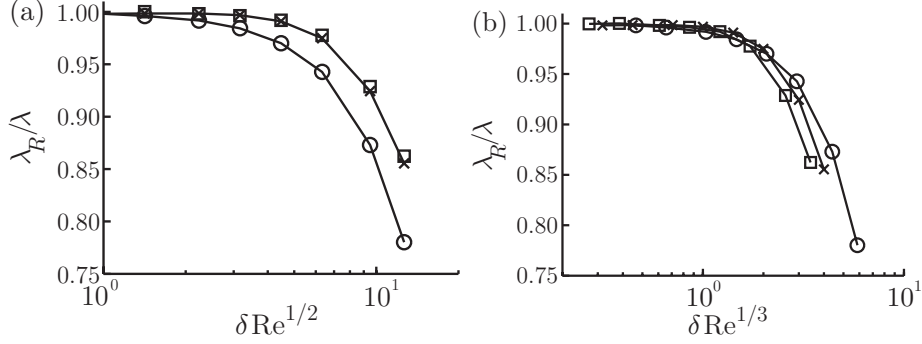
Figure 3.5 – *(a) The typical decay time λ_R/λ as a function of $\delta\,\mathrm{Re}^{1/2}$ and (b) λ_R/λ as a function of $\delta\,\mathrm{Re}^{1/3}$ for simulations with $\mathrm{Re} = 100\ (\circ)$, $\mathrm{Re} = 1000\ (\times)$, and $\mathrm{Re} = 2500\ (\square)$.*

Finally, we show how the change of regimes in the scaling of v_r and v_z relates to the primary motion, and hence, to the two-dimensionality of the flow. Figure 3.5 presents the decay time λ^{-1} of the primary flow normalized by the inverse of the Rayleigh parameter $\lambda_R^{-1} = 4/\pi^2$ as a function of (a) $\delta\,\mathrm{Re}^{1/2}$ and (b) $\delta\,\mathrm{Re}^{1/3}$. For $\mathrm{Re} = 1000$, 2500 and $\delta\,\mathrm{Re}^{1/2} \leq 3$, it is observed that $\lambda_R/\lambda \approx 1$, suggesting that (3.20) is valid in this regime. However, λ_R/λ starts to deviate strongly from unity for $\delta\,\mathrm{Re}^{1/2} \approx 3$, which corresponds with the value of $\delta\,\mathrm{Re}^{1/2}$ where the scaling of $\max(q_r)$ starts to deviate from the analytically obtained results for the secondary motion. For $\mathrm{Re} = 100$, λ_R/λ deviates from unity for smaller values of $\delta\,\mathrm{Re}^{1/2}$ than for $\mathrm{Re} = 1000$, 2500. This is due to the damping related to the horizontal momentum diffusion, which becomes important for large δ-values.

The deviation of λ from λ_R is related to qualitative changes in the azimuthal flow. For small values of $\delta^2\mathrm{Re}$, the flow has a Poiseuille-like vertical structure. However, for large values of $\delta^2\mathrm{Re}$, the flow consists of a thin boundary layer at the bottom and an inviscid interior. This is very similar in flows in curved pipes, where for small Dean number the main flow through the pipe is of Poiseuille type, while for large Dean number the flow is composed of a thin boundary layer and an inviscid core (Berger et al., 1983).

As shown in figure 3.5 (b), for $\delta\,\mathrm{Re}^{1/3} \lesssim 1$, $\lambda_R/\lambda \approx 1$ for all Re-values. However, for $\delta\,\mathrm{Re}^{1/3} \gtrsim 1$, it is observed that λ_R/λ deviates strongly from unity. Note that $\delta\,\mathrm{Re}^{1/3} \approx 1$ is also the value of $\delta\,\mathrm{Re}^{1/3}$ for which $\max(q_z)$ starts to strongly deviate from the analytical results. This suggests that for $\delta\,\mathrm{Re}^{1/3} \gtrsim 1$ the secondary motion strongly affects the primary azimuthal flow, and hence, that the secondary motion can not be neglected.

3.6   Discussion and conclusions

Using a formal perturbation approach in the aspect ratio δ, we obtained at lowest order ($\delta \downarrow 0$) a set of simplified Navier–Stokes equations for the evolution of a shallow axisymmetric swirl flow. Flows governed by these simplified equations can be considered as Q2D since the secondary motion can be neglected in the evolution of the primary azimuthal motion.

It was shown that for shallow axisymmetric swirl flows dominated by bottom friction the magnitude of the radial velocity scales with $\delta^2 \mathrm{Re}$, while the magnitude of the vertical velocity scales with $\delta^3 \mathrm{Re}$ with respect to the primary motion. Consequently, we conclude that the dynamics of the flow plays a crucial role in the scaling of the vertical velocity, and that the argument based only on the continuity equation is inadequate to explain this scaling. However, this argument seems to become valid for large values of $\delta^2 \mathrm{Re}$ and small values of δ, i.e. when the shear flow is fully turbulent as considered by Jirka & Uijttewaal (2004). This can be seen in figure 3.4, since the value of $\max(q_r)$ tends towards being independent of δ for such large values of $\delta^2 \mathrm{Re}$. Nevertheless, we wish not to expand this work towards a fully-turbulent case since such regime should be treated differently.

Numerical simulations served to test the analytical results and to determine their range of validity. We compared the results from fully three-dimensional numerical simulations of a decaying Lamb–Oseen vortex to the analytical solution of the simplified Navier–Stokes equations obtained for shallow swirl-flows where advection due to the secondary flow has been neglected. Good agreement between the numerical and analytical solutions was found for $\delta \, \mathrm{Re}^{1/2} \lesssim 3$ and $\delta \, \mathrm{Re}^{1/3} \lesssim 1$. Consequently, for these values of $\delta \, \mathrm{Re}^{1/2}$ and $\delta \, \mathrm{Re}^{1/3}$ this flow can be considered as Q2D.

To quantify the degree of two-dimensionality of shallow flows is a complicated matter. One quantity commonly used is the ratio of kinetic energy of the vertical velocity component to the kinetic energy of the horizontal velocity components. For example, Satijn et al. (2001) considered this ratio together with two other characteristic quantities and argued that the flow can be considered as Q2D if these quantities are smaller than a certain threshold, which is rather arbitrary. Another way to quantify the degree of two dimensionality of shallow flows is to estimate the dynamical forces related to the vertical or secondary motions. In this case, it is not a priori obvious whether these dynamical forces should be evaluated at a certain location in the fluid or need to be averaged over a certain domain (see e.g. Akkermans et al., 2008b). Hence, this approach also implies some degree of arbitrariness, depending on the position where these forces are evaluated.

The regime where the primary flow can be considered as Q2D is rarely studied in shallow layer experiments. For example, experiments of a shallow electromagnetically driven dipolar vortex were performed for $4 \lesssim \delta \, \mathrm{Re}^{1/3} \lesssim 7.7$ and $\mathrm{Re} \sim 4800$ (Akkermans et al., 2008b). Clercx et al. (2003) performed experiments of Q2D turbulence in a shallow layer with a lower bound for $\delta \, \mathrm{Re}^{1/3} \approx 2.17$ with $\mathrm{Re} \approx 2500$. These experiments fall outside the range where $v_z/v_\theta = \mathcal{O}(\delta^3 \mathrm{Re})$. Therefore, we

propose experiments to be performed in the parameter regime studied in this chapter to confirm the scaling presented here.

Chapter 4

Decaying axisymmetric swirl flows with background rotation

4.1 Introduction

In the past 30 years, there has been a large interest in creating quasi-two-dimensional flows in the laboratory aimed to verify, for example, theories about the stability of two-dimensional (2D) shear flows and 2D spatially periodic flows (Dolzhanskii et al., 1990) and the properties of two-dimensional turbulence (Paret & Tabeling, 1997). Inspired by the large-scale flows in the oceans and the atmosphere that seem to behave in a 2D way, experimentalists have used background rotation (e.g. Afanasyev & Wells, 2005) and the thin-layer configuration (e.g. Tabeling et al., 1991) to enforce the two-dimensionality of flows in the laboratory. However, it is well known that both of these methods have drawbacks and limits (see Chapter 2).

Drawing again inspiration from atmospheric and oceanic flows, it might be tempting to apply background rotation to a shallow flow (or to reduce the depth of a fluid subjected to background rotation) in order to further enforce its two-dimensionality. It is the goal of the present chapter to determine if this combination of background rotation and shallowness can indeed be a useful tool to achieve quasi-two-dimensional (Q2D) flows in the laboratory. If so, it is of interest to also find its limitations. For this, it is first necessary to establish criteria to determine which flows can be considered as Q2D.

To achieve these goals, the dynamics of a shallow axisymmetric monopolar vortex subjected to background rotation is studied. A systematic analysis of the two-dimensionality of the flow is conducted using numerical simulations and a perturbation analysis. Through the perturbation analysis, at lowest order nine
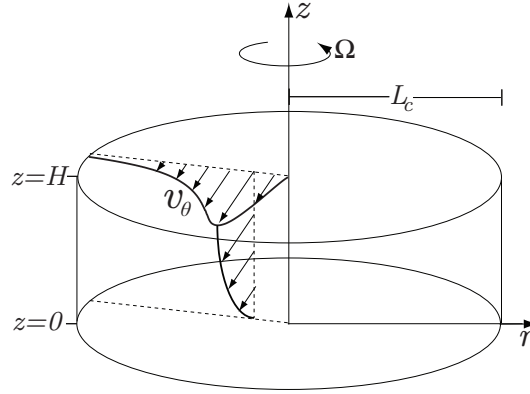
Figure 4.1 – *Sketch of the problem's geometry.*

different flow regimes with different governing equations were found. In only five of these regimes the flow can be considered as Q2D. The results from numerical simulations are compared with the flow characteristics in each of the nine regimes to determine their boundaries in the parameter space.

The chapter is organized as follows: Section 4.2 presents the governing equations and the geometry pertinent to the problem. In Section 4.3, we present the numerical and analytical methods to study the flow. Section 4.4 is devoted to the results of two limiting cases: the limit of weak background rotation and the limit of strong background rotation. In Section 4.5, the rotation rate dependence of the characteristics of the flow is discussed. Finally, in Section 4.6, a brief summary of the main results is outlined, and some conclusions are given in Section 4.7.

4.2   Statement of the problem

We consider a freely evolving swirl flow governed by the Navier–Stokes equation in a rotating reference frame

$$\frac{\partial \boldsymbol{v}}{\partial t} + \boldsymbol{v} \cdot \boldsymbol{\nabla} \boldsymbol{v} + 2\boldsymbol{\Omega} \times \boldsymbol{v} = -\frac{1}{\rho}\boldsymbol{\nabla}P + \nu\nabla^2\boldsymbol{v} \tag{4.1}$$

and the continuity equation for an incompressible fluid

$$\boldsymbol{\nabla} \cdot \boldsymbol{v} = 0, \tag{4.2}$$

where $\boldsymbol{v}$ is the fluid velocity; $\boldsymbol{\Omega}$ is the rotation vector of the system; ν is the kinematic viscosity of the fluid; P is the reduced pressure; and ρ is the density of the fluid.

The fluid is contained inside a cylinder, with depth H and radius L_c, rotating at a rate Ω around its axis, as shown in figure 4.1. For simplicity, we consider that

$\Omega > 0$. The cylinder has a no-slip bottom, and the fluid upper surface is stress-free, flat, and rigid.

Due to the geometry of the problem, it is convenient to use cylindrical coordinates (r, θ, z) where the vertical axis is parallel to the rotation axis ($\boldsymbol{\Omega} = \Omega \hat{\boldsymbol{z}}$); the velocity is then written as $\boldsymbol{v} = (v_r, v_\theta, v_z)$, and the vorticity as $\boldsymbol{\omega} = \boldsymbol{\nabla} \times \boldsymbol{v} = (\omega_r, \omega_\theta, \omega_z)$.

As initial condition, we consider a Lamb–Oseen vortex with radius L_0 and which is uniform in the vertical:

$$v_\theta(r, z, 0) = \frac{U\,L_0}{2r}\left\{1 - \exp[-(r/L_0)^2]\right\},\tag{4.3}$$

and no secondary flow in the (r, z)-plane

$$v_z(r, z, 0) = v_r(r, z, 0) = 0,\tag{4.4}$$

where U is a typical velocity of the flow. The Lamb–Oseen vortex was chosen because it is known to be similar to some vortices created in the laboratory (Hopfinger & van Heijst, 1993), and because of its stability properties. To minimize the influence of the side wall of the cylinder on the evolution of the vortex, we take $L_0 \ll L_c$.

To derive the relevant nondimensional parameters, we introduce the following nondimensional variables denoted by primes:

$$t' = \frac{\nu\,t}{H^2}, \quad r' = \frac{r}{L_0}, \quad z' = \frac{z}{H}, \quad \boldsymbol{v}' = \frac{\boldsymbol{v}}{|U|}, \quad \omega'_\theta = \frac{H}{|U|}\omega_\theta.\tag{4.5}$$

We consider the flow to have azimuthal symmetry ($\partial/\partial\theta = 0$), so that (4.1) and (4.2) can be rewritten as

$$\frac{\partial v'_\theta}{\partial t'} + \delta^2 \mathrm{Re}\left(v'_r \frac{\partial v'_\theta}{\partial r'} + \frac{v'_\theta v'_r}{r'}\right) + \delta\,\mathrm{Re} v'_z \frac{\partial v'_\theta}{\partial z'}$$
$$= -\frac{\delta^2 \mathrm{Re}}{\mathrm{Ro}}v_r + \delta^2\left[\frac{\partial^2 v'_\theta}{\partial r'^2} + \frac{\partial}{\partial r}\left(\frac{v'_\theta}{r'}\right)\right] + \frac{\partial^2 v'_\theta}{\partial z'^2},\tag{4.6}$$

$$\frac{\partial \omega'_\theta}{\partial t'} + \delta^2 \mathrm{Re}\left(v'_r \frac{\partial \omega'_\theta}{\partial r'} - \frac{\omega'_\theta v'_r}{r'}\right) + \delta\,\mathrm{Re} v'_z \frac{\partial \omega'_\theta}{\partial z'}$$
$$= \delta^2 \mathrm{Re}\left(\frac{1}{r'}\frac{\partial v'^2_\theta}{\partial z'} + \frac{1}{\mathrm{Ro}}\frac{\partial v'_\theta}{\partial z}\right) + \delta^2\left[\frac{\partial^2 \omega'_\theta}{\partial r'^2} + \frac{\partial}{\partial r'}\left(\frac{\omega'_\theta}{r}\right)\right] + \frac{\partial^2 \omega'_\theta}{\partial z'^2},\tag{4.7}$$

$$\delta\frac{1}{r'}\frac{\partial}{\partial r'}(r' v'_r) + \frac{\partial v'_z}{\partial z'} = 0,\tag{4.8}$$

$$\omega'_\theta = \frac{\partial v'_r}{\partial z'} - \delta\frac{\partial v'_z}{\partial r'}\tag{4.9}$$

with $\mathrm{Re} \equiv |U|L_0/\nu$ the Reynolds number, $\delta \equiv H/L_0$ the aspect ratio, and $\mathrm{Ro} \equiv |U|/(2\Omega L_0)$ the Rossby number. Note that the Ekman number Ek, which is also

commonly used to characterize rotating flows, is related to Ro and Re by $\mathrm{Ek} \equiv 2\mathrm{Ro}/(\delta^2\mathrm{Re}) = \nu/(\Omega H^2)$. In the following, we consider the typical scale $U = \hat{\omega}_0 L_0$ with $\hat{\omega}_0$ the maximum of the vertical vorticity component at time $t = 0$. To simplify the notation, the primes will be omitted from here on.

The primary motion of the monopolar vortex is then governed by (4.6), while (4.7) governs the secondary motion in the (r, z)-plane. Of special interest is the term

$$\delta^2\mathrm{Re}\left(\frac{1}{r}\frac{\partial v_\theta^2}{\partial z} + \frac{1}{\mathrm{Ro}}\frac{\partial v_\theta}{\partial z}\right) = \delta^2\mathrm{Re}\frac{1}{r}\frac{\partial v_\theta^2}{\partial z} + \frac{2}{\mathrm{Ek}}\frac{\partial v_\theta}{\partial z} \tag{4.10}$$

in (4.7), which couples the secondary motion to the primary motion and plays a central role in the flow dynamics studied in the current chapter. It can be seen from this term that a vertical gradient in v_θ drives the secondary motion. The physical mechanism by which the swirl generates azimuthal vorticity is clearly explained by Davidson (1989).

4.3   Quantification of the two-dimensionality of the flow

4.3.1   Quantifying the strength of the secondary motion

As previously mentioned, a vertical gradient of the azimuthal velocity drives a secondary motion in the (r, z)-plane. In turn, this secondary motion could redistribute the azimuthal velocity v_θ and thus modify the primary swirl through vortex stretching. For this reason, it is of interest to measure the strength of the secondary motion.

We define two quantities to measure the strength of the secondary flow in the vortex core: the normalized kinetic energy Q_r associated with the radial velocity component and the normalized kinetic energy Q_z associated with the vertical velocity component, i.e.

$$Q_r(t) = \frac{\int_0^1 \int_0^1 v_r^2(r, z, t)r\mathrm{d}r\mathrm{d}z}{\int_0^1 \int_0^1 v_\theta^2(r, z, t)r\mathrm{d}r\mathrm{d}z}, \qquad Q_z(t) = \frac{\int_0^1 \int_0^1 v_z^2(r, z, t)r\mathrm{d}r\mathrm{d}z}{\int_0^1 \int_0^1 v_\theta^2(r, z, t)r\mathrm{d}r\mathrm{d}z}. \tag{4.11}$$

Since it is difficult to measure Q_r and Q_z in experiments, we also introduce two quantities that provide information about the strength of the secondary motion as measured at the free-surface (as is commonly done in laboratory experiments). These quantities are the normalized kinetic energy q_r associated with the radial

velocity component at the surface

$$q_r(t) = \frac{\displaystyle\int_0^1 v_r^2(r,1,t)r\mathrm{d}r}{\displaystyle\int_0^1 v_\theta^2(r,1,0)r\mathrm{d}r} \tag{4.12}$$

and the normalized horizontal divergence at the surface

$$\Delta(t) = \frac{\displaystyle\int_0^1 \frac{\partial}{\partial r}[rv_r(r,1,t)]\mathrm{d}r}{\displaystyle\int_0^1 \omega_z(r,1,0)r\mathrm{d}r}. \tag{4.13}$$

Note that the integration in the r-direction of all four quantities is limited to the vortex core ($r \leq 1$), where most of the energy of the secondary motion is expected to be concentrated.

4.3.2 Perturbation analysis

Usually, the absolute values of (4.11)–(4.13) or similar quantities are used to determine if a flow can be considered as Q2D (see e.g. Satijn et al., 2001). The flow is then considered as Q2D if these absolute values are smaller than a certain threshold. Besides the arbitrariness of setting the threshold, this method has the drawback that the absolute values depend on the integration domain considered or on the limited availability of experimental data in space (Akkermans et al., 2008a,b).

For these reasons, in the current chapter we propose an alternative procedure to determine if a flow can be considered as Q2D, following the approach used in the previous chapter. First, a perturbation analysis for small δ-values is used to derive simplified versions of the governing equations, which depend on the values of the parameters of the problem. These simplified governing equations are analyzed to determine if a flow governed by them can be considered as Q2D. On the other hand, the full governing equations (4.6)–(4.8) are solved numerically for different values of the problem parameters, and the quantities (4.11)–(4.13) are used to characterize the flow obtained through these numerical simulations. Finally, to determine if this flow is Q2D, its characteristics are compared with the characteristics of the solutions to the simplified equations that were obtained through the perturbation analysis.

In the limit of shallow flows ($\delta \ll 1$), we propose an asymptotic expansion of the variables in terms of δ:

$$\omega_\theta = \sum_{n=0}^\infty \delta^n \omega_{\theta,n}, \quad v_\theta = \sum_{n=0}^\infty \delta^n v_{\theta,n}, \quad v_r = \sum_{n=0}^\infty \delta^n v_{r,n}, \quad v_z = \sum_{n=1}^\infty \delta^n v_{z,n}. \tag{4.14}$$

Note that for v_z the expansion in terms of δ starts with $n = 1$, as can be verified by substituting the expansion for v_r into the continuity equation (4.2). Moreover, substitution of (4.14) into (4.9) yields

$$\omega_{\theta,0} = \frac{\partial v_{r,0}}{\partial z} \tag{4.15}$$

at lowest order $\delta \downarrow 0$.

In addition, it is also necessary to compare the magnitudes of the Reynolds and Rossby numbers to the magnitude of δ. For this reason, the Reynolds and Rossby numbers are quantified in terms of powers of δ, according to

$$\mathrm{Re} = A\delta^k, \qquad \mathrm{Ro} = (B\delta^l)^{-1}, \tag{4.16}$$

where k and l are integers to be defined; and A and B are constants of order unity. The Ekman number is then written as:

$$\mathrm{Ek} = \frac{2}{AB}\delta^{-m}, \tag{4.17}$$

where $m = k + l + 2$.

Equations (4.14) and (4.16) are then substituted into (4.6) and (4.7). Depending on the values of k and l (or equivalently Re and Ro), nine flow regimes can be identified; each of them will be described next. The details can be found in Appendix B.

4.3.3 Numerical simulations

To study the evolution of the flow for different values of the control parameters (Ro, Re, and δ), a finite-element code (COMSOL) is used to solve the full Navier–Stokes equations for an incompressible and azimuthally symmetric flow.

The equations were solved in the (r, z)-plane, where a no-slip condition was used at $z = 0$ and a stress-free condition at $z = 1$. Furthermore, a stress-free condition was also imposed at $r = L_c/L_0 = 12$ (about ten times the radius of maximum velocity of the Lamb–Oseen vortex) to reduce the influence of this boundary.

As can be seen, the initial condition (4.3) does not satisfy the no-slip condition at the bottom. However, the code adjusts the initial flow instantaneously to satisfy the bottom boundary condition. To further analyze the importance of the initial vertical profile, some simulations were initialized with different vertical profiles, e.g. a Poiseuille-like profile $\sin(\pi z/2)$ or a profile with a thin boundary layer at the bottom and an interior that is uniform in z.

Both the time and spatial resolution were evaluated by performing several numerical simulations with different resolutions, and verifying that the results converged to the same solution.

All the simulations were performed for Re $= 1000$, which is typical in laboratory experiments. Furthermore, it has been previously shown that the dynamics
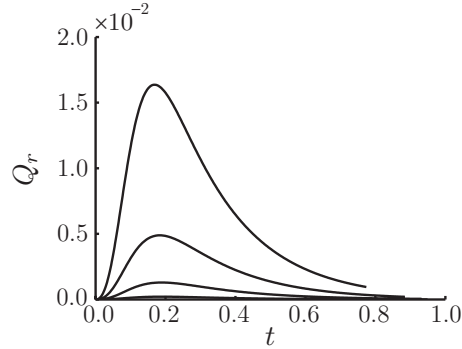
Figure 4.2 – *Evolution of the normalized energy of the radial velocity component Q_r as a function of time for simulations with* Ro $= \infty$, Re $= 1000$ *and* δ^2Re $=$ 5, 10 *and* 20.

of shallow swirl flows without background rotation are governed only by the parameter δ^2Re (Duran-Matute et al., 2010). The parameter space was explored by varying either the aspect ratio δ or the Rossby number Ro, while keeping the other control parameters fixed.

4.4 Limiting cases: Ro ≫ 1 and Ro ≪ 1

4.4.1 The limit of weak background rotation (Ro ≫ 1)

Figure 4.2 presents the evolution of the normalized kinetic energy Q_r for three numerical simulations with Re $= 1000$, Ro $= \infty$ and δ^2Re $= 5$, 10, and 20. Initially, the secondary flow is set up with its energy increasing until Q_r reaches a maximum. Later, the secondary motion decays faster than the primary motion. To simplify our study, we only focus on the maximum in time of the quantities used to quantify the strength of the secondary motion: $\max(Q_r)$, $\max(Q_z)$, $\max(q_r)$, and $\max(\Delta)$.

It is here convenient to define the parameter

$$h_{\mathrm{Re}} \equiv \frac{2}{\delta \, \mathrm{Re}^{1/2}} \tag{4.18}$$

to characterize the flow without background rotation. As it will be shown later from an analogy with the rotating case, h_{Re} can be considered as the nondimensional thickness of the boundary layer at the bottom for the non-rotating case.

Figure 4.3 shows the maximum in time of Q_r, Q_z, q_r, and Δ as a function of h_{Re}. For all quantities, two scaling regimes are observed: one for $h_{\mathrm{Re}} \lesssim 0.2$ and another for $h_{\mathrm{Re}} \gtrsim 0.6$, with a smooth transition in between.
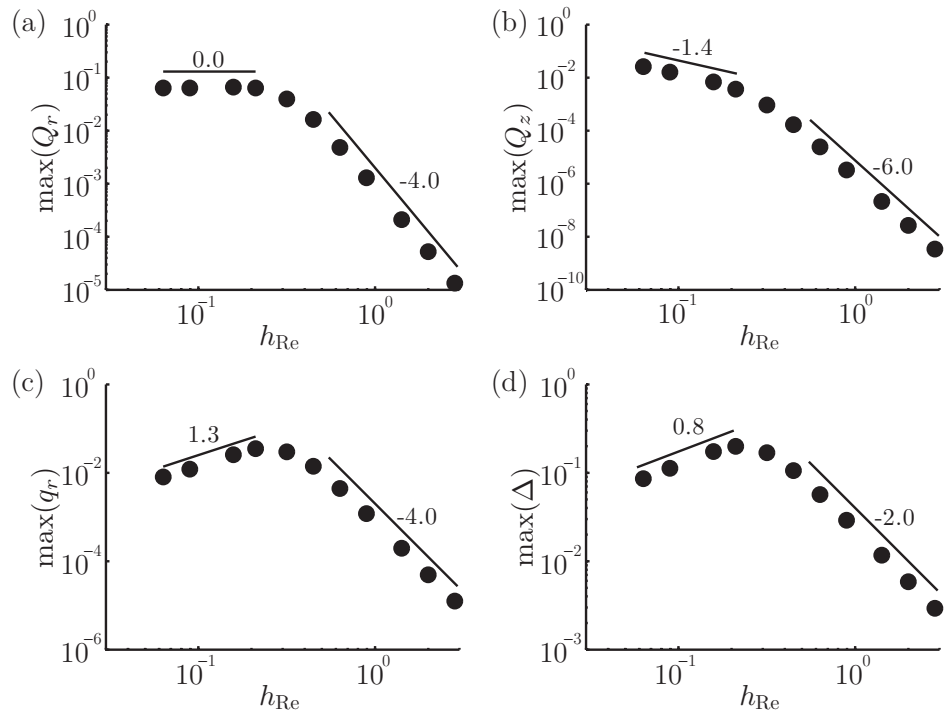
Figure 4.3 – *Strength of the secondary flow for the case without background rotation ($\mathrm{Ro} = \infty$) as a function of h_{Re}. (a) Maximum of the kinetic energy associated with the radial velocity component, (b) maximum of the kinetic energy associated to the vertical velocity component, (c) maximum of the kinetic energy of the secondary motion at the surface, and (d) maximum of the normalized horizontal divergence at the surface. The bullets represent the numerical results.*

Regime AI: Ro $\gg$ 1, $h_{\mathrm{Re}} \gtrsim 0.6$

As seen in figure 4.3, the importance of the secondary motion decreases with increasing h_{Re}-values for $h_{\mathrm{Re}} \gtrsim 0.6$. In fact, the velocity components scale as

$$\frac{v_r}{v_\theta} = \mathcal{O}(h_{\mathrm{Re}}^{-2}) = \mathcal{O}(\delta^2 \mathrm{Re}), \tag{4.19}$$

$$\frac{v_z}{v_\theta} = \mathcal{O}(\delta\, h_{\mathrm{Re}}^{-2}) = \mathcal{O}(\delta^3 \mathrm{Re}). \tag{4.20}$$

This is the characteristic scaling for the case of weak background rotation (Ro $\gg$ 1) when the convective acceleration can be neglected and bottom friction dominates, as described in the Appendix B.1.

In this regime, the governing equations to lowest order ($\delta \downarrow 0$) are

$$\frac{\partial v_\theta}{\partial t} - \frac{\partial^2 v_\theta}{\partial z^2} = 0, \tag{4.21}$$

$$\frac{\partial \omega_\theta}{\partial t} - \frac{\partial^2 \omega_\theta}{\partial z^2} = \frac{\delta^2 \mathrm{Re}}{r} \frac{\partial v_\theta^2}{\partial z}, \tag{4.22}$$

if $v_r = v_z = 0$ at $t = 0$.

The evolution of the azimuthal velocity component is governed by the diffusion equation (4.21) since it is dominated by bottom friction. From this equation it can be seen that the vertical profile of the azimuthal velocity tends to a Poiseuille-like profile of the form $\sin(\pi z/2)$ and that v_θ decays exponentially as $v_\theta \propto e^{-\pi^2 t/4}$. Since, the evolution of the primary motion is independent of the secondary motion, the flow is Q2D in this regime.

Regime AII: Ro $\gg$ 1, $h_{\mathrm{Re}} \lesssim 0.2$

As the value of h_{Re} is decreased (the aspect ratio δ increased), bottom friction becomes less dominant, and the azimuthal velocity $v_\theta(r, z)$ is redistributed by the secondary motion. This results in a qualitative change in the flow. While for $h_{\mathrm{Re}} \gtrsim 0.6$ the azimuthal velocity has a Poiseuille-like profile, for $h_{\mathrm{Re}} \lesssim 0.2$ the azimuthal velocity is composed of two regions: a boundary layer at the bottom and an inviscid interior. This change is reflected in the values of q_r and Q_r, which are equal for $h_{\mathrm{Re}} \gtrsim 0.6$ but different for $h_{\mathrm{Re}} \lesssim 0.2$ (see figure 4.3).

Due to the qualitative change in the vertical profile of the azimuthal velocity, the relative strength of the secondary motion at the surface (given by q_r and Δ) increases with increasing h_{Re} values (decreasing values of the aspect ratio δ). This observation contradicts, at least outside the boundary layer, the usual assumption that the relative strength of the secondary motion should decrease with decreasing δ-values.

In addition, the qualitative change in the flow is reflected as a change in the scaling of the velocity components. However, it has been observed that the scaling

of the velocity components for $h_{\mathrm{Re}} \lesssim 0.2$ depends on the vertical profile of the initial condition, in contrast with the previous regime for which the scaling does not depend on the precise form of the initial vertical structure of the swirl. This dependence is due to the presence of strong non-linear inertial oscillations which can be excited in the inviscid interior if the primary flow depends strongly on z initially. The energy of these oscillations depends on the initial vertical profile and adds up to the energy of the secondary motion. Hence, the scaling laws presented in figure 4.3 for $h_{\mathrm{Re}} \lesssim 0.2$ are only characteristic for the case where the initial condition is independent of z, i.e. for $v_\theta(r, z, t = 0) = f(r)$.

Since the non-linear terms in (4.1) cannot be neglected, the scaling laws for the velocity components in this regime could not be recovered using perturbation analysis. However, it is clear that the secondary motion strongly modifies the primary motion, and hence, the flow is not Q2D.

Transition AIII: $\mathrm{Ro} \gg 1$, $0.6 \gtrsim h_{\mathrm{Re}} \gtrsim 0.2$

The transition between the two scaling regimes occurs for $0.6 \gtrsim h_{\mathrm{Re}} \gtrsim 0.2$. In this transition, bottom friction is of the same order as inertia forces (see Appendix B.3), and the secondary motion starts to influence the evolution of the primary motion.

Figure 4.4 shows the typical decay time τ of the azimuthal velocity. This decay time is obtained by fitting an exponential decay to the average value of the azimuthal velocity in the volume for $r \leq 1$ as a function of time. For $h_{\mathrm{Re}} \gtrsim 0.6$, the typical decay time is the Rayleigh decay time $\tau_R = 4/\pi^2$ [equivalent to $4H^2/(\pi^2\nu)$ in dimensional units] which is typical for shallow flows dominated by bottom friction (Satijn et al., 2001). For $h_{\mathrm{Re}} \lesssim 0.2$, the velocity decay is mainly due to the momentum diffusion in the boundary layer, and the decay time related to the boundary layer thickness in the form $\tau = \tau_{\mathrm{Re}} = h_{\mathrm{Re}}$. By equating the typical decay times τ_R and τ_{Re}, the critical boundary layer thickness $h_{\mathrm{Re},C} = 4/\pi^2$ for the transition between regimes AI and AII can be obtained.

4.4.2 The limit of strong background rotation ($\mathrm{Ro} \ll 1$)

In the limit of strong rotation, we performed simulations for $\mathrm{Ro} = 0.1$, $\mathrm{Re} = 1000$, and different values of the aspect ratio δ, i.e. different values of the Ekman number Ek. This section is devoted exclusively to cyclonic vortices ($U > 0$). In Section 4.5.2, we will discuss the difference between cyclonic and anticyclonic vortices.

Figure 4.5 shows the azimuthal velocity distribution in the (r, z)-plane for two simulations with $\mathrm{Ro} = 0.1$ and two different aspect ratios at a characteristic time. A clear difference can be observed between the two simulations: for the shallower case [figure 4.5 (a)] the vertical profile resembles a Poiseuille flow, while for the deeper case [fig. 4.5 (b)] the flow is composed by a thin Ekman boundary layer at the bottom and a geostrophic interior with small vertical gradients above the boundary layer. In the case of flows subjected to strong rotation, the horizontal boundary
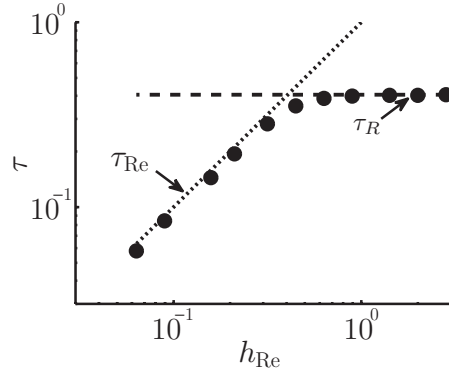
Figure 4.4 – *Typical decay time of the primary motion in the limit of no background rotation (*Ro $= \infty$*). The decay time τ is plotted as a function of the boundary layer thickness h_{Re} for simulations with* Re $= 1000$, Ro $= \infty$*, and different values of δ. The dashed line represents the Rayleigh decay time $\tau = \tau_R$, and the dotted line the decay time $\tau = \tau_{\mathrm{Re}}$ associated with the boundary layer*
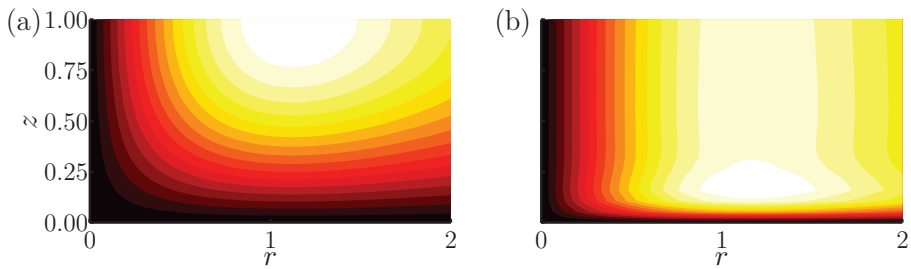
Figure 4.5 – *Azimuthal velocity distribution in the vortex core in the case of strong rotation* Ro $= 0.1$ *at* $t = 0.2$*. (a)* Re $= 1000$ *and* Ek $= 0.4$ *(*Ek$^{-1/2} \approx 1.58$*). (b)* Re $= 1000$ *and* Ek $= 0.005$ *(*Ek$^{-1/2} \approx 14.14$*)*

layers are known as Ekman boundary layers, and their thickness is defined as

$$h_{\mathrm{Ek}} \equiv \mathrm{Ek}^{1/2} \tag{4.23}$$

(see Pedlosky, 1987).

Figure 4.6 shows the maximum in time of Q_r, Q_z, q_r, and Δ, the quantities used to characterize the flow's two-dimensionality, as a function the Ekman boundary layer thickness h_{Ek}. For all quantities, two scaling regimes are observed: one for $h_{\mathrm{Ek}} \lesssim 0.2$ and another for $h_{\mathrm{Ek}} \gtrsim 0.6$. Between these two regimes there is a smooth transition.

Even though the maximum of the normalized energy associated with the vertical velocity component Q_z varies little for flows with small boundary layer thickness $h_{\mathrm{Ek}} \lesssim 0.2$, the maxima of Q_r, q_r, and Δ increase with increasing Ek values (i.e. with decreasing depth). This means that shallowness does not reduce the magnitude of the vertical velocity. The decrease in the relative strength of the secondary motion due to the vertical confinement occurs only if $h_{\mathrm{Ek}} \gtrsim 0.6$.

Regime BI: $\mathrm{Ro} \ll 1$, $h_{\mathrm{Ek}} \gtrsim 0.6$

The governing equations (4.6) and (4.7) simplify, at lowest order ($\delta \downarrow 0$), to

$$\frac{\partial v_\theta}{\partial t} - \frac{\partial^2 v_\theta}{\partial z^2} = 0, \tag{4.24}$$

$$\frac{\partial \omega_\theta}{\partial t} - \frac{\partial^2 \omega_\theta}{\partial z^2} = \frac{2}{\mathrm{Ek}} \frac{\partial v_\theta}{\partial z}, \tag{4.25}$$

when momentum diffusion due to bottom friction dominates over both the Coriolis and the convective accelerations. Since all the terms in (4.24) and (4.25) are of the same order, the velocity components scale as

$$\frac{v_r}{v_\theta} = \mathcal{O}\left(\frac{1}{\mathrm{Ek}}\right), \qquad \frac{v_z}{v_\theta} = \mathcal{O}\left(\frac{\delta}{\mathrm{Ek}}\right), \tag{4.26}$$

in this regime. These scaling laws for the velocity components are equivalent to the numerically obtained scalings of $\max(Q_r)$, $\max(Q_z)$, $\max(q_r)$, and $\max(\Delta)$ observed in figure 4.6 for $h_{\mathrm{Ek}} \gtrsim 0.6$.

In this regime, due to the importance of bottom friction, the evolution of v_θ is governed, at lowest order, by the diffusion equation (4.24). This results in a Poiseuille-like vertical profile of v_θ [see figure 4.5 (a)]. Furthermore, the secondary motion does not affect the evolution of the primary motion, i.e. vortex stretching is absent at lowest order, and the primary flow can be considered as Q2D.

Note that, for strong rotation ($\mathrm{Ro} \ll 1$), it is only in this regime that shallowness reduces the strength of the secondary motion.
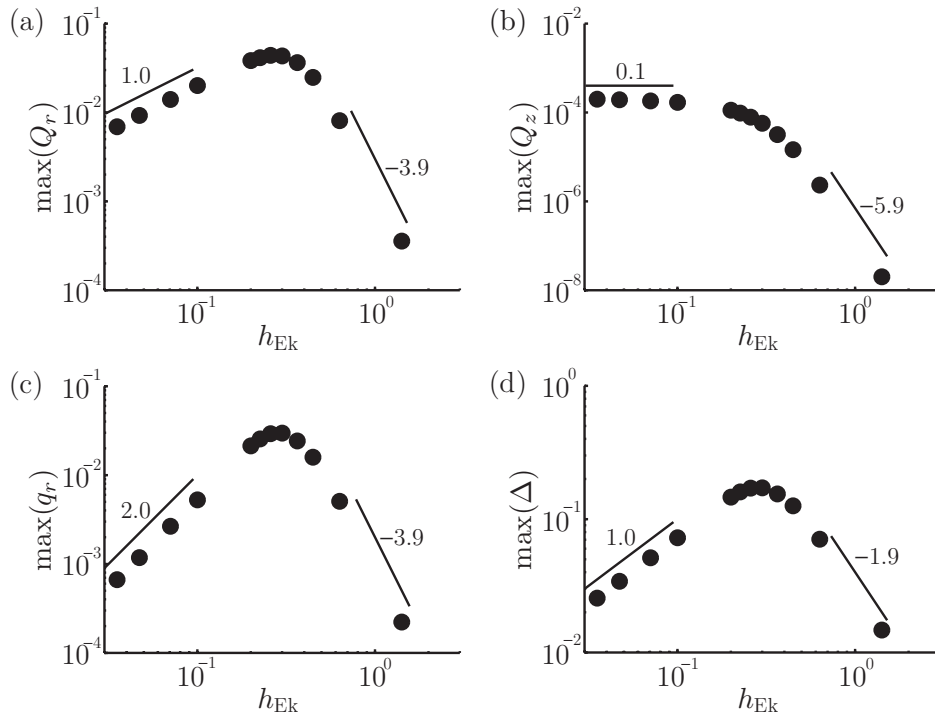
Figure 4.6 – *Strength of the secondary flow for the case of strong rotation as a function of the Ekman boundary layer thickness h_{Ek}. (a) Maximum of the energy of the radial velocity component integrated over the volume, (b) maximum of the energy of the vertical velocity component integrated over the volume, (c) maximum of the energy of the secondary flow at the surface, and (d) maximum of the normalized horizontal divergence at the surface for simulations with $\mathrm{Re} = 1000$ and $\mathrm{Ro} = 0.1$.*

Regime BII: Ro $\ll$ 1, $h_{\mathrm{Ek}} \lesssim 0.2$

For $h_{\mathrm{Ek}} \lesssim 0.2$, bottom friction can be neglected except in a thin boundary layer close to the bottom. In this way, the flow is divided into two regions: a geostrophic interior and an Ekman boundary layer at the bottom, as shown in figure 4.5.

In the geostrophic interior, the evolution of the azimuthal velocity is governed by

$$\frac{\partial v_\theta}{\partial t} + \mathrm{Ek}^{1/2} v_\theta = 0, \tag{4.27}$$

$$\frac{\partial v_\theta}{\partial z} = 0, \tag{4.28}$$

as derived in Appendix B.5. These equations are in agreement with the equations derived by Kloosterziel & van Heijst (1991) for any value of δ. As can be seen, the primary flow in the geostrophic interior is independent of the vertical coordinate, as stated by the Taylor–Proudman theorem (see Pedlosky, 1987), and its decay time is given by the dimensionless Ekman decay time $\tau_{\mathrm{Ek}} = \mathrm{Ek}^{1/2}$, in agreement with linear Ekman theory. Furthermore, the radial profile of the primary flow is not modified by the secondary flow. Hence, the primary flow can be considered as Q2D for Ro $\ll$ 1 and $h_{\mathrm{Ek}} \lesssim 0.2$.

In the geostrophic interior, the velocity components scale like

$$\frac{v_r}{v_\theta} = \mathcal{O}(\mathrm{Ek}^{1/2}), \qquad \frac{v_z}{v_\theta} = \mathcal{O}(\delta \mathrm{Ek}^{1/2}). \tag{4.29}$$

These scaling laws are in agreement with the numerically obtained scaling: $\max(q_r) \sim \mathrm{Ek}$ and $\max(\Delta) \sim \mathrm{Ek}^{1/2}$ for $h_{\mathrm{Ek}} \lesssim 0.2$, as observed in figure 4.6(c) and (d). It can also be observed, by comparing figure 4.6(c) with figure 4.6(a), that Q_r does not scale as predicted by (4.29) since the integration over the volume takes into account the Ekman boundary layer. In this way, the division of the flow into two regions is clearly reflected in a difference in the scaling of $\max(q_r)$ and $\max(Q_r)$ for $h_{\mathrm{Ek}} \lesssim 0.2$.

It must be pointed out that, in this regime, the scaling and the general evolution of the primary flow depends on the initial vertical profile of the azimuthal velocity. In fact, note that the initial condition that $\partial v_\theta / \partial z = 0$ is necessary for (4.27) and (4.28) to hold. Carnevale et al. (1997) have shown through numerical simulations that a rapid instability occurs for small Rossby numbers, and the vortex tubes can break up if the initial columnar vortex is strongly perturbed. A similar problem occurs here if the initial vertical profile varies greatly with z. Hence, the scaling presented here is only valid for an initial vortex that is independent of the vertical coordinate.

Transition BIII: Ro $\ll$ 1, $0.6 \gtrsim h_{\mathrm{Ek}} \gtrsim 0.2$

In the transition between regimes BI and BII, viscous forces and the Coriolis force are in balance while they dominate over advection. In other words, the Ekman

boundary layer thickness is of the same order as the fluid depth, and the governing equations at lowest order for the whole fluid column are the same as for the Ekman boundary layer:

$$\frac{\partial v_\theta}{\partial t} - \frac{\partial^2 v_\theta}{\partial z^2} = -\frac{2}{\mathrm{Ek}} v_r, \tag{4.30}$$

$$\frac{\partial \omega_\theta}{\partial t} - \frac{\partial^2 \omega_\theta}{\partial z^2} = \frac{2}{\mathrm{Ek}} \frac{\partial v_\theta}{\partial z}. \tag{4.31}$$

These equations also govern the flow in regimes BI and BII. However, in these regimes, (4.30) and (4.31) can be further simplified: the Coriolis force in (4.30) can be neglected in regime BI, and the flow can be divided into two regions in regime BII.

In this transitional regime, the secondary motion modifies the primary motion according to (4.30). However, by close inspection, it can be seen that the secondary motion does not modify the radial distribution of the azimuthal velocity but only its vertical distribution since (4.30) and (4.30) are independent of r. Hence, the flow can be considered as Q2D in this regime.

In figure 4.7, the typical decay time of the primary flow is plotted as a function of the Ekman boundary layer thickness h_{Ek}. The decay time is obtained by fitting an exponential function to the average of the azimuthal velocity for $r \leq 1$ as a function of time. The typical decay time of the primary motion is given by the Ekman time scale $\tau_{\mathrm{Ek}} = \mathrm{Ek}^{1/2}$ [equivalent to $H/(\nu\omega)^{1/2}$ in dimensional form] in agreement with linear Ekman theory only for $h_{\mathrm{Ek}} \lesssim 0.2$. However, for vortices with large Ekman boundary layer thickness as compared to the total fluid depth ($h_{\mathrm{Ek}} \gtrsim 0.6$), the typical decay time of the kinetic energy of the primary motion is the Rayleigh decay time $\tau_R = 4/\pi^2$ [equivalent to $4H^2/(\pi^2\nu)$ in dimensional form]. By equating the two different decay times τ_R and τ_{Ek}, it is possible to obtain the critical Ekman boundary layer $h_{\mathrm{Ek}} = 4/\pi^2$ for the transition between the two regimes.

4.4.3 Comparison between the limiting cases Ro ≫ 1 and Ro ≪ 1

In the limiting cases, the flow dynamics depends only on the value of $h_{\mathrm{Re}} = 2/(\delta\,\mathrm{Re}^{1/2})$ for Ro ≫ 1 and $h_{\mathrm{Ek}} = \mathrm{Ek}^{1/2}$ for Ro ≪ 1. For each limiting case, two scaling regimes where found: (i) a viscous regime where the vertical profile of the azimuthal velocity tends to a Poiseuille-like vertical profile $\sin(\pi z/2)$, and (ii) a regime where the flow is composed of a bottom boundary layer and an inviscid interior. The two regimes are separated by a smooth transition.

From the previous sections, it can be seen that there is a strong analogy between h_{Ek} and h_{Re}, which is detailed further in table I. This analogy clearly implies that h_{Re} can be considered as the typical boundary layer thickness in the vortex core ($r \leq 1$) for Ro ≫ 1.
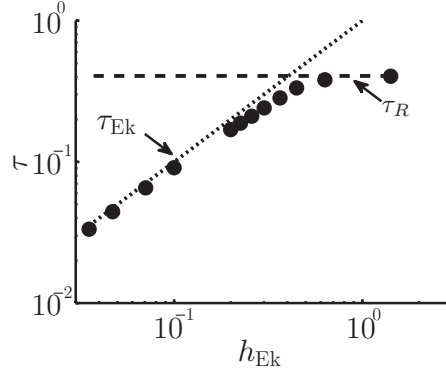
Figure 4.7 – *Typical decay time of the primary motion in the limit of strong rotation Ro $\ll$ 1. The typical time τ is plotted as a function of the thickness of the Ekman boundary layer h_{Ek} for simulations with Re $= 1000$, Ro $= 0.1$, and different values of δ. The bullets represent results from numerical simulations. The dashed line represents the Rayleigh decay time $\tau = \tau_R$, while the dotted line represents the Ekman decay time $\tau = \tau_{\mathrm{Ek}}$.*

Limit	Ro $\gg$ 1	Ro $\ll$ 1
Governing parameter	$h_{\mathrm{Re}} = 2/(\delta\,\mathrm{Re}^{1/2})$	$h_{\mathrm{Ek}} = \mathrm{Ek}^{1/2}$
Viscous regime limit	$h_{\mathrm{Re}} \gtrsim 0.6$	$h_{\mathrm{Ek}} \gtrsim 0.6$
Transitional regime	$0.6 \gtrsim h_{\mathrm{Re}} \gtrsim 0.2$	$0.6 \gtrsim h_{\mathrm{Ek}} \gtrsim 0.2$
Typical decay time	$\tau = 4/\pi^2$ for $h_{\mathrm{Re}} \lesssim 0.2$ $\tau = h_{\mathrm{Re}}$ for $h_{\mathrm{Re}} \gtrsim 0.6$	$\tau = 4/\pi^2$ for $h_{\mathrm{Ek}} \lesssim 0.2$ $\tau = h_{\mathrm{Ek}}$ for $h_{\mathrm{Ek}} \gtrsim 0.6$
Critical boundary layer thickness	$h_{\mathrm{Re}} = 4/\pi^2$	$h_{\mathrm{Ek}} = 4/\pi^2$

Table I – *Similarities between the two limiting cases: Ro $\gg$ 1 and Ro $\ll$ 1.*
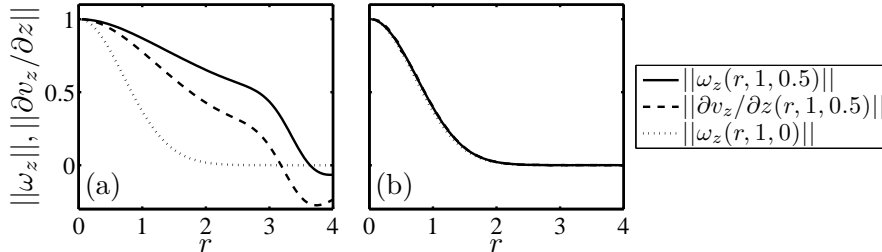
Figure 4.8 – *Radial profiles at the surface for the normalized vertical vorticity $||\omega_z|| = \omega_z/\max(\omega_z)$ and the normalized vertical gradient of the vertical velocity $||\partial v_z/\partial z|| = (\partial v_z/\partial z)/\max(\partial v_z/\partial z)$ for two simulations: (a) Ro $= \infty$, Re $= 1000$ and $h_{\mathrm{Re}} = 0.11$, and (b) Ro $= 0.1$, Re $= 1000$ and $h_{\mathrm{Re}} = 0.71$ ($h_{\mathrm{Ek}} = 0.16$) at time $t = 0.1$. The radial profile for ω_z at the surface and time $t = 0$ is shown as reference.*

In spite of the strong analogy between both limits, there is also an important difference regarding the two-dimensionality of the flow: for the case of no background rotation, the flow is strictly Q2D only in the viscous regime, when $h_{\mathrm{Re}} \gtrsim 0.6$, while for the case of strong background rotation, the flow can be considered as Q2D independently of the Ekman boundary layer thickness h_{Ek}. This difference not only lies in the distinct values for the strength of the secondary motion, but also in important qualitative differences between both limits.

For example, figure 4.8 shows the normalized radial profiles for the azimuthal velocity and the vertical gradient of the vertical velocity (which is equal to the horizontal divergence) at the surface ($z = 1$) at time $t = 0.1$ for two simulations: one with Ro $= \infty$, Re $= 1000$ and $h_{\mathrm{Re}} = 0.11$, and one with Ro $= 0.1$, Re $= 1000$ and $h_{\mathrm{Re}} = 0.71$ ($h_{\mathrm{Ek}} = 0.16$). The radial profile of the azimuthal velocity at time $t = 0$ is also shown as reference. These two simulations were chosen because they have a similar maximum q_r-values: $\max(q_r) \approx 0.026$. For the case of no background rotation, the radial distributions of the vertical vorticity and horizontal divergence are different. This leads to the deformation of the radial profile of the azimuthal velocity partially due to vortex stretching in the z-direction, which is proportional to the horizontal divergence. On the other hand, for the case of strong background rotation, the radial distribution of the azimuthal velocity component remains unchanged although the decrease in the strength of the azimuthal velocity is caused by vortex stretching exerted by the secondary motion. This is due to the particular distribution of the secondary motion driven by the Ekman boundary layer in which the radial distribution of the horizontal divergence coincides with the radial distribution of the vertical vorticity.

Another important qualitative difference between the two limits resides in the evolution of the boundary layer thickness. For the case Ro $= \infty$, the boundary layer thickness depends on the azimuthal velocity in the inviscid interior. Furthermore, since the azimuthal velocity in the interior is a function of r and t, the boundary layer thickness also varies with r and t. Consequently, outside the viscous regime,
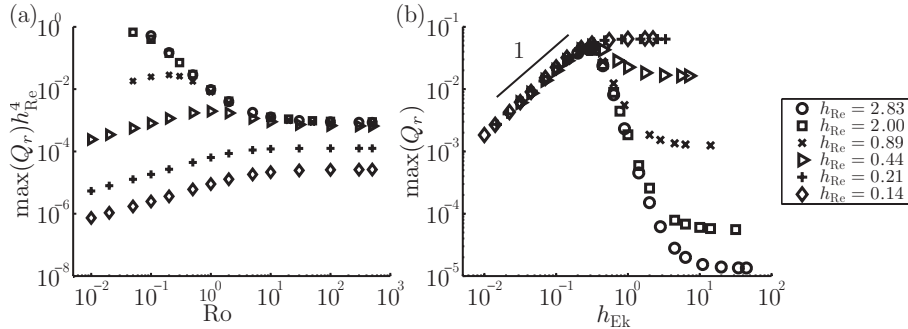
Figure 4.9 – *Strength of the secondary motion as a function of the rotation rate. Maximum of the normalized kinetic energy of the radial velocity component in the vortex core* $\max(Q_r)$ *as a function of (a) the Rossby number Ro and (b) the dimensionless Ekman boundary layer thickness h_{Ek} for different values of the aspect ratio δ and Re $= 1000$. Note that $\max(Q_r)$ has been scaled, for convenience, by h_{Re}^4 in (a).*

the local damping rate, which is related to the boundary layer thickness, is neither homogeneous in the r-direction nor in time for Ro $= \infty$. On the other hand, the thickness of the Ekman boundary layer and the associated damping rate is homogeneous in the r-direction and constant in time for Ro $\ll 1$.

Both the quantitative and qualitative differences in the two limiting cases are related to the coupling between the primary and secondary motions. This coupling is given by the term (4.10) in (4.7), the convective acceleration, $\boldsymbol{v} \cdot \boldsymbol{\nabla} v_\theta$, in (4.6), and the Coriolis acceleration, $-\mathrm{Ek}^{-1} v_r$, in (4.6). For the case of strong background rotation (Ro $\ll 1$), the coupling term (4.10) reduces to $\mathrm{Ek}^{-1} \partial v_\theta / \partial z$, and the convective acceleration is negligible. On the other hand, for the case of weak background rotation (Ro $\gg 1$), the coupling term (4.10) reduces to $\delta^2 \mathrm{Re}\, r^{-1} \partial v_\theta^2 / \partial z$, and the primary motion is modified exclusively through convective acceleration. It can be clearly seen that for the case of strong background rotation, the coupling between the primary and secondary motion is linear, while this coupling is non-linear for the case of no background rotation.

4.5   Intermediate rotation rates

4.5.1   Cyclonic vortices

In this section, we present results from numerical simulations where the Rossby number was varied while keeping the aspect ratio δ and the Reynolds number Re fixed. In this way, the dependence of the flow dynamics on the rotation rate Ω is studied.

Figure 4.9(a) shows the maximum of the normalized energy of the radial velocity component integrated over the volume of the vortex core, $\max(Q_r)$, as a function of the Rossby number Ro for simulations of cyclonic vortices $U > 0$ with

Re = 1000 and different values of the aspect ratio δ, i.e. different values of h_{Re}. Note that the maximum of Q_r has been normalized with h_{Re}^4 for presentation purposes, and that the Rossby number is related to the boundary layer thickness of the limiting cases:

$$\mathrm{Ro} = 2 \left(\frac{h_{\mathrm{Ek}}}{h_{\mathrm{Re}}} \right)^2. \tag{4.32}$$

As can be seen, for large Ro-values (Ro $\gtrsim$ 100), the value of $\max(Q_r)$ remains almost constant as rotation is increased, implying that rotation has a negligible effect on the secondary motion. As the value of the Rossby number reaches Ro $\approx$ 100, the effect of rotation becomes noticeable. If $h_{\mathrm{Ek}} \gtrsim h_{\mathrm{Ek},C} = 4/\pi^2$, the strength of the secondary motion, given by Q_r increases for decreasing Ro-values and Ro $\lesssim$ 100 until a maximum is reached, and then it starts to decrease. If $h_{\mathrm{Ek}} \lesssim h_{\mathrm{Ek},C} = 4/\pi^2$, the energy of the secondary motion only decreases for decreasing Ro-values.

Figure 4.9(b) shows the maximum of Q_r as a function of the Ekman boundary layer thickness, h_{Ek}. It can be seen that Q_r becomes independent of h_{Re} for $h_{\mathrm{Ek}} \lesssim h_{\mathrm{Ek},C} = 4/\pi^2$. Furthermore, Q_r becomes proportional to h_{Ek} in this region of the parameter space, indicating that the secondary motion is due to Ekman pumping.

For $h_{\mathrm{Re}} \gtrsim 0.6$, v_θ has a Poiseuille-like vertical profile in the non-rotating case. As rotation is increased, this vertical profile remains unchanged since the azimuthal flow is still governed by a diffusion equation, thus the flow is still Q2D. On the other hand, the strength of the secondary motion increases due to the added effect of rotation in the coupling term (4.10). This is the regime CI detailed in Appendix B.7.

However, due to the increase in the strength of the secondary motion, the advective acceleration due to the secondary motion can become important. In this case, no term in (4.6) and (4.7) can be neglected. This is the regime CIII for intermediate rotation rates.

Finally if $h_{\mathrm{Re}} \lesssim 0.3$, v_θ is composed of an inviscid interior and a boundary layer with a typical thickness h_{Re} for Ro $= \infty$. As rotation is increased, the strength of the secondary motion and its structure remain unchanged until the critical Ekman boundary layer thickness $h_{\mathrm{Ek},C} = 4/\pi^2$ is reached, and the inviscid flow becomes geostrophic and the secondary motion is described by linear Ekman theory.

4.5.2 Cyclone–anticyclone asymmetry

The strength of the secondary motion can be increased or decreased depending on the direction of the primary flow as compared to the rotation direction of the system, i.e. depending on the relative sign of

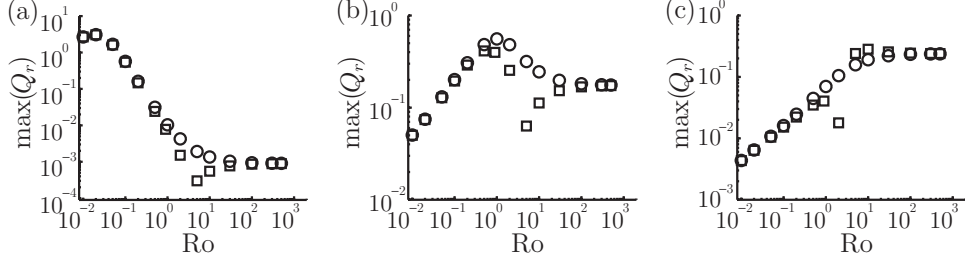$$\delta^2 \mathrm{Re} \frac{1}{r} \frac{\partial v_\theta^2}{\partial z}$$

Figure 4.10 – *Comparison of the strength of the secondary motion between cyclonic (○) and anticyclonic vortices (□) for* Re = 1000 *and three different values of* h_{Re}*: (a)* $h_{\mathrm{Re}} = 2.83$*, (b)* $h_{\mathrm{Re}} = 0.45$*, and (c)* $h_{\mathrm{Re}} = 0.14$

with respect to the sign of

$$\frac{2}{\mathrm{Ek}} \frac{\partial v_\theta}{\partial z}$$

in the term which couples (4.6) and (4.7), and which is expanded in (4.10). It is well known that strong Lamb–Oseen anticyclonic vortices, for which Ro < −1, are prone to the centrifugal instability which breaks the azimuthal symmetry of the flow (Kloosterziel & van Heijst, 1991). However, this phenomenon will not be taken into account here, and the azimuthal symmetry will be imposed even for unstable anticyclones to isolate the effect of the coupling term on the strength of the secondary motion.

Figure 4.10 shows the strength of the secondary motion, given by max(Q_r) as a function of the Rossby number Ro for both cyclones and anticyclones for simulations with: (a) $h_{\mathrm{Re}} = 2.83$, (b) $h_{\mathrm{Re}} = 0.45$, and (c) $h_{\mathrm{Re}} = 0.14$. It can be seen that the strength of the secondary motion differs between cyclones and anticyclones for $100 \gtrsim$ Ro $\gtrsim 0.2$. For example, for simulations with $h_{\mathrm{Re}} = 2.83$ and $h_{\mathrm{Re}} = 0.45$, the strength of the secondary motion for the anticyclonic vortices decreases with decreasing Ro-values for $100 \gtrsim$ Ro $\gtrsim 5$, while in the same range of Ro-values, it increases for cyclonic vortices.

However, this asymmetry is not relevant for the primary motion if the flow is Q2D. Figure 4.11 shows the radial profile of the azimuthal velocity at time $t = 0.5$ for a cyclonic and an anticyclonic vortex for three pairs of numerical simulations with (a) $h_{\mathrm{Re}} = 2$ and $h_{\mathrm{Ek}} = 3.16$; (b) $h_{\mathrm{Re}} = 0.31$ and $h_{\mathrm{Ek}} = 0.49$; and (c) $h_{\mathrm{Re}} = 0.1$ and $h_{\mathrm{Ek}} = 0.15$. All these simulations were performed with Ro = 5, for which a strong asymmetry between the strength of the secondary motion exists. In figure 4.11(a), it can be seen that the radial profile of the primary motion is equal for the anticyclone and the cyclone: this is because the flow is Q2D, and the secondary motion does not affect the primary motion. However, for the simulations shown in figure 4.11(b) and (c), there is an important difference in the evolution of the primary motion between cyclonic and anticyclonic vortices.

Note that for the simulation corresponding to figure 4.11(c), the thickness of
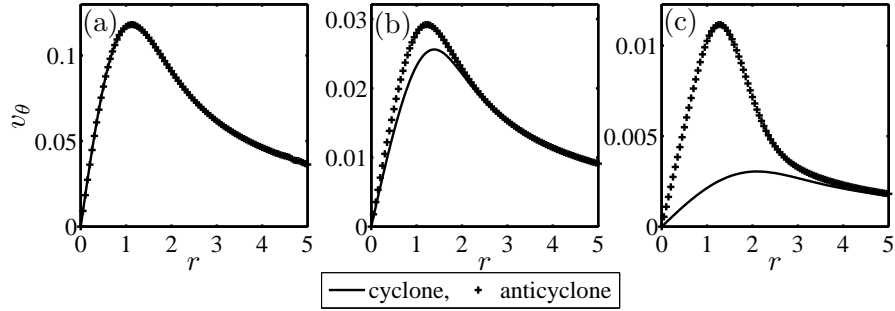
Figure 4.11 – *Radial profiles of the azimuthal velocity at the surface at $t = 0.5$ $[v_\theta(r, z = 1, t = 0.5)]$ for cyclones (solid line) and anticyclones (crosses) obtained from simulations with $\mathrm{Re} = 1000$, $\mathrm{Ro} = 5$ and three different values of h_{Re}: (a) $h_{\mathrm{Re}} = 2$, (b) $h_{\mathrm{Re}} = 0.31$, and (c) $h_{\mathrm{Re}} = 0.1$.*

the Ekman boundary layer h_{Ek} is smaller than the critical thickness $h_{\mathrm{Ek},C} = 4/\pi^2$. This means that the secondary motion is mainly due to Ekman pumping. However, the asymmetry in the evolution of the primary motion between cyclones and anticyclones suggests that linear Ekman theory is not valid since the primary motion is modified by the secondary motion through convective acceleration. Hence, this simulation does not correspond to regime BII. Instead, these characteristics are typical of regime CII, where the flow is composed of a thin boundary layer, and an inviscid interior, but the rotation is not strong enough for linear Ekman theory to govern the boundary layer dynamics. Due to their complex nature, vortices in this regime are the subject of numerous studies, usually in deeper layers; see e.g. Kloosterziel & van Heijst (1991) and Orlandi & Carnevale (1999).

In the regime CII for $\mathrm{Ro} < 1$, it is still possible to parametrize small nonlinear effects — like the cyclone–anticyclone asymmetry due to Ekman pumping — into a 2D equation for the vertical vorticity component (Zavala Sansón & van Heijst, 2000). However, these flows cannot be strictly considered as Q2D since the horizontal divergence cannot be neglected, and hence, the secondary motion still affects the evolution of the primary motion. It is still unknown if the Q2D turbulent flows governed by such an equation present the typical characteristics of 2D turbulence.

4.6 Discussion

Through a thorough exploration of the parameter space for shallow axisymmetric swirl flows subjected to background rotation, it has been found that in the limit $\delta \downarrow 0$, the flow is governed by only two non-dimensional parameters: h_{Re} and h_{Ek}.

Figure 4.12, shows a diagram of the parameter space explored with the boundaries of the different flow regimes, while table II presents a summary of the properties of each regime. In the parameter space explored, nine different flow regimes
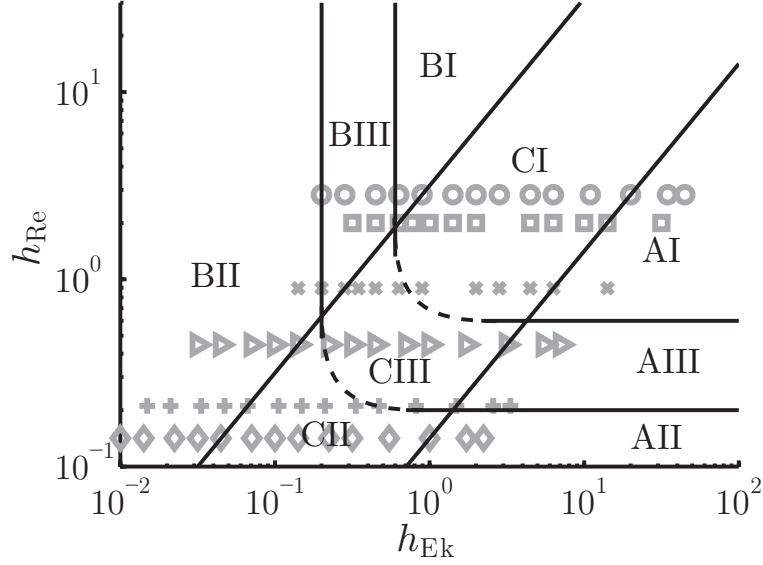
Figure 4.12 – *Diagram of the parameter space explored. The lines denote the limits of the different flow regimes. The different symbols denote the numerical simulations performed; each different symbol represents a value of h_{Re} as in figure 4.9.*

with qualitative differences were found. These differences are reflected in the value and the scaling of the relative strength of the secondary motion. The transitions between the different regimes are smooth, and the numerical values for the boundaries between the regimes are only an estimation.

One of the characteristics analyzed for each regime is the two-dimensionality of the flow, i.e. if the flow can or cannot be considered as Q2D. This property of the flow can be determined through the effects of the secondary motion on the primary motion. Not only the strength but also the spatial distribution of this secondary motion has been shown to be critical for the two-dimensionality of the flow.

It is commonly assumed that both rotation and a small aspect ratio δ enforce the two-dimensionality of the flow. However, if $\delta \ll 1$, the only simplification that can be made in all regimes is to neglect horizontal viscous diffusion. From the nine regimes found, the flow can be considered as Q2D in only five of them.

The effect of the combination of background rotation and a small aspect ratio on the two-dimensionality of flows depends on two parameters: h_{Re} and h_{Ek}. For example, consider a vortex with $h_{\mathrm{Re}} = 0.89$ and $h_{\mathrm{Ek}} = \infty$, which falls into regime AI and is then Q2D. For such a vortex, if rotation is added, h_{Re} remains constant and h_{Ek} decreases. For some value of h_{Ek}, the flow will enter regime CIII; it then becomes 3D (see the data denoted by crosses in figure 4.12). Hence, it cannot be said that the combination of background rotation and a small aspect ratio enforces the two-dimensionality of flows.

Regime	Governing equations at lowest order	Two-dimensionality	Vertical profile	Decay time
AI	(4.21) and (4.22)	Q2D	Poiseuille-like	$\tau = \tau_R$
AII	(B.14) and (B.14)	3D	Boundary layer, inviscid interior	$\tau = \tau_{\mathrm{Re}}$
AIII	(B.14) and (B.14)	3D	Boundary layer thickness of the same other as total depth	
BI	(4.24) and (4.25)	Q2D	Poiseuille-like	$\tau = \tau_R$
BII	(4.27) and (4.28)	Q2D	Ekman boundary layer and geostrophic interior	$\tau = \tau_{\mathrm{Ek}}$
BIII	(4.30) and (4.31)	Q2D	Ekman boundary layer	
CI	(B.59) and (B.60)	Q2D	Poiseuille-like	$\tau = \tau_R$
CII	Full equations	3D	Boundary layer and inviscid interior	
CIII	Full equations	3D	Boundary layer thickness similar to the total depth.	

Table II – *Summary of the properties of each regime*

When considering a problem with a small parameter, perturbation analysis is useful to simplify the equations and obtain the governing equations at lowest order. In the current chapter, we have focused on shallow flows ($\delta \ll 1$), and hence, we have performed perturbation analysis with δ as the small parameter. For strong rotation, Ro $\ll 1$ and Ek $\ll 1$, such an analysis can also be performed to further understand the importance of the convective acceleration in the evolution of the flow taking either Ro or Ek as the small parameter of the problem. In this way, a better insight into regimes CII and CIII can be reached; see e.g. Zavala Sansón & van Heijst (2000), Ishida & Iwayama (2006), Hart (2000), and Brink (1997).

4.7   Conclusions

It is usually assumed that both shallowness and background rotation enforce the two-dimensionality of flows. In the current chapter, we have shown that this is not necessarily true. Instead, the two-dimensionality of the flow depends in a complicated way on the problem parameters.

To determine if a flow is Q2D, a comparison was made between ideal Q2D flows as obtained by perturbation analysis for a small aspect ratio $\delta \ll 1$ and results from numerical simulations. Through this comparison, important insight has been gained into the effects of shallowness and background rotation on the dynamics of shallow flows.

Usually the reason why rotation is said to enforce the two-dimensionality of flows is by the reduction of the vertical gradients as stated by the Taylor–Proudman theory. When the thickness of the Ekman boundary layer is of the same order as the fluid depth, the limited depth of the fluid does not allow for the formation of columnar structures. However, we have shown that the flow can always be considered as Q2D for sufficiently strong rotation (Ro $\lesssim 0.2$) independently of the aspect ratio so even when no columnar structures can be formed. This can be attributed to the linearity of the equations governing the flow at lowest order.

Furthermore, the flow can always be considered as Q2D if the fluid depth is small compared to the typical boundary layer thickness. This condition replaces the usual condition based on the continuity equation stating that merely a small aspect ratio is sufficient to consider shallow flows as Q2D.

Chapter 5

Inertial oscillations in a monopolar vortex subjected to background rotation[i]

5.1 Introduction

It has been long known that vortices and flows in solid body rotation sustain inertial oscillations also known as Kelvin waves (Thomson, 1880). However, such oscillations continue to be a topic of interest due to their importance in the evolution of vortices. In geophysical fluid dynamics, the inertial oscillations in vortices affected by background rotation are of particular interest since such flows are common in both the ocean and the atmosphere (e.g. hurricanes and oceanic eddies).

Following the paper by Lord Kelvin (Thomson, 1880), inertial oscillations have been observed in, for example, experiments on vortices in a turbulent flow (Hopfinger, 1982) and in rotating fluids (Fultz, 1959). Furthermore, several analytical and numerical studies concerning inertial oscillations on vortices with different vorticity structures, both with and without background rotation, have been carried out.

The vortex analyzed by Lord Kelvin — now termed *Rankine vortex* — is composed of a core of uniform vorticity and an exterior with zero vorticity. Due to its shape the stability of a vortex with this profile is easily treated analytically. A formal solution to the initial value problem for small perturbations in a Rankine vortex has shown that any initial perturbation evolves exclusively as a collection of Kelvin waves, and that the physical mechanism of the propagation of the perturbations does not depend on the vortex profile (Arendt et al., 1997).

---

[i]The contents of this chapter have been adopted from the paper by Duran-Matute et al. (2009) with minor modifications.

Amongst other vortices studied, the Lamb–Oseen vortex has received special attention due to its similarity to vortices generated in the laboratory, although its profile does not allow for a complete analytical solution of the perturbed vortex. However, an exhaustive overview of the modes present in a Lamb–Oseen vortex has been obtained with the help of numerical simulations (Fabre et al., 2006). Some of the modes turned out to be related to those existing in the Rankine vortex, while others are singular, damped modes. Furthermore, a large axial-wave-number approximation has provided the spatial structure and the dispersion relation of the Kelvin modes, with good agreement with the numerical computation — even for small wave numbers (Le Dizès & Lacaze, 2005).

The axisymmetric modes form a special case since they are regular modes in a Lamb–Oseen vortex (Sipp & Jacquin, 2003; Fabre et al., 2006). Consequently, their dynamics are similar in both the Rankine vortex and the Lamb–Oseen vortex. The physical mechanism of these axisymmetric modes can be described as follows. Initially, the perturbed vortex consists of regions of high and low vorticity. Because of conservation of angular momentum, the vortex radius is smaller in the regions of high vorticity and larger in the regions of low vorticity [hence the term *sausaging modes* (Saffman, 1992)]. This shape is associated with alternating high and low pressure perturbations. Therefore, a net axial pressure gradient exists within the core and induces an axial flow. Finally the axial flow within the vortex affects the axial vorticity through the stretching-compressing mechanism. Consequently, the vortex column undergoes deformations with the varicose shape being reversed repeatedly (Fabre et al., 2006). An alternative explanation, based on the twisting of the vortex lines, was proposed by Melander & Hussain (1994).

Axisymmetric modes can affect the evolution of vortices. For instance, *sausage modes* can travel along the vortex and cause it to break down if the vortex is centrifugally unstable. These modes appear even if the vortex column is perturbed in a non-axisymmetric way (Carnevale et al., 1997; Kloosterziel et al., 2007). However, the Lamb–Oseen vortex, for example, is known to be stable to centrifugal instability, except in the case of strong anticyclones (Hopfinger & van Heijst, 1993).

The main aim of this chapter is to extend the study of the oscillations inside the vortex by including the effects of both background rotation and confinement of the fluid to a cylinder of finite dimensions. As mentioned earlier, background rotation is relevant in the study of geophysical flows. On the other hand, confinement is always necessary to contain the fluid.

We restrict our study to a monopolar vortex (swirl flow) and to the axisymmetric inertial oscillations associated with it. We focus on the spatial structure and the frequency of the different modes, as well as on the effect that these modes have on the evolution of the vortex.

Le Dizès (2008) performed an extensive study on the inviscid waves on a Lamb–Oseen vortex with background rotation, using a local Lagrangian description and a global Wentzel–Kramers–Brillouin–Jeffreys (WKBJ) approach. He found that the global modes exist in more restricted parameter regimes than the modes obtained with a local approach. Nonetheless, we will show here that this finding is only valid

in an infinite domain.

In order to characterize the waves sustained inside monopolar vortices in laboratory experiments and other real settings, we first study the inviscid modes sustained by a time-independent Rankine vortex confined to a cylinder with stress-free boundaries and subjected to background rotation. Secondly, we study the inviscid waves sustained by a more realistic vortex profile, namely the Lamb–Oseen vortex. Later, the effects of viscosity are included, and finally, the effects of a no-slip bottom are considered.

The chapter is organized as follows. In Section 5.2, we introduce the geometry and the non-dimensional parameters relevant to the problem. Section 5.3 presents the governing equations. In Section 5.4, we analyze the inviscid linear waves, while in Section 5.5, we discuss the effects of viscosity including a study of the evolution of the inertial waves in a cylinder with a no-slip bottom (Section 5.5.2). Finally, in Section 5.6, the main results and conclusions are outlined.

5.2   Definition of the problem

We consider fluid motion relative to the system rotating at a constant rate Ω about the vertical axis. The relative flow is governed by the Navier–Stokes equation:

$$\frac{D\boldsymbol{v}}{Dt} = -\frac{1}{\rho}\boldsymbol{\nabla}P + \nu\nabla^2\boldsymbol{v} - 2\boldsymbol{\Omega}\times\boldsymbol{v}, \qquad (5.1)$$

and the continuity equation for an incompressible fluid:

$$\boldsymbol{\nabla}\cdot\boldsymbol{v} = 0, \qquad (5.2)$$

where D/Dt is the material derivative, $\boldsymbol{\Omega} = \Omega\hat{\boldsymbol{z}}$ is the rotation vector of the system, $\boldsymbol{v}$ is the relative velocity, P is the generalized pressure, and ρ is the density of the fluid. The motion of the fluid is described in terms of the radial, azimuthal and axial coordinates (r,θ,z), with unit vectors $\hat{\boldsymbol{r}}$, $\hat{\boldsymbol{\theta}}$, and $\hat{\boldsymbol{z}}$ in these directions. The velocity and vorticity vectors can then be written as $\boldsymbol{v} = (v_r, v_\theta, v_z)$ and $\boldsymbol{\omega} = (\omega_r, \omega_\theta, \omega_z)$, respectively.

The flow studied consists of a vortex with peak vertical vorticity $\hat{\omega}$ and radius L confined to a cylindrical domain with height H and radius L_c, as in the previous chapter and shown in figure 4.1. The cylinder rotates around the vertical axis with angular frequency Ω. We consider all boundaries to be stress-free. (Later, in section 5.5.2, we will consider the case of a no-slip bottom). In addition, both the bottom (at $z = 0$) and the surface (at $z = H$) are flat and rigid.

Considering the parameters of the problem and performing dimensional analysis yields four nondimensional numbers that describe the problem:

$$\mathrm{Ro} \equiv \frac{\hat{\omega}_0}{2\Omega}, \quad \mathrm{Re} \equiv \frac{L_0^2|\hat{\omega}_0|}{\nu}, \quad \delta \equiv \frac{H}{L_0}, \quad \mathrm{R_c} \equiv \frac{L_c}{L_0},$$

where ν is the kinematic viscosity of the fluid, $\hat{\omega}_0$ is the initial peak vorticity of the vortex, L_0 is the initial radius of the vortex, Ro is the Rossby number, Re is the Reynolds number, δ is the aspect ratio of the vortex, and R_c is the radius of the cylinder compared to the radius of the vortex.

5.3   The governing equations

To nondimensionalize (5.1) and (5.2) , the following set of dimensionless variables is defined:

$$t' = |2\Omega + \hat{\omega}_0|t, \quad r' = \frac{r}{L_0}, \quad z' = \frac{z}{H}, \quad v'_r = \frac{v_r}{\hat{\omega}_0 L_0}, \quad v'_\theta = \frac{v_\theta}{\hat{\omega}_0 L_0}, \quad v'_z = \frac{v_z}{\hat{\omega}_0 H},$$

with the primes denoting nondimensional quantities. By assuming that the flow has azimuthal symmetry, we can write the governing equations in terms of ω'_θ and v'_θ in the following form:

$$
\begin{aligned}
&\text{N}\frac{\partial v'_\theta}{\partial t'} + \left(v'_r \frac{\partial v'_\theta}{\partial r'} + v'_z \frac{\partial v'_\theta}{\partial z'} + \frac{v'_\theta v'_r}{r'} \right) \\
&= -\frac{1}{\text{Ro}} v'_r + \frac{1}{\text{Re}} \left(\frac{\partial^2 v'_\theta}{\partial r'^2} + \frac{1}{r'} \frac{\partial v'_\theta}{\partial r} - \frac{v'_\theta}{r'^2} \right) + \frac{1}{\delta^2 \text{Re}} \frac{\partial^2 v'_\theta}{\partial z'^2},
\end{aligned}
\tag{5.3}
$$

$$
\begin{aligned}
&\text{N}\frac{\partial \omega'_\theta}{\partial t'} + \left(v'_r \frac{\partial \omega'_\theta}{\partial r'} + v'_z \frac{\partial \omega'_\theta}{\partial z'} - \frac{\omega'_\theta v'_r}{r'} - \frac{1}{\delta r'} \frac{\partial v'^2_\theta}{\partial z'} \right) \\
&= \frac{1}{\delta \text{Ro}} \frac{\partial v'_\theta}{\partial z'} + \frac{1}{\text{Re}} \left(\frac{\partial^2 \omega'_\theta}{\partial r'^2} + \frac{1}{r'} \frac{\partial \omega'_\theta}{\partial r'} - \frac{\omega'_\theta}{r'^2} \right) + \frac{1}{\delta^2 \text{Re}} \frac{\partial^2 \omega'_\theta}{\partial z'^2},
\end{aligned}
\tag{5.4}
$$

$$\frac{1}{r'} \frac{\partial}{\partial r'}(r' v'_r) + \frac{\partial v'_z}{\partial z'} = 0 \tag{5.5}$$

with the rotation number $\text{N} \equiv |2\Omega + \hat{\omega}_0|/|\hat{\omega}_0| = |1 + \text{Ro}|/|\text{Ro}|$.

   The typical time scale is taken as $|2\Omega + \hat{\omega}_0|^{-1}$, since $|2\Omega + \hat{\omega}_0|$ is the natural rotation frequency at the center of the vortex. Due to this definition of the typical time scale, the correct form of the equations is recovered when Ro $= \infty$. In this case, the three remaining nondimensional parameters are Re, δ, and R_c. In addition, by multiplying (5.3) and (5.4) by Ro and making $\hat{\omega}_0 = 0$, we recover the equations for the limit of solid body rotation.

   For convenience of notation, the primes will be omitted from here on. Furthermore, it is useful to define the new variables

$$\Phi = \omega_\theta/r, \tag{5.6}$$

and

$$V = r v_\theta + r^2/(2\text{Ro}), \tag{5.7}$$

where V is the absolute angular momentum nondimensionalized with $\hat{\omega}_0 L_0^2$. The system of governing equations can now be written as

$$\mathrm{N}\frac{\partial V}{\partial t} + \frac{1}{r}\left[V, \psi\right] = \frac{1}{\mathrm{Re}}r\frac{\partial}{\partial r}\left(\frac{1}{r}\frac{\partial V}{\partial r}\right) + \frac{1}{\delta^2\mathrm{Re}}\frac{\partial^2 V}{\partial z^2}, \tag{5.8}$$

$$\mathrm{N}\frac{\partial \Phi}{\partial t} + \frac{1}{r}\left[\Phi, \psi\right] = \frac{1}{\delta r^4}\frac{\partial V^2}{\partial z} + \frac{1}{\mathrm{Re}}\left(\frac{\partial^2 \Phi}{\partial r^2} + \frac{3}{r}\frac{\partial \Phi}{\partial r}\right) + \frac{1}{\delta^2\mathrm{Re}}\frac{\partial^2 \Phi}{\partial z^2}, \tag{5.9}$$

$$\Phi = \frac{1}{r^2}\tilde{\Delta}\psi = \frac{1}{r^2}\left(\delta\frac{\partial^2\psi}{\partial r^2} - \delta\frac{1}{r}\frac{\partial\psi}{\partial r} + \frac{1}{\delta}\frac{\partial^2\psi}{\partial z^2}\right), \tag{5.10}$$

where

$$[f, g] = \frac{\partial f}{\partial r}\frac{\partial g}{\partial z} - \frac{\partial f}{\partial z}\frac{\partial g}{\partial r}, \tag{5.11}$$

$\tilde{\Delta}$ is the dimensionless modified Laplacian operator, and ψ is the streamfunction defined by

$$v_r = \frac{1}{r}\frac{\partial\psi}{\partial z}, \quad v_z = -\frac{1}{r}\frac{\partial\psi}{\partial r}. \tag{5.12}$$

Equation (5.8) shows that for the inviscid case the angular momentum of the fluid is locally modified exclusively by the meridional flow (v_r, v_z), while (5.9) shows that the meridional flow is coupled to the swirl flow by the term $r^{-4}\delta^{-1}\partial V^2/\partial z$. The physical interpretation of this coupling term rests on the balance (to lowest order) between the radial pressure gradient and $v_\theta^2/r + v_\theta/\mathrm{Ro}$. In other words, a vertical gradient of the angular momentum implies a vertical pressure gradient that drives a meridional flow.

To study the interaction between the swirl flow and the meridional flow, we follow the approach taken by Lord Kelvin (Thomson, 1880), assuming a small perturbation V_1 of the basic vortex with absolute angular momentum V_0:

$$V = V_0 + V_1, \tag{5.13}$$

where $V_1 \ll V_0$ so that the conditions for linearization hold. In addition, the meridional flow satisfies: $\Phi = \Phi_1 \ll V_0$, $\psi = \psi_1 \ll V_0$.

Substitution of (5.13) into (5.8)–(5.10), yields to lowest order an equation for V_0:

$$\mathrm{N}\frac{\partial V_0}{\partial t} = \frac{1}{\mathrm{Re}}\left(r\frac{\partial}{\partial r}\frac{1}{r}\frac{\partial V_0}{\partial r}\right) + \frac{1}{\delta^2\mathrm{Re}}\frac{\partial^2 V_0}{\partial z^2}, \tag{5.14}$$

and hence, the basic state is only modified by diffusion. In addition, we obtain a set of equations for V_1, Φ_1, and ψ_1:

$$\mathrm{N}\frac{\partial V_1}{\partial t} + \frac{1}{r}\left[V_0, \psi_1\right] = \frac{1}{\mathrm{Re}}\left(r\frac{\partial}{\partial r}\frac{1}{r}\frac{\partial V_1}{\partial r}\right) + \frac{1}{\delta^2\mathrm{Re}}\frac{\partial^2 V_1}{\partial z^2}, \tag{5.15}$$

$$\mathrm{N}\frac{\partial \Phi_1}{\partial t} = \frac{2}{\delta r^4}\left(V_0\frac{\partial V_1}{\partial z} + V_1\frac{\partial V_0}{\partial z}\right) + \frac{1}{\mathrm{Re}}\left(\frac{\partial^2 \Phi_1}{\partial r^2} + \frac{3}{r}\frac{\partial \Phi_1}{\partial r}\right) + \frac{1}{\delta^2\mathrm{Re}}\frac{\partial^2 \Phi_1}{\partial z^2}, \quad (5.16)$$

$$\Phi_1 = \frac{1}{r^2}\tilde{\Delta}\psi_1, \tag{5.17}$$

where second order quantities have been neglected.

5.4   Inviscid linear theory

In this section, we study the inviscid limit ($\mathrm{Re} \to \infty$) of (5.14)–(5.17). If V_0 is z-independent, then $V_0 = V_0(r)$, and the combination of (5.15)–(5.17) results in the following equation for ψ_1:

$$\frac{\partial^2}{\partial t^2}\tilde{\Delta}\psi_1 = -\frac{\eta(r)}{\delta}\frac{\partial^2 \psi_1}{\partial z^2} \tag{5.18}$$

with

$$\eta(r) = \frac{1}{\mathrm{N}^2 r^3}\frac{\mathrm{d}V_0^2}{\mathrm{d}r}, \tag{5.19}$$

where η denotes the extended Rayleigh discriminant (Hopfinger & van Heijst, 1993) normalized to 1 for $r = 0$.

Assume now a time-periodic perturbation $\psi_1 = \tilde{\psi}(r,z)e^{i\xi t}$, with ξ the frequency of the oscillation. Substitution of this form into the previous equation yields

$$\xi^2\tilde{\Delta}\tilde{\psi} = \frac{\eta(r)}{\delta}\frac{\partial^2 \tilde{\psi}}{\partial z^2}. \tag{5.20}$$

Assuming a separable solution, $\tilde{\psi}(r,t) = R(r)Z(z)$, leads to equations for R and Z:

$$\frac{1}{Z}\frac{\mathrm{d}^2 Z}{\mathrm{d}z^2} = -\lambda^2, \tag{5.21}$$

$$r\frac{\mathrm{d}}{\mathrm{d}r}\left(\frac{1}{r}\frac{\mathrm{d}R}{\mathrm{d}r}\right) - \frac{\lambda^2}{\delta^2}R = -\frac{\lambda^2}{\delta^2}\left(\frac{\eta(r)}{\xi^2}\right)R, \tag{5.22}$$

where λ is the separation constant.

At the bottom ($z = 0$) and at the rigid free surface ($z = 1$), an impermeability condition is imposed ($\tilde{\psi} = 0$). Together with these boundary conditions, (5.21) constitutes an eigenvalue problem for the eigenvalue λ, and the quantized solution is of the form

$$Z(z) = C_2\sin(\lambda_n z), \tag{5.23}$$

where the vertical wave number is $\lambda_n = \pi(n+1)$, and the integer $n = 0, 1, 2, \ldots$ is the vertical mode number.

Equation (5.22) is rewritten as

$$r\frac{\mathrm{d}}{\mathrm{d}r}\left(\frac{1}{r}\frac{\mathrm{d}R}{\mathrm{d}r}\right) - k_n^2 R = -k_n^2 \frac{\eta(r)}{\xi_n^2} R, \tag{5.24}$$

where $k_n^2 = \lambda_n^2 / \delta^2$. Solutions to (5.24) are required to satisfy the following boundary conditions:

$$R(r = 0) = R(r = \mathrm{R_c} \leq \infty) = 0. \tag{5.25}$$

With these homogeneous boundary conditions, (5.24) constitutes a Hermitian eigenvalue problem of Sturm–Liouville type for the eigenvalue ξ_n provided that $\eta(r) > 0$ for $0 < r < \mathrm{R_c}$, i.e. if the vortex is stable to centrifugal instability. This implies that all eigenvalues $\xi_{m,n}$ are discrete and real-valued.

5.4.1 The role of horizontal confinement in the frequency range

The extended Rayleigh discriminant η can be rewritten as

$$\eta(r) = \frac{1}{(\mathrm{Ro}+1)^2}\left(1 + \mathrm{Ro}\frac{2v_{\theta,0}}{r}\right)(1 + \mathrm{Ro}\omega_{z,0}), \tag{5.26}$$

with $v_{\theta,0} = v_{\theta,0}(r)$ the azimuthal velocity of basic vortex, and $\omega_{z,0} = \omega_{z,0}(r) = (1/r)[\mathrm{d}(rv_{\theta,0})/\mathrm{d}r]$ the vorticity.

For vortices with $\omega_{z,0}$ monotonically decreasing in r, such as the Rankine vortex and the Lamb–Oseen vortex, $\omega_{z,0} = 1 + \mathcal{O}(r^2)$ and $v_{\theta,0} = r/2 + \mathcal{O}(r^3)$ as $r \downarrow 0$, and $\omega_{z,0} \to 0$ and $v_{\theta,0} \to 0$ for $r \to \infty$ yielding

$$\eta(r) \to \begin{cases} 1, & r \downarrow 0, \\ \dfrac{1}{(\mathrm{Ro}+1)^2}, & r \to \infty. \end{cases} \tag{5.27}$$

The upper bound for the spectrum of $\xi_{m,n}$ can be determined by multiplying (5.24) by R/r and integrating over $0 < r < \mathrm{R_c}$. Then, through integration by parts and using the boundary conditions, we obtain

$$0 \leq \xi_{m,n}^2 \leq \begin{cases} 1, & 0 \leq \mathrm{Ro} < \infty \\ (\mathrm{Ro}+1)^{-2}, & -1 < \mathrm{Ro} < 0 \end{cases} \tag{5.28}$$

where we have assumed that $\eta(r)$ monotonically decreases (increases) from $\eta(0) = 1$ to $\eta(\infty) = (\mathrm{Ro}+1)^{-2}$ for $0 \leq \mathrm{Ro} < \infty$ $(-1 < \mathrm{Ro} < 0)$. Note that for anticyclonic vortices, our study is restricted to $-1 < \mathrm{Ro} < 0$ since the vortices are prone to centrifugal instability and (5.24) is no longer an eigenvalue problem of the Sturm–Liouville type for $\mathrm{Ro} < -1$.

To clarify the meaning of the upper bounds for the frequency range, it is convenient to define the dimensional frequency $\xi^*_{m,n} = |\hat{\omega}_0 + 2\Omega|\xi_{m,n}$. Then, $\xi^2_{m,n} = 1$ is equivalent to $\xi^{*2}_{m,n} = (\hat{\omega}_0 + 2\Omega)^2$ in dimensional units, while $\xi^2_{m,n} = (\mathrm{Ro}+1)^{-2}$ is equivalent to $\xi^{*2}_{m,n} = (2\Omega)^2$ in dimensional units.

If $\mathrm{R_c} = \infty$, it is useful to write (5.24) in normal form by taking $R = \sqrt{r}F$:

$$\frac{\mathrm{d}^2 F}{\mathrm{d}r^2} + \left\{ k_n^2 \left[\frac{\eta(r)}{\xi^2_{m,n}} - 1 \right] - \frac{3}{4r^2} \right\} F = 0. \tag{5.29}$$

To satisfy the boundary condition for $r \to \infty$, the term $\eta(r)/\xi^2_{m,n}$ in (5.29) must satisfy

$$\frac{\eta(\infty)}{\xi^2_{m,n}} < 1 \tag{5.30}$$

which — using (5.27) — implies that

$$\xi^2_{m,n} > (\mathrm{Ro}+1)^{-2}. \tag{5.31}$$

Combining this with (5.28), we conclude that for $\mathrm{R_c} = \infty$:

$$(\mathrm{Ro}+1)^{-2} < \xi^2_{m,n} \le 1 \quad \text{for } 0 \le \mathrm{Ro} < \infty, \tag{5.32}$$

and no modes are possible for $-1 < \mathrm{Ro} < 0$.

Condition (5.32) implies that in an infinite domain no modes with frequencies smaller than the rotation rate of the system $[\xi^2_{m,n} < (\mathrm{Ro}+1)^{-2}]$ exist, while these frequencies are sustained within a domain bounded in the r-direction ($\mathrm{R_c} < \infty$).

For Kelvin waves in a non-confined ($\mathrm{R_c} = \infty$) Lamb–Oseen vortex with background rotation, (5.22) was studied recently by Le Dizès (2008), using a WKJB approach based on the vertical wave number being large. Le Dizès found nontrivial solutions to (5.22) that satisfy the homogeneous Dirichlet conditions $R(r) = 0$ at $r = 0$ and $r = \mathrm{R_c} = \infty$ for $(\mathrm{Ro}+1)^{-2} < \xi^2_{\mathrm{m,n}} < 1$ (that is, the absolute value of the dimensional frequency is between 2Ω and $2\Omega + \hat{\omega}_0$). However, no solutions were found for $0 < \xi^2_{m,n} < (\mathrm{Ro}+1)^{-2}$ in agreement with condition (5.32).

The physical difference between the two different boundary conditions can be explained as follows. When $R_c = \infty$, the wave must be outgoing or exponentially small at infinity; this condition is known as a radiative boundary condition. However, reflexions are also allowed at the boundary when $R_c < \infty$.

5.4.2   The Rankine vortex

To solve the eigenvalue problem (5.24) analytically, we focus on a relatively simple vortex profile, namely the Rankine vortex confined to a rotating cylinder. The structure of the Rankine vortex consists of a core of uniform vorticity and an
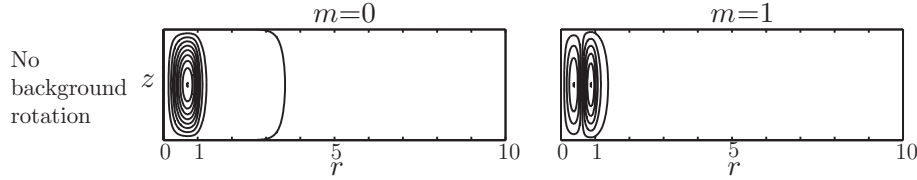
Figure 5.1 – *Streamlines of the inertial waves sustained by a Rankine vortex without background rotation. Isolines of $\tilde{\psi}$ for $\mathrm{Ro} = \infty$, $\mathrm{R_c} = 10$, $\delta = 0.5$, and mode numbers $n = 0$ and $m = 0, 1$.*

irrotational exterior, and is given, in terms of the absolute angular momentum, by

$$
V_0(r) =
\begin{cases}
\dfrac{r^2}{2} + \dfrac{r^2}{2\mathrm{Ro}}, & 0 \le r < 1 \\[2ex]
\dfrac{1}{2} + \dfrac{r^2}{2\mathrm{Ro}}, & 1 \le r \le \mathrm{R_c}.
\end{cases}
\tag{5.33}
$$

For this profile the solution to (5.24) is presented in detail in Appendix C.

An example of the streamlines in the (r, z)-plane for a Rankine vortex without background rotation is shown in figure 5.1 for $\delta = 0.5$ and modes numbers $n = 0$ and $m = 0,\ 1$. As can be seen, the secondary flow is composed of recirculation cells, where $n+1$ gives the number of cells in the vertical direction, and $m+1$ gives the number of cells in the radial direction. For $\mathrm{Ro} = \infty$, $\tilde{\psi}$ outside the vortex core $(r > 1)$ is given in terms of evanescent, modified Bessel functions; the meridional flow is irrotational $(\Phi = 0)$; and $V_1 = 0$ as found by Lord Kelvin (Thomson, 1880).

Cyclonic vortices

For cyclonic vortices $(0 < \mathrm{Ro} < \infty)$, the maximum frequency allowed is such that $\xi_{m,n}^2 = 1$, as shown in (5.28). Thus, the streamfunction $\tilde{\psi}$ inside the vortex core $(r < 1)$ is given in terms of J_1, the Bessel function of the first kind and order one [see (C.5)].

On the other hand, outside the vortex core $(r > 1)$ there are three qualitatively different regimes that depend on the value of the frequency $\xi_{m,n}$:

- **Regime CI**: $1 > \xi_{m,n}^2 > (\mathrm{Ro} + 1)^{-2}$ and $\xi_{m,n}^2 > k_n^2/(\mathrm{N^2Ro})$. In this regime, the streamfunction in the outer region is given in terms of modified Bessel functions of order $\gamma \in \mathbb{R}$ [see (C.8)]. Hence, the streamfunction has an exponentially decaying tail outside the vortex core as for $\mathrm{Ro} = \infty$. See, for example, the upper panels in figure 5.2

- **Regime CII**: $1 > \xi_{m,n}^2 > (\mathrm{Ro} + 1)^{-2}$ and $\xi_{m,n}^2 < k_n^2/(\mathrm{N^2Ro})$. In this regime, the streamfunction $\tilde{\psi}$ in the outer region is given in terms of modified Bessel functions of imaginary order $(\gamma \in \mathbb{I})$. In this case, the streamfunction can have an oscillatory behavior in r outside the vortex core, but still an
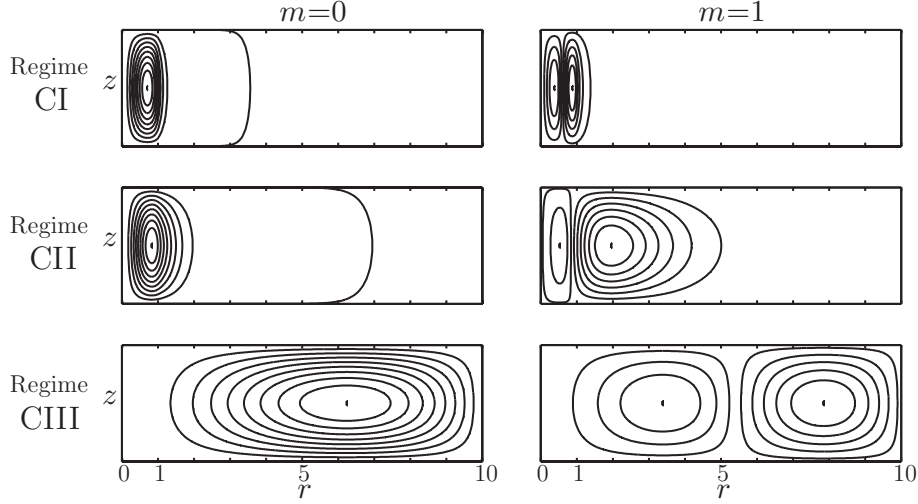
Figure 5.2 – *Three regimes for the streamlines of the inertial modes sustained by a Rankine vortex with background rotation. Isolines of $\tilde{\psi}$ for $R_c = 10$, $\delta = 0.5$, and mode numbers $n = 0$ and $m = 0, 1$ for different values of* Ro. **Regime CI** *(top):* Ro $= 100$, $(\mathrm{Ro}+1)^{-1} \approx 0.01$, and $k_n^2/(\mathrm{N}^2\mathrm{Ro}) \approx 0.39$, while $\xi_{0,0} \approx 0.71$ and $\xi_{0,1} \approx 0.55$. **Regime CII** *(middle):* Ro $= 0.25$, $(\mathrm{Ro}+1)^{-1} = 0.8$ and $k_n^2/(\mathrm{N}^2\mathrm{Ro}) \approx 6.32$, while $\xi_{0,0} \approx 0.87$ and $\xi_{0,1} \approx 0.81$. **Regime CIII** *(bottom):* Ro $= 0.02$, $(\mathrm{Ro}+1)^{-1} \approx 0.980$ and $k_n^2/(\mathrm{N}^2\mathrm{Ro}) \approx 0.759$, while $\xi_{0,0} \approx 0.979$ and $\xi_{0,1} \approx 0.975$.

exponentially decaying tail exists next to the outer wall. See, for example, the middle panels in figure 5.2.

- **Regime CIII**: $(\mathrm{Ro}+1)^{-2} > \xi_{m,n}^2 > 0$. In this case, the streamfunction $\tilde{\psi}$ is given in terms of Bessel functions [see (C.17)], which have an oscillatory behavior in r that extends radially across the whole cylinder, as shown in the bottom panels of figure 5.2. In this regime, $\tilde{\psi}$ is similar to the streamfunction obtained for inertial oscillations inside a rotating cylinder without a vortex in the center (see Fultz, 1959). Note that this regime does not exist in the case $R_c = \infty$. In fact, we show in Appendix C that, in this regime, the solution to (5.24) for a Rankine vortex cannot satisfy the boundary condition $\psi \to 0$ as $r \to \infty$.

As has been seen in figures 5.1 and 5.2, the secondary flow is composed of recirculation cells. These cells redistribute the angular momentum V, changing its vertical distribution. Subsequently, the recirculation cells reverse their direction due to the change in the vertical gradient of V, and this interaction repeats itself.

In fact, the evolution of the absolute angular momentum of the swirl flow, following (5.15), is given by

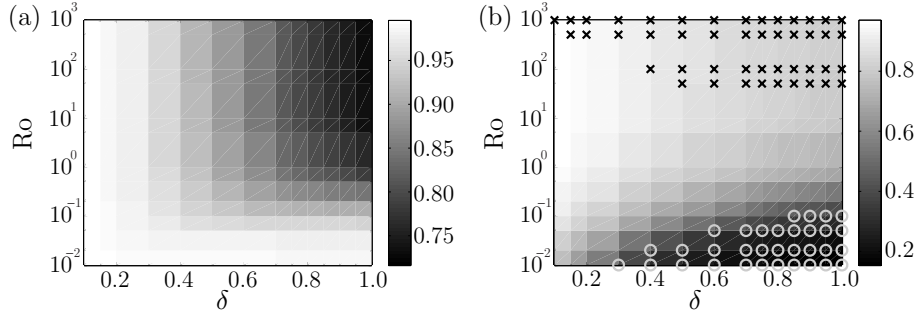$$V(r, z, t) = V_0(r) + \tilde{V}_1(r) \cos(\lambda_n z) e^{i(\xi_{m,n} t + \pi/2)}, \tag{5.34}$$

Figure 5.3 – *Graphical representation of the frequency and the wavenumber of mode $(m,n) = (0,0)$ as a function of Ro and δ. The grayscale denotes (a) the absolute value of the frequency $|\xi_{0,0}|$ and (b) the normalized wave umber $\bar{\alpha}_{0,0}$ for $R_c = 10$ as a function of Ro and δ. The crosses in (b) mark solutions corresponding to regime CI, while the circles mark solution corresponding with regime CIII.*

where

$$\tilde{V}_1(r) = \epsilon \frac{\lambda_n}{\xi_{m,n}} \begin{cases} R(r), & 0 \leq r < 1 \\ \dfrac{1}{\mathrm{Ro}+1} R(r), & 1 \leq r \leq R_c \end{cases} \tag{5.35}$$

with $\epsilon \ll \xi_{m,n}/\lambda_n$, and $R(r)$ is the r-dependence of the streamfunction $\tilde{\psi}$. Note that the frequency of the oscillation in V is equal to the frequency of the oscillations in the secondary motion but out of phase by a quarter period.

Furthermore, $\tilde{V}_1$ has a discontinuity at $r = 1$ for Ro $\neq 0$. This discontinuity is consistent with the fact that $\tilde{V}_1 = 0$ outside the vortex core for Ro $= \infty$ (Thomson, 1880), whereas for Ro $= 0$, the discontinuity disappears, and the solution for a rotating cylinder without a vortex is retrieved (see Fultz, 1959). Independently of the frequency $\xi_{m,n}$, if Ro $\neq 0$, then $V_1 \neq 0$ outside the vortex core, and the oscillations of the azimuthal motion are no longer confined to the inside of the vortex core. However, the amplitude of V_1 outside the vortex core can be negligible for large Ro-values.

We have shown that the recirculation cells can differ qualitatively depending on the value of the frequency $\xi_{m,n}$. Furthermore, the values of $\xi_{m,n}$ depend on the problem parameters: Ro, δ and R_c. Figure 5.3(a) shows the absolute value of the frequency for mode $(m,n) = (0,0)$, $|\xi_{0,0}|$, for $R_c = 10$ as a function Ro and δ. As can be seen, the frequency of the zeroth mode tends to unity as $\delta \to 0$ and Ro $\to 0$, while the lowest frequencies are reached for slow rotation (large Ro-values) and large aspect ratio δ, when keeping R_c fixed.

Figure 5.3(b) shows the normalized wave number inside the vortex core $\bar{\alpha}_{0,0} = \alpha_{0,0}/j_{1,0}$ [with $j_{1,0}$ the first zero of J_1 and $\alpha_{0,0}$ the wave number inside the vortex core as define in (C.4)] for $R_c = 10$ as a function Ro and δ. As can be seen, the wave number is smaller for fast rotation rates (small Ro-values) and large aspect ratio δ. It is in this region of the parameter space that the zeroth mode occupies
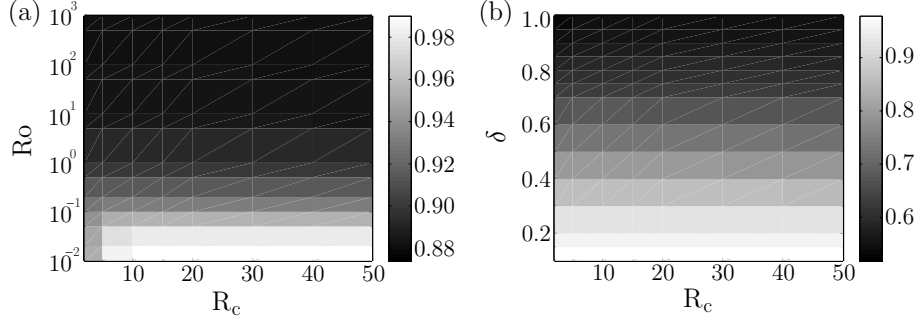
Figure 5.4 – *Graphical representation of the frequency of mode $(m,n) = (0,0)$ for a Rankine vortex as a function of Ro, δ, and R_c. (a) Grayscale denotes values of the frequency $\xi_{0,0}$ for for fixed $\delta = 1$ as a function of Ro and R_c. (b) Values of the frequency $\xi_{0,0}$ for for fixed Ro $= 1$ as a function of δ and R_c.*

the whole cylinder, as shown by the circles that denote regime CIII. Furthermore, the wave number is larger for slow rotation rates (large Ro) and small aspect ratio. It is in this region when the recirculation cell is smaller in the radial direction. Surprisingly, this behavior does not correspond to the regime CI denoted by the crosses. However, it is clear that a smaller aspect ratio δ tends to reduce the radial extent of the oscillations, while strong rotation tends to increase it.

As the mode number m increases, the frequency $\xi_{m,n}$ decreases for fixed mode number n. Hence, the boundary between the different regimes depends on the mode number. In other words, even if, for example, mode $(m,n) = (0,0)$ corresponds to regime CII there can be a mode (m,n) with $m > 0$ in regime CIII for the same values of the problem parameters.

After pointing out the difference between an infinite and a finite domain in the frequency range in Section 5.4.1, we have restricted our study to the case of $R_c = 10$. In figure 5.4(a), we present the value of the frequency $\xi_{0,0}$ for fixed $\delta = 1$ as a function of Ro and R_c, while in figure 5.4(b), we present the value of $\xi_{0,0}$ for fixed Ro $= 1$ as a function of δ and R_c. As can be clearly seen, the frequency does not depend strongly on R_c for large values of this parameter.

Anticyclonic vortices

It was shown in (5.28) that for anticyclones $(-1 < \text{Ro} < 0)$ the frequency is such that $\xi_{m,n}^2 < (\text{Ro} + 1)^{-2}$. Hence, outside the vortex core, the solution to (5.24) is given in terms of Bessel functions [see (C.17)] and the recirculation cells extend to the outer wall.

On the other hand, there are two qualitatively different regimes inside the vortex core:

- **Regime AI**: $(\text{Ro} + 1)^{-2} > \xi_{m,n}^2 > 1$. In this regime, the solution to (5.24) inside the vortex core is given in terms of $I_1(\alpha r)$, the modified Bessel function of the first kind and order one [see (C.5)]. Hence, the streamfunction $\tilde{\psi}$ cannot
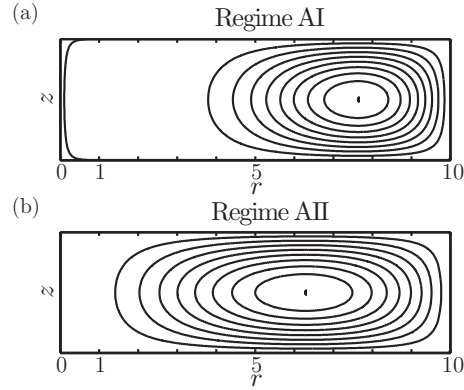
Figure 5.5 – *(a) Isolines of $\tilde{\psi}$ for* Ro $= -0.5$, R$_c$ $= 10$, $\delta = 0.5$, *and* $(m, n) = (0, 0)$. *In this case* $\xi_{0,0} \approx 1.983 > 1$ *corresponding to regime AI. (b) Isolines of $\tilde{\psi}$ for* Ro $= -0.001$, R$_c$ $= 10$, $\delta = 0.5$, *and* $(m, n) = (0, 0)$. *In this case* $\xi_{0,0} \approx 0.991 < 1$ *corresponding to regime AII.*

have an oscillatory behavior in r inside the vortex core. An example of such a flow is presented in figure 5.5(a), where the streamlines of the secondary flow for $(m, n) = (0, 0)$, Ro $= -0.5$, $\delta = 0.5$, and R$_c$ $= 10$ are plotted.

- **Regime AII**: $1 > \xi_{m,n}^2 > 0$. In this regime, the solution to (5.24) inside the vortex core is given in terms of $J_1(\alpha r)$, the Bessel function of the first kind and order one [see (C.5)]. Hence, the recirculation can have an oscillatory behavior in r across the whole cylinder. This can be seen in figure 5.5(b), where the streamlines for $(m, n) = (0, 0)$, Ro $= -0.01$, $\delta = 0.5$, and R$_c$ $= 10$ are plotted.

5.4.3 The Lamb-Oseen vortex

The Rankine vortex is a crude approximation for a real vortex, and it is by nature an inviscid model. To later consider the effects of viscosity, we study the waves sustained by the Lamb-Oseen vortex which is a good approximation to some real vortices (see e.g. Hopfinger & van Heijst, 1993). In this section, we consider a time-independent Lamb-Oseen vortex with a velocity profile given by

$$v_{\theta,0}(r) = \frac{1}{2r} \left[1 - \exp(-r^2) \right].$$
(5.36)

This vortex is characterized by a strong stability. For example, although it can be unstable with respect to centrifugal instability, this is only the case for strong anticyclonic vortices with Ro < -1 (Hopfinger & van Heijst, 1993) as for the Rankine vortex. Furthermore, it is stable to shear instability (Saffman, 1992), and as long as there is no elliptical perturbation also to elliptical instability. This stability backs our assumption of azimuthal symmetry.

The absolute angular momentum for the Lamb-Oseen vortex is given by

$$V_0(r) = \frac{1}{2}[1 - \exp(-r^2)] + \frac{r^2}{2\mathrm{Ro}}. \tag{5.37}$$

For this profile, (5.24) cannot be solved analytically; hence, the eigenvalue problem is solved numerically with the finite element code COMSOL — using the one-dimensional general form PDE module with the UMFPACK solver and 120 elements (see COMSOL AB, 2008).

The dynamics of the axisymmetric inertial oscillations sustained by a Rankine vortex are similar for a Lamb-Oseen vortex in the non-rotating case Fabre et al. (2006), as in the case with background rotation. However, some differences in the characteristics of such oscillations exist.

Figure 5.6(a) presents the ratio of $\xi_{0,0}$ for Lamb–Oseen vortex to $\xi_{0,0}$ for a Rankine vortex as a function of Ro and δ for $R_c = 10$. As can be seen, this ratio tends to unity as the rotation rate increases; already for Ro < 1, the frequency ratio does not exceed 10%. For large Ro-values and large δ-values — in regime CI — the difference in frequencies is most important. In contrast, specially in regime CIII, the frequency ratio is close to unity. This can be easily explained, since for small Ro-values the vortex motion is very weak compared to the background rotation.

Figure 5.6(b) shows the ratio of $\alpha_{0,0}$ for a Lamb–Oseen vortex to $\alpha_{0,0}$ for a Rankine vortex. As can be seen, for small Ro-values this ratio tends to unity suggesting that the radial wave number does not depend on the velocity profile. However, when rotation is decreased, the wave number $\alpha_{0,0}$ for the Lamb–Oseen vortex becomes up to three times larger than the wave number for the Rankine vortex for small aspect ratio δ. This can be explained as follows. For the Rankine vortex, waves with frequencies close to unity can be sustained inside the whole vortex core since the frequency is smaller than $2\Omega + \hat{\omega}$ for $0 < r < 1$ with $\hat{\omega}$ the peak vorticity. However, for the Lamb–Oseen vortex, the waves with frequencies approaching unity can only be sustained in a smaller domain.

In figure 5.6(b) the crosses denote the parameter for which mode $(m, n) = (0, 0)$ is in regime CI, while the circles denote the parameters for which mode $(m, n) = (0, 0)$ is in regime CIII. As can be seen by comparison with figure 5.3(b), the boundary between the different regimes agrees well for both vortex profiles. Furthermore, the characteristics of the three different regimes for cyclonic Rankine vortices are similar for a Lamb–Oseen vortex.

5.5   The effects of viscosity

5.5.1   In a cylinder with stress-free boundaries

When considering a time-independent Lamb–Oseen vortex, as in the previous section, the effect of viscosity on axisymmetric inertial oscillations is rather trivial.
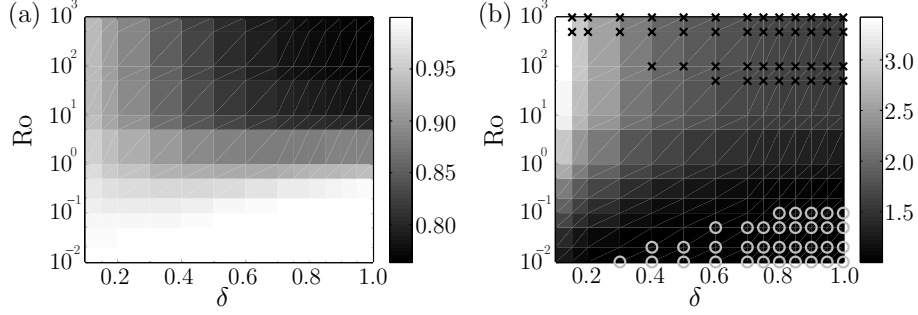
Figure 5.6 – *Graphical representation of the characteristics of mode $(m,n) = (0,0)$ for the Lamb–Oseen vortex compared to the characteristics of mode $(m,n) = (0,0)$ for the Rankine vortex. The grayscale denotes (a) the ratio of $|\xi_{0,0}|$ for the Lamb–Oseen vortex and $|\xi_{0,0}|$ for the Rankine vortex and (b) the ratio of $\bar{\alpha}_{0,0}$ for the Lamb–Oseen vortex and for $\bar{\alpha}_{0,0}$ for the Rankine vortex for $\mathrm{R_c} = 10$ as a function of Ro and δ. The crosses in (b) mark the points that correspond to regime CI, while the circles mark the point that correspond to regime CI.*

As found by Fabre et al. (2006) for the case of no background rotation, viscosity only damps the oscillations.

Horizontal diffusion can be neglected in the case that $\alpha_m \ll k_n$, and vertical diffusion does not modify the basic swirl flow if V_0 does not depend on z. However, diffusion affects the evolution of the perturbation. This can be expressed by including the vertical viscous terms in (5.18) for ψ_1:

$$\frac{\partial^2 \tilde{\Delta}\psi_1}{\partial t^2} = -\frac{1}{\delta r^3 \mathrm{N}^2}\frac{\partial V_0^2}{\partial r}\frac{\partial^2 \psi_1}{\partial z^2} + \frac{2}{\mathrm{ReN}\delta^2}\frac{\partial^2}{\partial z^2}\frac{\partial \tilde{\Delta}\psi_1}{\partial t} - \frac{1}{\mathrm{N}\,\mathrm{Re}^2\delta^4}\frac{\partial^4 \tilde{\Delta}\psi_1}{\partial z^4}. \quad (5.38)$$

Stress-free boundary conditions are imposed at $z = 0$ and $z = 1$, and we assume a harmonic dependence both in time and in z: $\psi_1 = R(r)\sin(\lambda_n z)e^{i\phi t}$. Substitution of this solution into (5.38) yields

$$\left(\phi - i\frac{k_n^2}{\mathrm{N}\,\mathrm{Re}}\right)^2 \tilde{\Delta}\psi_1 = -\frac{1}{\delta r^3 \mathrm{N}^2}\frac{\partial V_0^2}{\partial r}\frac{\partial^2 \psi_1}{\partial z^2}, \quad (5.39)$$

which can be transformed into (5.20) for the inviscid case by taking $\xi = \phi - ik_n^2/\mathrm{NRe}$, where ξ is again the frequency for the inviscid case. Therefore, the frequency for the viscous case is

$$\phi = \xi + i\frac{k_n^2}{\mathrm{N}\,\mathrm{Re}}, \quad (5.40)$$

where the imaginary part is a damping coefficient, which in dimensional units can be written as $\nu\lambda_n^2/H^2$. This damping rate is the slowest damping rate possible, since if radial diffusion is included, the damping rate would be higher and the radial shape of the recirculation cells would be modified.

However, viscosity also affects the main azimuthal motion. For the Lamb–Oseen vortex, the time-dependent azimuthal-velocity profile is given by the self-similar solution to (5.14):

$$v_{\theta,0}(r,t) = \frac{1}{2r}\left[1 - \exp\left(-\frac{r^2}{1 + 4t/\mathrm{N\,Re}}\right)\right],\tag{5.41}$$

when taking (5.37) as the initial condition. The corresponding vertical vorticity component is given by

$$\omega_{z,0}(r,t) = \frac{1}{1 + 4t/(\mathrm{N\,Re})}\exp\left(-\frac{r^2}{1 + 4t/(\mathrm{N\,Re})}\right).\tag{5.42}$$

As can be seen from (5.41) and (5.42), both the radius and the peak vorticity of the vortex change over time. Hence, it is possible to define a time-dependent Rossby number:

$$\mathrm{Ro}_T(t) = \frac{\mathrm{Ro}}{1 + 4t/(\mathrm{N\,Re})},\tag{5.43}$$

and a time dependent aspect ratio:

$$\delta_T(t) = \frac{\delta}{\sqrt{1 + 4t/(\mathrm{N\,Re})}},\tag{5.44}$$

both decreasing in time. Combining (5.43) and (5.44) yields

$$\delta_T = K\sqrt{\mathrm{Ro_T}},\tag{5.45}$$

where K is constant.

As it was seen in section 5.4.2, if both Ro and δ decrease, then the frequency tends to the maximum frequency allowed, which is now given by

$$\xi_{\max}(t) = \frac{1 + \mathrm{Ro}_T(t)}{1 + \mathrm{Ro}}\tag{5.46}$$

for the time-dependent Lamb-Oseen vortex.

To understand how the wave number changes in time, we consider that $\xi \gg 4/(\mathrm{N\,Re})$. In this case, we can assume that the vortex is frozen at every instant since the time scales for the oscillations and for the vortex decay can be separated. We also assume that $\mathrm{R_c}$ remains large as to not affect the value of the frequency and the wave number.

Figure 5.7 shows the absolute value of the wave number $|\alpha_{0,0}|$ for a Lamb–Oseen vortex as a function of Ro and δ for $\mathrm{R_c} = 20$. In addition, this figure also shows curves given by (5.45) for different values of K. The evolution of the Lamb–Oseen vortex follows these curves from right to left. As can be seen, for large Ro-values, the wave number $|\alpha_{0,0}|$ increases in time. However, when the initial values for Ro and δ are close to the boundary between the regimes CII and CIII, then the wave number remains almost constant. Hence, there is a value for K for which (5.45) gives a boundary between the two regimes.
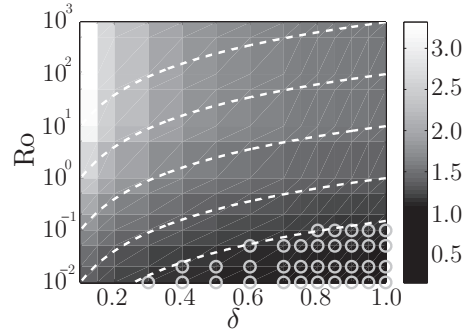
Figure 5.7 – *Evolution of the frequency of mode* $(m, n) = (0, 0)$ *sustained by a time-dependent Lamb–Oseen vortex. The grayscale denotes the normalized wave number* $\bar{\alpha}_{0,0}$ *for the oscillations sustained by a Lamb–Oseen vortex with* $R_c = 20$ *as a function of* Ro *and* δ. *The circles mark the points where* $|\xi_{0,0}| < (\text{Ro} + 1)^{-1}$, *while the dashed lines are given by* (5.45) *for different values of* K.

5.5.2 The effects of a no-slip bottom

We performed numerical simulations where (5.3)–(5.5) were solved inside a cylinder with a no-slip bottom. The initial condition was taken to be a Lamb–Oseen vortex with no vertical dependence and no perturbation, as given by (5.37). Although this initial condition does not satisfy the no-slip boundary condition at the bottom, the initial flow is adjusted instantaneously by the numerical code to satisfy the boundary condition. Several simulations were performed with different initial z-dependence to test if these profiles affected the results. We found that there were no significant differences when a small boundary layer was added to the initial vertical profile.

The simulations were performed using the finite element code COMSOL with the 2D-axisymmetric incompressible Navier–Stokes module, approximately 140 000 degrees of freedom, and the PARDISO solver (see COMSOL AB, 2008). Both the time and spatial resolution were evaluated by performing several numerical simulations with different resolutions and verifying that the results converged to the same solution.

No background rotation

First, we analyze a vortex without background rotation. In this case, when δ and Re are small, the main flow has a Poiseuille-like vertical profile and is damped at a rate $\pi^2/(4\text{Re}\,\delta^2\,\text{N})$ since the evolution is dominated by bottom friction as it was discussed in Chapters 3 and 4 . For these values of δ and Re, an analytical solution for the evolution of the secondary motion can be obtained where no inertial oscillations are sustained inside the vortex (Duran-Matute et al., 2010).

However, for larger values of δ and Re the vertical profile of the main flow differs from Poiseuille-like. Figure 5.8 shows the vertical profile of the azimuthal
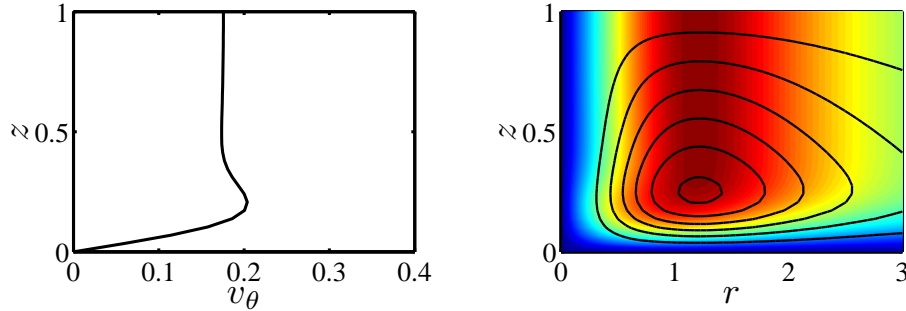
Figure 5.8 – *Lamb–Oseen vortex inside a cylinder with a no-slip bottom and no background rotation. Vertical profile of v_θ at $r = 5$ (left), contours of the secondary flow and azimuthal velocity (color) (right) at $t = 5$ for a simulation with Re = 2500, $\delta = 0.5$, Ro = ∞, and $R_c = 12$.*

velocity v_θ and streamlines in the (r, z)-plane at $t = 5$ for a simulation with Re = 2500, $\delta = 0.5$, Ro = ∞, and $R_c = 12$. From the vertical profile of v_θ, we can see that a boundary layer forms close to the bottom, and that on top of it, the flow is more uniform in the vertical. The streamlines in the (r, z)-plane show a large secondary motion that occupies the whole depth of the fluid. Unlike the recirculation cells associated with the inertial oscillations shown in previous sections, the recirculation cell shown in figure 5.8 is driven by the boundary layer.

Figure 5.9 presents snapshots of the azimuthal velocity and the streamlines in the (r, z)-plane at three different times, and of the vertical profile of the pressure $P(z)$ in the vortex core ($r = 0.01$) at three different times for a simulation with Ro = ∞, Re = 2500, $\delta = 0.5$, and $R_c = 12$. As can be seen, the vertical pressure gradient changes sign in time. This is due to the presence of inertial oscillations which are superimposed to the secondary motion. The physical process driving these oscillations, as observed in figure 5.9, can be described as follows. Initially on the vortex axis, a negative vertical pressure gradient exists, which drives an upward motion in the vortex core, and hence, a meridional flow. This flow redistributes the azimuthal velocity. Consequently, the vertical gradient of the azimuthal velocity and the pressure are inverted. This new pressure gradient forces a downward motion in the center of the vortex and the appearance of a cell in the meridional flow with an opposite direction to the main secondary flow driven by the boundary layer. This process repeats itself, always with the oscillation in the pressure out of phase by a quarter period with respect to the oscillation in the meridional flow. It can also be seen in the pressure profiles that at the top of the boundary layer ($z \approx 0.1$) the pressure gradient is always negative, thus continuously driving the large recirculation cell.

The presence of a no-slip boundary condition at the bottom has two main effects on the primary motion: (i) the main flow is damped faster due to bottom friction; (ii) the main flow is modified by the secondary flow driven by the boundary layer. However, since advection plays an important role for large values of Re and

Figure 5.9 – *Evolution of a Lamb-Oseen vortex inside a cylinder with a no-slip bottom and no background rotation. Upper row: meridional circulation at three different times (t = 5, 10, 17.5) for Ro = ∞, Re = 2500, and δ = 0.5. The color coding denotes the azimuthal velocity and the black lines are streamlines of the secondary flow in the (r, z)-plane. Lower row: pressure profile at r = 0.01 and three different times (t = 1, 7.5, 15) for the same simulations.*
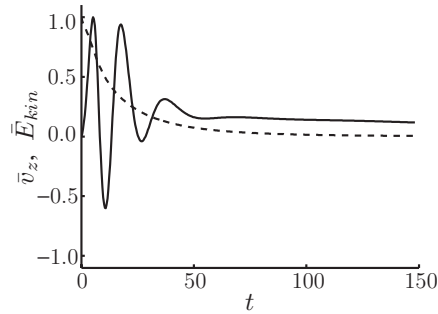
Figure 5.10 – *Evolution of the normalized vertical velocity $\bar{v}_z = v_z/\max(v_z)$ in the core of the vortex $(r, z) = (0.01, 0.8)$ (solid line), and evolution of the normalized kinetic energy of the azimuthal motion $\bar{E}_{kin} = E_{kin}/\max(E_{kin})$ (dashed line) for a simulation with Re = 2500, $\delta = 0.5$, Ro = ∞, and $R_c = 12$.*

δ, there is no analytical expression for the damping rate of the vortex or for its deformation.

Figure 5.10 shows the evolution of the normalized vertical velocity $v_z/\max(v_z)$ in the core of the vortex at $(r, z) = (0.01, 0.8)$ and the evolution of the kinetic energy of the main azimuthal flow for a simulation with Re = 2500, $\delta = 0.5$ and Ro = ∞. As can be seen, the vertical velocity inside the vortex oscillates. These oscillations are damped, and their frequency decreases in time due to the damping of the vortex and the growth of the vortex radius. By comparison with the decay of the kinetic energy of the vortex, it can be seen that the characteristic decay time of the main flow is a good estimate for the lifetime of the oscillations.

The type of flow discussed in this section and shown in figure 5.8 is similar to the one described by Akkermans et al. (2008b), who studied an electromagnetically generated dipolar vortex in a shallow layer. In that case Re $\approx$ 3500, and $201 \leq$ Re$\delta^2 \leq 727$. In such a flow, a boundary layer at the bottom and inertial oscillations in the vortex cores on top of the boundary layer were observed.

Strong background rotation

For the case of strong rotation, the main flow consists of an Ekman boundary layer at the bottom, and a geostrophic interior. This can be seen in figure 5.11, where snapshots of the azimuthal velocity and the streamfunction in the (r, z)-plane at three different times are shown for a simulation with Ro = 1, Re = 2500, $\delta = 0.5$, and $R_c = 12$.

As for the case of no background rotation, if bottom friction dominates, no inertial oscillations are sustained by the flow. For strong background rotation (Ro $\ll$ 1), this occurs when the nondimensional thickness of the Ekman boundary

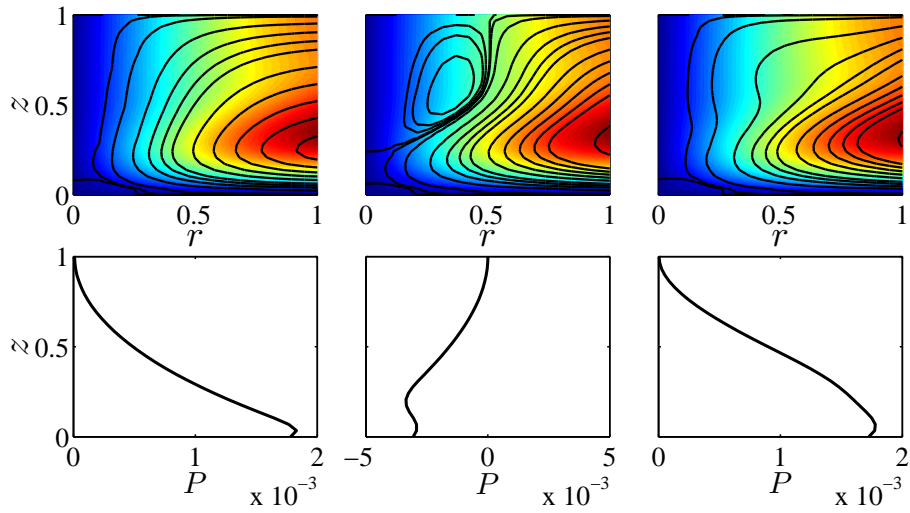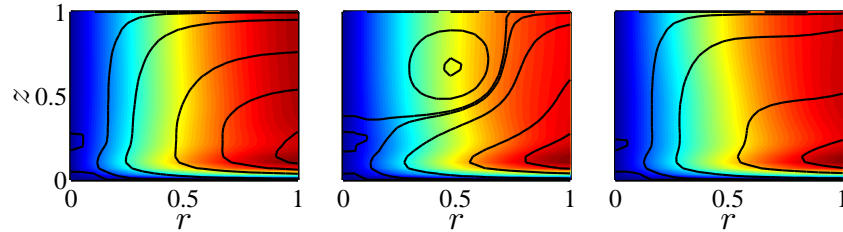**Figure 5.11** – *Evolution of a Lamb–Oseen vortex inside a cylinder with a no-slip bottom and background rotation. Upper row: meridional flow at three different times ($t = 12.5, 17.5, 20$) for Ro $= 1$, Re $= 2500$, $\delta = 0.5$, and $R_\mathrm{c} = 12$. The color coding denotes the azimuthal velocity and the black lines are streamlines of the secondary flow in the (r, z)-plane.*

layer

$$h_\mathrm{Ek} \equiv \mathrm{Ek}^{1/2} = \frac{1}{\delta} \left(\frac{2\mathrm{Ro}}{\mathrm{Re}} \right)^{1/2} \gtrsim 0.6 \tag{5.47}$$

(see Chapter 4). Hence, we focus on flows with $h_\mathrm{Ek} \ll 1$.

In figure 5.11, it can be observed, by comparison with figure 5.9, that the flow and the physical process driving the inertial oscillations is similar for flows with and without background rotation. However, in the rotating case (Ro $= 1$), the recirculation cell associated with the inertial oscillations extends farther towards the exterior of the vortex, suggesting that the radial wavelength of the oscillations is larger.

Figure 5.12 displays the evolution of the normalized vertical velocity $v_z/\max(v_z)$ in the core of the vortex at $(r, z) = (0.01, 0.8)$ and the kinetic energy of the azimuthal flow as a function of time for a simulation with Ro $= 1$, Re $= 2500$, $\delta = 0.5$, and $R_\mathrm{c} = 12$. As can be seen, the vertical velocity in the vortex core oscillates. Initially, the signal seems to be modulated, but this is due to the superposition of different modes with similar frequencies. In addition for Ro $= 1$, the oscillation is persistent throughout the simulation for a much longer time than in the case Ro $= \infty$ (figure 5.10). As seen previously, for Ro $= \infty$, no oscillations can be sustained once the vortex is damped. On the other hand, for Ro $= 1$, the system still sustains oscillations even after the vortex as been damped. In this case, the decay rate of the oscillations is closer to the damping rate given by (5.40).

It could be argued that the inertial oscillations in the simulations discussed in this section arise because the flow must adjust itself since the initial condition has no vertical dependence. To exclude this possibility, we performed also simulations where the flow was forced for some time. For these simulations, $\boldsymbol{v} = 0$ at $t = 0$, and a forcing term

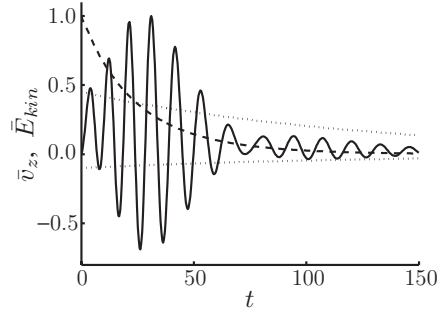$$F = \frac{F_0}{2} [1 - \exp(-r^2)], \tag{5.48}$$

Figure 5.12 – *Normalized vertical velocity $\bar{v}_z = v_z/\max(v_z)$ in the vortex core $(r, z) = (0.01, 0.8)$ (solid lines), normalized kinetic energy of the main azimuthal motion $\bar{E}_{kin} = E_{kin}/\max(E_{kin})$ (dashed line) for a simulation* Ro = 1, Re = 2500, $\delta = 0.5$, and R$_c$ = 12. *The dotted lines represent the envelope curves with a decay rate as given by (5.40).*

where F_0 is the magnitude of the forcing, was included on the right hand side of (5.8) for $0 < t < T_F$, where T_F is the forcing time. Inertial oscillations were also observed in these simulations, except when $T_F \gg 1$. Hence, we conclude that the inertial oscillations observed in previous numerical simulations are indeed a physical phenomenon.

The simulations discussed here were all performed under the assumption of axisymmetric flow, hence restricting the emergence of other modes, and other three-dimensional (3D) phenomena. To study this restriction, 3D simulations were performed for a few points in the parameter space. These simulations are computationally more expensive, thus it was not possible to achieve the same resolution as in the axisymmetric simulations. No qualitative differences were observed between the two types of simulations, however only some small quantitative differences, most likely caused by the lower spatial and temporal resolution of the 3D simulations, were found.

5.6 Conclusions

We have studied the evolution of axisymmetric inertial oscillations in a confined monopolar vortex with background rotation, and their effects on the evolution of the vortex itself. Firstly, we presented an analytical result for the inviscid inertial oscillations sustained by the Rankine vortex inside a rotating cylinder. Later, numerical results for the inviscid waves sustained by a Lamb–Oseen vortex were analyzed. Finally, we studied the effects of viscosity and of a no-slip bottom on the evolution of the oscillations. In this way, a situation similar to the one found in laboratory experiments was reached, while discussing different properties of the oscillations at every step.

From the linear inviscid theory, we showed that the frequency range of the

inertial oscillations in cyclonic vortices is such that $0 < \xi_{m,n}^{*2} < (2\Omega + \hat{\omega})^2$ (in dimensional units) where Ω is the rotation rate of the system and $\hat{\omega}$ is the peak vorticity of the vortex. However, horizontal confinement is necessary for modes with the absolute value of their frequency $|\xi_{m,n}^*| < 2\Omega$.

In the case with background rotation, the oscillations in the azimuthal flow can extend outside the vortex, as opposed to the case without background rotation. Furthermore, we found three qualitatively different regimes for the modes sustained by cyclonic vortices. It is in the regime where $\xi_{m,n}^{*2} < (2\Omega)^2$, which only exists for horizontally confined vortices, that the streamfunction in the (r, z)-plane has an oscillatory behavior in r across the whole cylinder. This behavior is characteristic for strong rotation and large aspect ratio.

The effects of viscosity are twofold. On one hand, it acts directly on the oscillations by damping them. On the other hand, it acts on the main vortex by damping it and changing its radius. In this way, the characteristics of the waves sustained by the vortex change. For the cases when stress-free boundaries are considered, the basic vortex is a Lamb–Oseen vortex, and the decay rate of the vortex is much slower than the frequency of the oscillations, then the inviscid theory can be used to obtained the results at any given time.

On the other hand, when a no-slip bottom is considered, there is a boundary layer at the bottom which drives a meridional flow, and bottom friction damps the vortex. The meridional flow affects the evolution of the basic vortex, for which there is no analytical expression. In this case, the inertial oscillations are superimposed to the main meridional flow driven by the boundary layer. For the case of no background rotation, the oscillations cannot persist as the vortex is damped and their life time is hence dictated by the lifetime of the vortex. However, when background rotation is present the waves persists even if the vortex is damped since the system can still sustain oscillations.

This study was restricted to axisymmetric dynamics. In this case, confinement plays a crucial role in the frequency range of the oscillations sustained by a vortex subjected to background rotation. It is to be expected that confinement will also play an important role in non-axisymmetric dynamics, and possibly in the stability of some vortices. This role is still to be determined.

Chapter 6

Decaying dipolar vortex[i]

6.1 Introduction

One of the characteristics of Q2D flows is the formation of large coherent structures. This phenomenon has been observed in a shallow layer of fluid by, for example, Sous et al. (2004, 2005). In their studies, an impulsive turbulent jet was introduced into a fluid initially at rest. For small fluid depths, it was observed that the vertical motions are damped and that the turbulent jet evolves into a large coherent dipolar vortex.

However, several recent studies have demonstrated that shallow dipolar vortices present a complicated 3D structure with vertical velocities that do not scale linearly with the aspect ratio. For instance, Lin et al. (2003) studied the 3D structure of vortex dipoles generated by a piston-nozzle arrangement and observed a secondary vortex, which is orthogonal and just ahead of the primary dipole. Sous et al. (2004, 2005) also observed the presence of a spanwise vortex at the front of the dipolar vortex for certain regions of their parameter space. Akkermans et al. (2008a,b) investigated numerically and experimentally the evolution of electromagnetically forced vortex dipoles. Besides observing a spanwise vortex in front of the vortex dipole, they also measured large non-negligible vertical velocities in the vortex cores, which impairs the two-dimensionality of the flow.

The importance of vertical flows — and by continuity, radial flows — for the evolution of shallow axisymmetric monopolar vortices has been previously studied using numerical simulations. These previous studies have shown that indeed the small aspect ratio promotes a decrease in the magnitude of vertical motions inside the monopolar vortices. In addition, it was shown that this magnitude depends also on the Reynolds number (Satijn et al., 2001; Duran-Matute et al., 2010). Moreover, for shallow axisymmetric swirl flows, only the parameter $\delta^2 \mathrm{Re}$ — where

---

[i]The contents of this chapter, with minor modifications, have been submitted in the form of a paper to *Physics of Fluids*.

Re is the Reynolds number and δ is the flow aspect ratio — characterizes the flow (Duran-Matute et al., 2010).

The work presented in the current chapter has been inspired by experimental work by Albagnac et al. (2010), who continued with the work by Lacaze et al. (2010) on laminar dipolar vortices generated by two closing flaps. Through a parametric study, Albagnac et al. (2010) investigated the dynamics of the spanwise vortex as a function of Re and δ and found that δ^2Re is a good parameter to determine the appearance of the spanwise vortex.

In the present chapter, we study numerically and experimentally the two-dimensionality of a decaying dipolar vortex as a function of both the Reynolds number Re and the aspect ratio δ of the initial dipole. The aim of this chapter is twofold: (i) to explain previous contradictory experimental results on the two-dimensionality of shallow flows, in particular that of a dipolar vortex where shallowness seems to promote the two-dimensionality of the flow (Sous et al., 2004), but even very shallow dipolar vortices can present complicated 3D structures (Akkermans et al., 2008b), and (ii) to test in a somewhat more complicated flow, namely the dipolar vortex structure, the scaling properties previously described in Chapter 3 for an axisymmetric monopolar vortex.

High-resolution 3D numerical simulations, together with the use of the so-called λ_2 vortex detection criterion (Jeong & Hussain, 1995; Wu et al., 2006), have revealed the full 3D structure of the dipole, providing new insight into the dynamics of shallow flows. Of special interest is the effect that secondary motions have on the 3D structure of the dipolar vortex as the parameter δ^2Re is increased. Furthermore, results from laboratory experiments show good agreement with the numerical simulations and give confidence in the robust character of the numerical results.

This chapter is organized as follows: in Section 6.2, the problem is formulated and the non-dimensional parameters characterizing the flow are defined. Section 6.3 is devoted to the numerical study of an initially Q2D dipolar vortex, where first, the numerical simulations are described. In Section 6.3.1, the strength of the 3D motions is quantified. Then, Section 6.3.2 presents the three different flow regimes observed for shallow dipoles. Finally, in Section 6.4 the laboratory experiments are presented and qualitatively compared with the numerical results. A discussion of the results and some conclusions are presented in Section 6.5.

6.2   Statement of the problem

We study a decaying symmetric dipolar vortex — a compact structure consisting of two counter-rotating vortex cores with equal strength and size — in a shallow fluid layer. Due to the strong interaction of the vortex cores, this structure propagates along a straight line (see e.g. Lamb, 1932).

The flow is considered to be governed by the Navier–Stokes equation

$$\frac{\partial \boldsymbol{v}}{\partial t} + (\boldsymbol{v} \cdot \boldsymbol{\nabla})\boldsymbol{v} = -\frac{1}{\rho}\boldsymbol{\nabla}p + \nu \nabla^2 \boldsymbol{v} \tag{6.1}$$

and the continuity equation for an incompressible fluid

$$\boldsymbol{\nabla} \cdot \boldsymbol{v} = 0, \tag{6.2}$$

with $\boldsymbol{v}$ the velocity of the fluid, t the time, ρ the density of the fluid, p the pressure, and ν the kinematic viscosity of the fluid. The motion of the fluid is described in Cartesian coordinates $\boldsymbol{x} = (x, y, z)$ with x the direction of propagation of the dipole, y the spanwise direction, and z the vertical direction. The velocity and vorticity vectors are then written as $\boldsymbol{v} = (u, v, w)$ and $\boldsymbol{\omega} = \boldsymbol{\nabla} \times \boldsymbol{v} = (\omega_x, \omega_y, \omega_z)$, respectively.

To nondimensionalize (6.1) and (6.2), the following nondimensional variables, which are denoted by primes, are defined:

$$\begin{aligned}
\boldsymbol{v}' &= \frac{\boldsymbol{v}}{U_0}, \quad \boldsymbol{\omega}' = \frac{R_0}{U_0}\boldsymbol{\omega}, \quad t' = \frac{U_0}{R_0}t, \quad p' = \frac{p}{\rho U_0^2} \\
x' &= \frac{x}{R_0}, \quad y' = \frac{y}{R_0}, \quad z' = \frac{z}{H},
\end{aligned} \tag{6.3}$$

where U_0 is the initial propagation speed of the dipole; R_0 is the initial radius of the dipole, and H is the depth of the fluid layer. Then, substituting (6.3) into (6.1) and (6.2) yields

$$\frac{\partial \boldsymbol{v}'}{\partial t'} + (\boldsymbol{v}' \cdot \tilde{\boldsymbol{\nabla}})\boldsymbol{v}' = -\tilde{\boldsymbol{\nabla}}p' + \frac{1}{\mathrm{Re}}\tilde{\nabla}^2 \boldsymbol{v}', \tag{6.4}$$

$$\tilde{\boldsymbol{\nabla}} \cdot \boldsymbol{v} = 0, \tag{6.5}$$

where

$$\tilde{\boldsymbol{\nabla}} \equiv \left(\frac{\partial}{\partial x'}, \frac{\partial}{\partial y'}, \frac{1}{\delta}\frac{\partial}{\partial z'} \right) \tag{6.6}$$

is the nondimensional gradient operator, and where the Reynolds number

$$\mathrm{Re} \equiv \frac{U_0 R_0}{\nu} \tag{6.7}$$

and the aspect ratio

$$\delta \equiv \frac{H}{R_0} \tag{6.8}$$

are the two nondimensional parameters characterizing the flow. To simplify notation, the primes will be omitted from here on, and only the nondimensional variables will be used.

6.3   Numerical simulations

In the present study, the governing equations (6.1) and (6.2) are solved numerically using a finite-element code (for more details see COMSOL AB, 2008). The numerical domain is $-9 \le x \le 21$, $0 \le y \le 15$, $0 \le z \le 1$. It has been previously observed that this domain size is large enough as not to affect the results of the simulations due to the effect of the lateral boundaries (Akkermans et al., 2008a).

As boundary conditions, a no-slip boundary condition is imposed at the bottom, whereas the surface is stress-free, flat, and rigid so that free-surface deformations are excluded. A stress-free condition is implemented for all lateral boundaries in order to further reduce the possible influence of these boundaries.

The flow is initialized in the horizontal plane with a Lamb–Chaplygin dipolar vortex with unit radius and a Poiseuille-like vertical structure according to

$$\boldsymbol{U}_{LC}(x,y) = \left(\frac{\partial \psi}{\partial y}, -\frac{\partial \psi}{\partial x}, 0 \right) \sin \left(\frac{\pi z}{2} \right),$$

where the streamfunction ψ is defined as:

$$\psi(r,\theta) = \begin{cases} -\dfrac{2}{\mu_1 J_0(\mu_1)} J_1 \left(\mu_1 r \right) \sin \theta, & r \le 1 \\[2mm] \left(r - \dfrac{1}{r} \right) \sin \theta, & r > 1 \end{cases} \tag{6.9}$$

with J_0 and J_1 the zeroth and first order Bessel functions of the first kind, and μ_1 the first zero of J_1. Note that $x = r\cos\theta$ and $y = r\sin\theta$ so that $r = \sqrt{x^2 + y^2}$ and $\theta = \tan^{-1}(y/x)$.

The Lamb–Chaplygin vortex dipole was chosen because of its resemblance to horizontal slices of experimentally created dipolar vortices (Flòr & Van Heijst, 1994; Billant & Chomaz, 2000; Sous et al., 2004, 2005; Sipp et al., 2000). The vertical Poiseuille-like structure was chosen since it seems to be a realistic profile for time-dependent shallow flows (Satijn et al., 2001).

Due to the symmetry with respect to the vertical plane $y = 0$, only the evolution of half of the dipole ($y > 0$) is simulated. However, for visualization purposes, the full dipolar vortex is reconstructed in the figures shown in this section.

The spatial resolution was checked by performing several simulations for two points in the (Re, δ) parameter space with increasing resolution until no significant differences were observed. This check resulted in a computational domain discretized with approximately 43000 unstructured mesh elements. A finer mesh was used in regions where high velocity gradients were expected. In addition, mesh elements in the vertical direction are between three and nine times smaller than the ones in the horizontal direction to resolve vertical gradients with sufficient resolution. In this way, the equations were solved for approximately 955000 degrees of freedom.

Time steps were determined by the numerical code using variable-order variable-step-size backward differentiation formulas (COMSOL AB, 2008) with the time

δ	Re
0.1	200, 300, 400, 800
0.2	50, 70, 100, 150, 200, 260, 500, 1000
0.3	25, 40, 50, 89, 100, 200, 222, 260
0.7	4, 8, 16, 40, 70, 90, 145

Table I – *Values of the Reynolds number Re and the aspect ratio δ used in the numerical simulations.*

resolution computed from the relative and absolute error tolerances. The values for such error tolerances were deduced by performing several simulations with decreasing tolerance until no significant difference between the simulations was observed.

The parameter space was explored by performing several numerical simulations for different values of the Reynolds number Re and the aspect ratio δ as shown in table I.

6.3.1 Quantitative characterization of the flow

As the dipolar vortex is left to evolve freely, secondary motions arise in the form of upwelling or downwelling in the vortex cores (Akkermans et al., 2008a) and in the form of a spanwise vortex at the front of the dipole (Sous et al., 2004; Akkermans et al., 2008a,b). To quantify the strength of these secondary motions, we consider the following quantities: (i) the normalized horizontal divergence at the surface ($z = 1$)

$$\Delta(t) = \frac{\displaystyle\int_{A_H} |\boldsymbol{\nabla} \cdot \boldsymbol{v}(x, y, 1, t)| \, \mathrm{d}x\mathrm{d}y}{\displaystyle\int_{A_H} \left| \hat{\boldsymbol{k}} \cdot \boldsymbol{\nabla} \times \boldsymbol{v}(x, y, 1, t) \right| \mathrm{d}x\mathrm{d}y}, \tag{6.10}$$

(as previously used by Akkermans et al., 2008a) and (ii) the normalized kinetic energy of the vertical velocity component in the vertical symmetry plane $y = 0$

$$Q_z(t) = \frac{\displaystyle\int_{A_V} w^2(x, 0, z, t)\mathrm{d}x\mathrm{d}z}{\displaystyle\int_{A_V} u^2(x, 0, z, t)\mathrm{d}x\mathrm{d}z} \tag{6.11}$$

(as previously used by Sous et al., 2004), where A_H is the horizontal area of the numerical domain; A_V is the area of the vertical symmetry plane, and $\hat{\boldsymbol{k}}$ is the unit vector in the z direction. In particular, we focus on the maximum in time of these two quantities: $\max(\Delta)$ and $\max(Q_z)$.

The surface $z = 1$ was chosen to evaluate the horizontal divergence Δ since $w = 0$ on this plane, and hence, the divergence is the only signature of the secondary
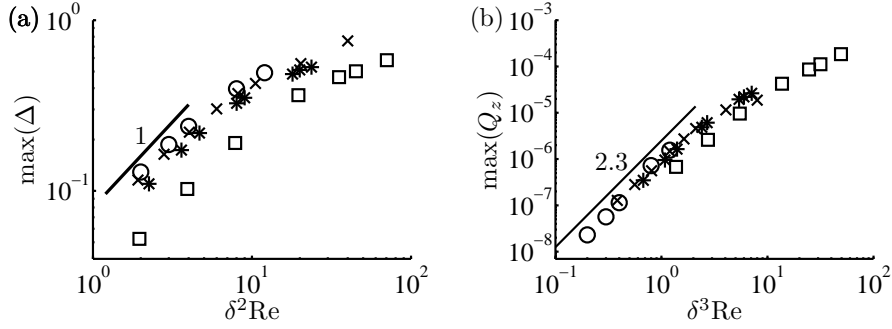
Figure 6.1 – *Relative strength of the secondary motions with respect to that of the primary motion: (a) maximum of the horizontal divergence at the surface as a function of $\delta^2 Re$; (b) maximum of the kinetic energy of the vertical velocity component in the vertical symmetry-plane as a function of δ^3Re. The symbols denote simulations for different values of Re and $\delta = 0.1$ (○), $\delta = 0.2$ (×), $\delta = 0.3$ (∗), and $\delta = 0.7$ (□). The solid lines represent the different scalings.*

motions. Similarly, in the vertical symmetry plane ($y = 0$), the vertical velocity is the only signature of the secondary motions.

To quantify the strength of the secondary motions in an axisymmetric monopolar vortex, the flow can be easily decomposed, using cylindrical coordinates, into the primary motion in the azimuthal direction and secondary motions in the radial and vertical directions (see e.g. Satijn et al., 2001; Duran-Matute et al., 2010). For the case of the monopolar vortex, the horizontal divergence is related to the radial velocity, and hence, it only depends on δ^2Re for $\delta \ll 1$. On the other hand, the magnitude of the vertical velocity only depends on δ^3Re (see Duran-Matute et al., 2010).

Figure 6.1(a) shows the maximum of the horizontal divergence, max(Δ), as a function of δ^2Re. A collapse of the curves for $\delta = 0.1$, $\delta = 0.2$, and less clearly for $\delta = 0.3$ is observed. This collapse indicates — as for the monopolar vortex (Duran-Matute et al., 2010) — that shallow dipoles are characterized by only one nondimensional parameter: δ^2Re, provided that $\delta \ll 1$. However, the results given by simulations with $\delta = 0.7$ do not collapse with the curves described by the results for simulations with $\delta = 0.1$, 0.2 since $\delta = 0.7$ is not small enough (i.e. the flow is not shallow enough) for the flow evolution to depend solely on the parameter δ^2Re. In addition, the graph clearly shows the existence of a scaling regime for δ^2Re $\lesssim 6$ where max(Δ) $\propto \delta^2$Re. In comparison with a monopolar vortex, the scaling max(Δ) $\propto \delta^2$Re implies that the flow is dominated by viscosity in this regime and that the secondary motions can be neglected. On the other hand, inertia dominates over viscous forces outside this regime.

In figure 6.1(b), the maximum of the kinetic energy associated with the vertical velocity max(Q_z) is plotted as a function of δ^3Re. Again, a good collapse is observed for the results of the simulations with $\delta = 0.1$, 0.2 and 0.3, indicating
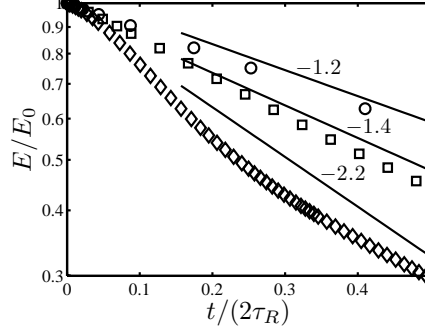
Figure 6.2 – *Numerically obtained kinetic energy decay at the surface $z = 1$ for three different simulations with $\delta = 0.2$: Re = 50 ($\circ$), Re = 200 ($\square$), and Re = 500 ($\diamond$).*

that the magnitude of the vertical velocity depends only on δ^3Re. In contrast, the results from the simulations with $\delta = 0.7$ do not collapse to the same curve. As for the monopolar vortex (Duran-Matute et al., 2010), a scaling regime is found for $\delta^3 \text{Re} \lesssim 1$ although the exponent is somewhat larger for the dipolar vortex. Outside this scaling regime, the secondary motion cannot be neglected, and hence the flow must be considered as 3D.

A few simulations with different initial vertical profiles, including a vertical profile that is independent of the vertical coordinate, were performed. It was observed that the scaling in the viscosity-dominated regime is independent of the initial vertical velocity profile. In contrast, the trend in outside this regime does depend on the initial vertical velocity profile. However, the viscous regime and the inertia-dominated regime never show the same scaling, implying that the two regimes are easily distinguishable.

To further characterize the flow, we calculate the typical decay time τ_D by fitting an exponential decay to the normalized kinetic energy associated to the horizontal velocity components at the surface $z = 1$

$$\frac{E(t)}{E_0} = \frac{\int_{A_H} [u^2(x, y, 1, t) + v^2(x, y, 1, t)] \mathrm{d}x \mathrm{d}y}{\int_{A_H} [u^2(x, y, 1, 0) + v^2(x, y, 1, 0)] \mathrm{d}x \mathrm{d}y}. \tag{6.12}$$

The decay time τ_D is then compared with the Rayleigh decay time

$$\tau_R = \frac{4}{\pi^2} \delta^2 \text{Re}, \tag{6.13}$$

[equivalent to $4H^2/(\pi^2 \nu)$ in dimensional units] being the typical decay time for shallow flows dominated by bottom friction (Satijn et al., 2001; Paret et al., 1997).

Figure 6.2 shows the normalized kinetic energy as a function of time (normalized by the Rayleigh decay time τ_R) for $\delta = 0.2$ and Re = 50, 200 and 500. By

fitting an exponential curve to the evolution of the kinetic energy, it can be seen that for small Reynolds numbers (e.g. Re = 50), the characteristic decay time $\tau_D \sim \tau_R/1.2$ is close to the Rayleigh decay time. However, as the Reynolds number increases and the flow becomes 3D, the decay time becomes much shorter: $\tau_D \sim \tau_R/1.4$ for Re = 200 and $\tau_D \sim \tau_R/2.2$ for Re = 500. For Re = 50 the difference between τ_D and τ_R is probably due to horizontal diffusion, which enhances the viscous decay. However, for larger values of Re, the difference between τ_D and τ_R is due to the 3D dynamics of the flow: the advection of fluid by the secondary motion towards a thin boundary layer at the bottom. This advection increases the damping rate, like the Ekman boundary layers do for flows subjected to background rotation; see, for example, Pedlosky (1987).

6.3.2   Flow regimes for shallow dipolar vortices

For the simulations of shallow dipoles ($\delta = 0.1, 0.2, 0.3$), three qualitatively different flow regimes were observed in the range of Re-values investigated. Since the characteristics of shallow dipoles depend exclusively on the value of δ^2Re, we base the description of the different regimes on the simulations with $\delta = 0.2$, which are characteristic for simulations with other aspect ratios much smaller than unity (e.g. $\delta = 0.1$ and 0.3). As δ approaches unity (e.g. $\delta = 0.7$), the characteristics of the flow depend both on the values of δ and Re; it is not within the scope of the current work to analyze such cases.

The description of the three regimes for shallow dipoles is mainly based on their 3D structure. To determine this structure, we used the λ_2 vortex detection criterion proposed by Jeong & Hussain (1995) that allows to find the locations of local pressure minima in the flow that correspond to the presence of vortices. This detection criterion consists in calculating the real eigenvalues $\lambda_1 \geq \lambda_2 \geq \lambda_3$ of the symmetric tensor $\boldsymbol{S}^2 + \boldsymbol{\Xi}^2$, where $\boldsymbol{S}$ and $\boldsymbol{\Xi}$ are the symmetric and antisymmetric components of $\boldsymbol{\nabla v}$, respectively. Then, the sectional pressure minimum induced by a vortex corresponds to regions where the second eigenvalue of $\boldsymbol{S}^2 + \boldsymbol{\Xi}^2$ is negative: $\lambda_2 < 0$. Hence, the 3D boundary of a vortical structure is given by the isosurface $\lambda_2 = 0$. For more details see also Wu et al. (2006).

Quasi-two-dimensional (Q2D) flow regime ($\delta^2\text{Re} \lesssim 6$)

Figure 6.3 shows the evolution of the dipolar vortex for a simulation corresponding to Re = 50 and $\delta = 0.2$ ($\delta^2\text{Re} = 2$). In the top row of figure 6.3, colors denote the magnitude of the vertical vorticity ω_z and the black contour denotes the boundary of the vortex dipole as given by λ_2-criterion for $t = 0.5$, 1, and 2 at the surface ($z = 1$). As can be seen from the vertical vorticity ω_z distribution, the structure of the vortex dipole remains coherent. This is also reflected by the boundary of each vortex core, which describes approximately a circle throughout the flow evolution. In fact, only a weak increment, due to diffusion, in the size of the structure can be perceived.
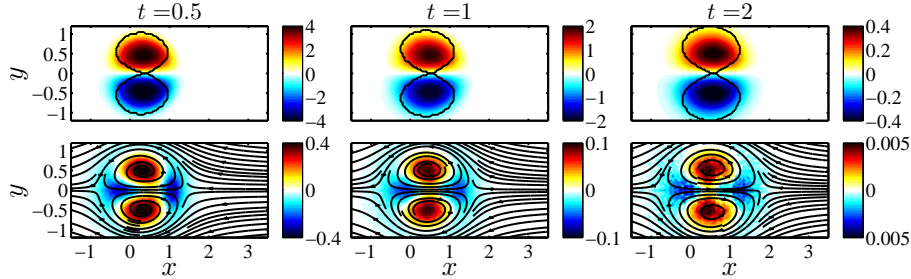
Figure 6.3 – *Evolution of a dipolar vortex at the surface ($z = 1$) for a simulation with Re = 50 and $\delta = 0.2$ (δ^2Re = 2) at times $t = 0.5$, 1, and 2. Top row: the color denotes the vertical vorticity component ω_z, and the black contour denotes the boundary of the vortex cores given by the $\lambda_2 = 0$ isoline. Lower row: the color denotes the horizontal divergence and the black lines denote the flow lines tangential to the horizontal velocity components in the reference frame co-moving with the vortex dipole.*

In the lower row of figure 6.3, the colors denote the horizontal divergence ($\partial u/\partial x + \partial v/\partial y$) and the black lines indicate the flow lines tangential to the horizontal velocity components in the reference frame co-moving with the dipolar vortex. By comparing the top and lower rows in figure 6.3, it can be observed that, at the surface ($z = 1$), the positions of the primary vortex cores delineated by the $\lambda_2 = 0$ isoline correspond to areas of positive horizontal divergence. It is already known that a vortex with its rotation axis normal to a solid bottom induces an upwelling from the Bödewadt boundary layer into the vortex core (Bödewadt, 1940). Then, this upwelling induces a radial diverging flux at the surface. Downwelling areas are associated with converging fluxes, which are found close to the saddle type stagnation points at the front and at the rear of the dipolar vortex on its symmetry axis.

In the lower row of figure 6.3, the instantaneous flow lines tangential to the horizontal velocity components define quasi-closed loops around a focal point corresponding to the vertical vorticity extrema. This suggests that the flow is mainly horizontal and that the upwelling is negligible when compared to the primary dipole. Thus, the flow at the surface suggests that the dipolar vortex with Re = 50 and $\delta = 0.2$ remains Q2D during its lifetime.

Figure 6.4 shows the spanwise vorticity ω_y in the vertical symmetry plane of the dipolar vortex ($y = 0$) at times $t = 0.5$, 1, and 2 for the simulation with Re = 50 and $\delta = 0.2$ (δ^2Re = 2). From the contours of ω_y, it can be seen that the flow structure in the vertical symmetry plane barely changes in time. Only at early times ($t \approx 0.5$), a small deviation from the initial shape is observed.

In figure 6.5, the 3D structure of half of the vortex dipole is illustrated by the $\lambda_2 = 0$ isosurface at time $t = 1$ for two simulations : one simulation with Re = 50 and $\delta = 0.2$ (δ^2Re = 2) and one with Re = 25 and $\delta = 0.3$ (δ^2Re = 2.25). In this figure, it is clear that the vortex structure is 2D (independent of the vertical coordinate) even though the velocity field itself is 3D. All along its evolution, the
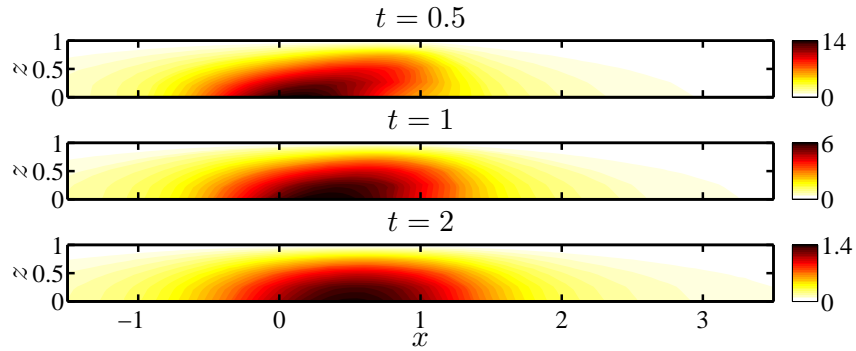
Figure 6.4 – *Evolution of the flow in the vertical symmetry ($y = 0$) plane for a simulation with* Re $= 50$ *and* $\delta = 0.2$ *(δ^2Re $= 2$) at times $t = 0.5$, 1, and 2. The color denotes the spanwise vorticity component ω_y.*
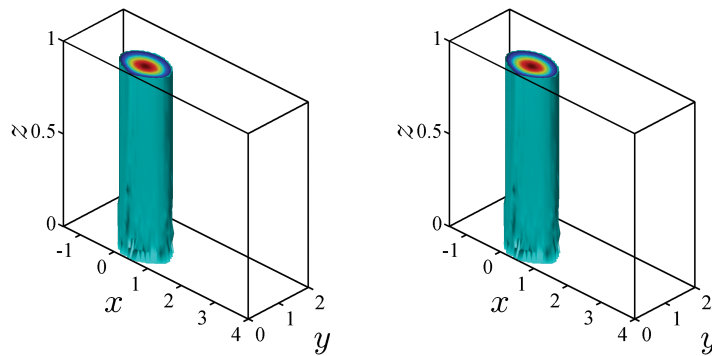
Figure 6.5 – *3D structure of half of the dipolar vortex ($y > 0$) for two simulations at time $t = 1$. Left:* Re $= 50$ *and* $\delta = 0.2$ *(δ^2Re $= 2$). Right:* Re $= 25$ *and* $\delta = 0.3$ *(δ^2Re $= 2.25$). The structure is given by the isosurface $\lambda_2 = 0$ following the λ_2-criterion.*

Figure 6.6 – *Same as in figure 6.3, except for a simulation with* Re = 200 *and* δ = 0.2 *(δ^2Re = 8).*

dipolar vortex maintains this 2D structure. The described characteristics can also be observed for other small values of δ and similar values of δ^2Re, as shown, for example, in figure 6.5 for the simulation with $\delta = 0.3$ and δ^2Re = 2.25.
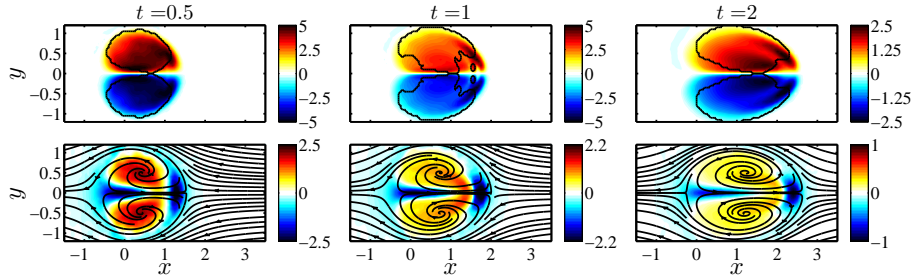
Transitional flow regime ($6 \lesssim \delta^2$Re $\lesssim 15$)

Figure 6.6 shows the evolution of the dipolar vortex obtained from a simulation with Re = 200 and $\delta = 0.2$ (δ^2Re = 8). Color coding and black lines have the same meaning as in figure 6.3. As can be observed, the vorticity extrema no longer correspond with the primary vortex centroids. Instead, they are found at the front of the dipolar vortex and close to its symmetry axis. In the frontal region, the vertical vorticity extrema extend along the boundary of the dipolar vortex specially at late times (e.g. $t = 1$ and $t = 2$). However, the area bounded by the $\lambda_2 = 0$ isoline remains coherent.

In the lower row of figure 6.6, it can be seen that, as for the Q2D regime, there exists a patch of positive divergence at each of the cores of the dipolar vortex. The presence of this horizontal divergence can be observed in the form of the flow lines spiraling out of the primary vortex centroids suggesting the existence of a secondary flow that cannot be neglected. In addition, there exist two patches of converging flow (negative horizontal divergence) corresponding to downwelling areas. These areas are found along the axis of the dipolar vortex as well as in front of the dipole. In the positive divergence areas, vertical vortex tubes just below the surface are compressed, while in the negative divergence areas the vertical vortex tubes are stretched by the secondary motion. This stretching/compression mechanism is responsible for the local vorticity maxima in the negative divergence area.

Figure 6.7 shows the distribution of spanwise vorticity ω_y in the vertical symmetry plane of the vortex dipole ($y = 0$) at times $t = 0.5$, 1, and 2 for the simulation with Re = 200 and $\delta = 0.2$ (δ^2Re = 8). In this flow regime, we observe a viscous boundary layer, which is generated by the dipolar vortex propagating above the solid bottom and which is characterized by high spanwise vorticity close to the bottom. Then, fluid with high spanwise vorticity from the boundary layer
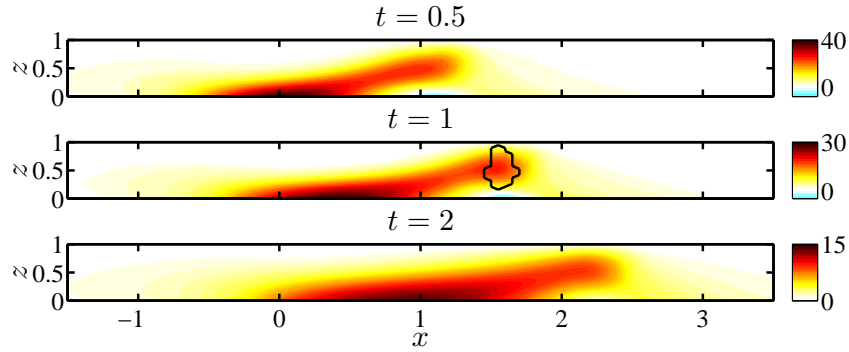
Figure 6.7 – *Same as in figure 6.4, except for the simulation with* $\mathrm{Re} = 200$ *and* $\delta = 0.2$ *($\delta^2\mathrm{Re} = 8$). The black contour denotes the* $\lambda_2 = 0$ *isoline.*
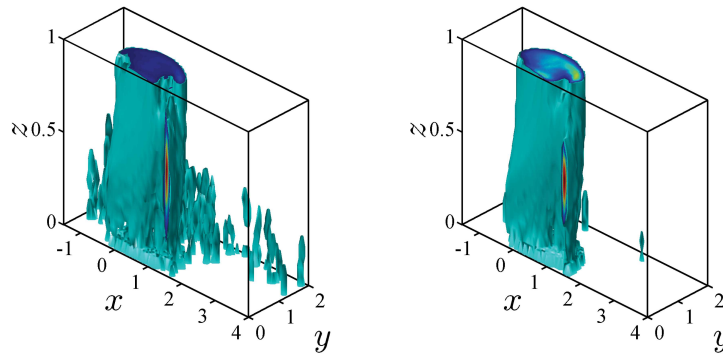
Figure 6.8 – *Same as in figure 6.5, except for the simulations with* $\mathrm{Re} = 200$ *and* $\delta = 0.2$ *($\delta^2\mathrm{Re} = 8$) (left) and with* $\mathrm{Re} = 89$ *and* $\delta = 0.3$ *($\delta^2\mathrm{Re} = 8$) (right).*

is entrained towards the front of the dipole and forms a frontal circulation at mid-depth. In the current regime, this region of spanwise vorticity exists during most of the evolution, and at intermediate times ($t \approx 1$), a spanwise vortex is detected by the λ_2-criterion. The formation of the spanwise vortex can be partly attributed to vortex stretching in the spanwise direction, $\omega_y \partial v/\partial y$, which is of particular importance at the front of the dipole along its separatrix. Shortly after its appearance, the spanwise vortex vanishes as viscous effects start to dominate over vortex stretching due to decay of the dipolar vortex. At $t = 2$, a patch of spanwise vorticity remains at the front of the dipole, but this vorticity patch is no longer a vortex.

Figure 6.8 shows the isosurface of the 3D λ_2-criterion for two simulations with $\delta^2\mathrm{Re} = 8$ and two different values of δ ($\delta = 0.2$ and 0.3) at time $t = 1$. Here, the structure defined by the λ_2-criterion contains both the primary vortex and the spanwise vortex at the front of the dipole. In figure 6.8, the $\lambda_2 = 0$ isosurface is

Figure 6.9 – *Same as in figure 6.3, except for a simulation with* Re = 500 *and* $\delta = 0.2$ *(δ^2Re = 20).*

a coherent column as for the Q2D regime. However, the circular horizontal cross section is distorted due to the presence of the spanwise vortex and other 3D effects. In this figure, apparently, the flow structure is similar for different small values of δ and the same value of δ^2Re.

Three-dimensional (3D) flow regime (δ^2Re $\gtrsim 15$)

Figure 6.9 shows the evolution of the dipolar vortex for the simulation with Re = 500 and $\delta = 0.2$ (δ^2Re = 20). Color coding and black lines have the same meaning as in figure 6.3. For this regime, as in the transitional one, the local vorticity extrema are found close to the axis of the dipolar vortex and at its front where they extends along its boundary. However, due to the stronger concentration of vorticity at the edges of the dipole, the $\lambda_2 = 0$ isoline at the surface loses its circular shape. The boundary given by the λ_2-criterion becomes first an annulus and then an elongated structure that surrounds the cores of the dipolar vortex. In this regime, the boundary of the vortices at the surface, given by the $\lambda_2 = 0$ isoline, indicates an important modification of the primary structure in comparison with the previous regimes.

In the lower row of figure 6.9, it can be seen that the horizontal divergence field is again composed of two patches of positive divergence in the cores of the dipolar vortex and two patches of converging flow: one along the axis of the dipolar vortex dipole and another at its front. As in the previous regime, the presence of this horizontal divergence can be observed in the form of the flow lines spiraling out of the primary vortex centroids suggesting the existence of a secondary flow that cannot be neglected.

Figure 6.10 shows the distribution of spanwise vorticity ω_y in the vertical symmetry plane ($y = 0$) of the vortex dipole at times $t = 0.5$, 1 and 2 for the simulation with Re = 500 and $\delta = 0.2$ (δ^2Re = 20). The magnitude of the spanwise vorticity in the vertical symmetry plane is much higher than the vertical vorticity of the primary vortex. As in the transitional regime, there is a viscous boundary layer close to the bottom below the primary vortex and a patch of spanwise vorticity ω_y at the front of the dipole at approximately mid-depth. The λ_2-criterion detects the
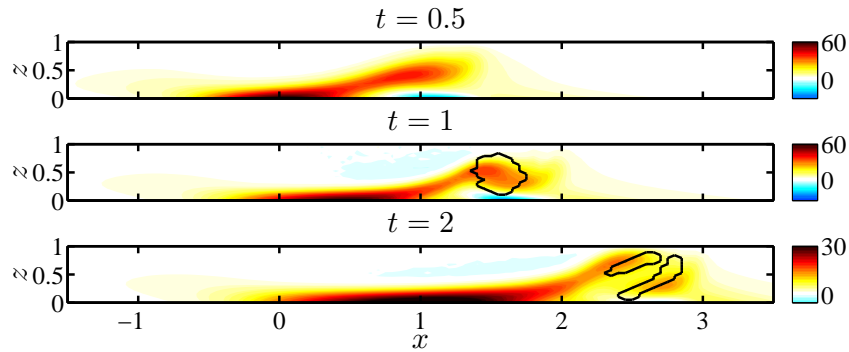
Figure 6.10 – *Same as in figure 6.4, except for a simulation with* Re = 500 *and* δ = 0.2 *(δ²Re = 20). The black contour denotes the* $\lambda_2 = 0$ *isoline.*
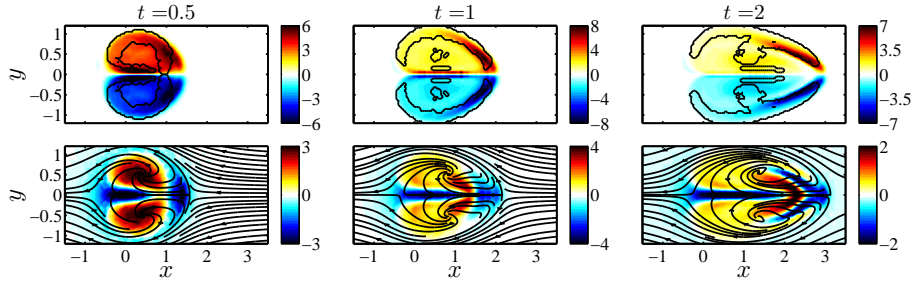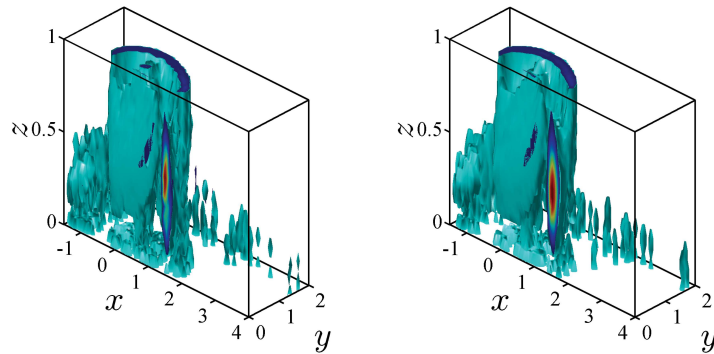

Figure 6.11 – *Same as in figure 6.5, except for the simulations with* Re = 500 *and* δ = 0.2 *(δ²Re = 20) (left) and* Re = 222 *and* δ = 0.2 *(δ²Re = 20).*

presence of a spanwise vortex, which develops after some time (see time $t = 1$ and 2 in figure 6.10). In comparison to the transitional regime, the spanwise vortex is present for a longer time since viscous effects outside the boundary layer are negligible as compared with inertia forces for a longer time.

Figure 6.11 shows the $\lambda_2 = 0$ isosurface, outlining the boundary of the dipolar vortex for $y \geq 0$ at time $t = 1$ for two simulations with $\delta^2\text{Re} = 20$ and two different values of δ ($\delta = 0.2$, 0.3). Here again the volume defined by the $\lambda_2 = 0$ isosurface contains both the primary dipolar vortex and the spanwise vortex located at its front. It can be seen that in this regime, the 3D structure of the vortex depends strongly on the vertical direction: the shape is modified by the presence of the spanwise vortex at mid-depth, and at the top, the vortex core is hollow.
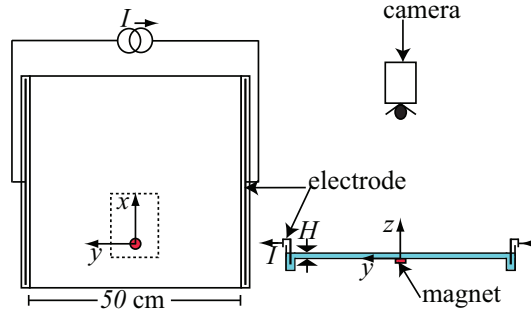
Figure 6.12 – *Schematic representation of the experimental setup.*

6.4 Laboratory experiments

6.4.1 Experimental setup

The experimental setup, shown schematically in figure 6.12, consists of a water tank with a base of 50×50 cm^2 which is filled with a salt solution with a 178 g/l concentration up to a depth of 0.5 cm. To force the flow, two titanium electrodes are placed along two opposite sides of the tank, and one cylindrical magnet with a 2.5 cm diameter is placed underneath the tank bottom. An electric current is forced through the fluid using a power supply. Due to the interaction of this electric current and the magnetic field of the magnet, a Lorentz force is generated

$$\boldsymbol{F} = \boldsymbol{J} \times \boldsymbol{B}, \tag{6.14}$$

with $\boldsymbol{J}$ the current density and $\boldsymbol{B}$ the magnetic field, by which the fluid is set in motion. In the current study, the fluid is forced for 1 s, and then it is left to evolve freely. The initial time $t = 0$ is taken to be at the end of the forcing period. A similar forcing method has been previously used successfully to create dipolar vortices in a shallow fluid layer (Akkermans et al., 2008a,b), which have an initial radius similar to the diameter of the magnet: $R_0 \approx 2.5$ cm. In this way, the aspect ratio of the dipoles is $\delta \approx 0.2$ for our experiments.

We consider the electric current to be homogeneous and running only in the y-direction, while the main component of the magnetic field above the center of the magnet is in the z-direction. Hence, the principal component of the Lorentz force is in the x-direction, thus forcing a dipolar vortex that propagates in this direction.

Particle Image Velocimetry (PIV) is used to measure the horizontal velocity field of the flow in a horizontal plane 3 mm above the bottom. The fluid is seeded with 106–150 μm polymethylmethacrylate (PMMA) particles, which are illuminated with a double pulsed Nd:YAG laser sheet. Images of a 12×9 cm^2 area of the tank are taken using a Megaplus digital camera with a resolution of 1600×1200 pixels. Images at different time intervals are chosen, depending on the maximum velocity of the flow. These are then cross-correlated using PIV software

Figure 6.13 – *(Color online) Vertical vorticity field in the horizontal plane $z = 0.6$ (3 mm above the bottom) for three experiments at $t = 1$. The color denotes the vertical vorticity ω_z. The parameters for each experiment are shown above each panel.*
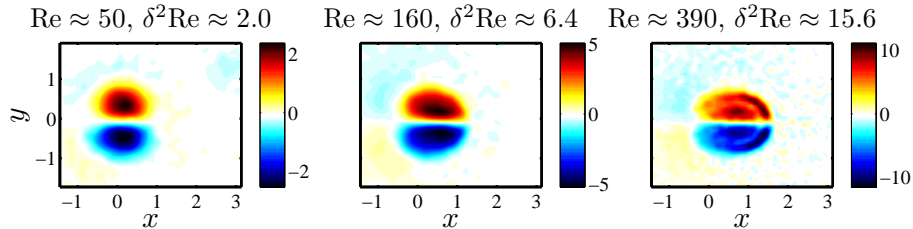
from PIVTEC GmbH, Göttingen, Germany to calculate the horizontal velocity field.

In the current chapter, results for three experiments are presented. These experiments were performed with three different magnitudes of the electric current, which resulted in three different values of the strength of the dipolar vortex. For the experiment with the lowest electric current, a picture was taken every 200 ms. Then each picture was correlated with the following picture using the PIV software. For the experiments with moderate and strong forcing, a pair of images was taken every 1/15 s, with a time interval between each picture of 10 ms or 25 ms depending on the magnitude of the electric current. Then, each image pair was correlated. The three experiments presented in this chapter correspond to Re $\approx$ 50, 160, 390, and they are representative of each of the three regimes described in the numerical study.

6.4.2 Experimental results

Figure 6.13 shows the vertical vorticity in the horizontal plane $z = 0.6$ at time $t = 1$ for three experiments. In this figure, the vortex dipole can be easily distinguished. However, the primary vortex dipole is surrounded by weak vorticity regions, which are typical of the forcing method employed and which are not found in the results from the numerical simulations. Due also to the generation mechanism, the initial vertical profile of the horizontal velocity is not Poiseuille-like as in the simulations. Instead, the horizontal velocities are stronger close to the bottom than at the surface since the forcing is stronger at the bottom (i.e. closer to the magnet)(Akkermans et al., 2008a). In spite of these differences, the resulting evolution of the dipolar vortex in the laboratory experiments is in good agreement with the evolution of the dipolar vortex in the numerical simulations. This agreement indicates that the observed characteristics of the flow evolution do not depend critically on the precise form of the initial condition. For example, it can be observed that the dipolar vortex remains coherent for small values of δ^2Re (δ^2Re $\approx$ 2.0), i.e. in the viscosity dominated regime. For intermediate values of δ^2Re (δ^2Re $\approx$ 6.4), a slight elongation of the dipolar vortex can be observed
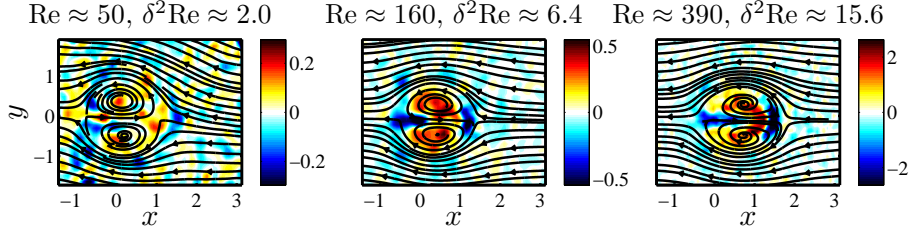
Figure 6.14 – *Horizontal divergence and flow lines tangential to the horizontal velocity components in the horizontal plane $z = 0.6$ for three experiments at $t = 1$. The color denotes the horizontal divergence $\partial u/\partial x + \partial v/\partial y$. The parameters for each experiment are shown above each panel.*

with bands of vertical vorticity maxima close to the symmetry axis of the dipole. Finally, for large values of $\delta^2\mathrm{Re}$ ($\delta^2\mathrm{Re} \approx 15.6$), the dipolar vortex is fully divided into a band of high vorticity at the front and patches of high vorticity close to the symmetry axis of the dipole.

Figure 6.14 shows the instantaneous flow lines tangential to the horizontal velocity components in the reference frame co-moving with the dipole and the horizontal divergence at $t = 1$ for the same three experiments as shown in figure 6.13. For $\delta^2\mathrm{Re} \approx 2.0$, the horizontal divergence is very small and below the accuracy of our measurements. Therefore, the horizontal divergence field is very noisy. On the other hand, for intermediate values of $\delta^2\mathrm{Re}$ ($\delta^2\mathrm{Re} \approx 6.4$), two patches of positive horizontal-divergence in the primary vortex cores indicate upwelling areas as in the numerical simulations. Downwelling is clearly observed at the front and close to the symmetry axis of the dipolar vortex. For large values of $\delta^2\mathrm{Re}$ ($\delta^2\mathrm{Re} \approx 15.6$), the horizontal divergence distribution is the same as for intermediate values, except in the frontal region of the dipolar vortex. In this region, two narrow bands of horizontal divergence with opposite sign indicate the presence of a spanwise vortex. In addition, the flow lines clearly spiral out from the primary vortex centroids indicating the presence of non-negligible secondary motions.

The generation mechanism used in the experiments does not seem to have a large effect on the overall characteristics of the flow evolution. For example, Lacaze et al. (2010) performed one experiment where the dipole was generated using two closing flaps with $\delta = 0.3$ and $\delta^2\mathrm{Re} = 20$ (this is the same value of $\delta^2\mathrm{Re}$ used in the simulations presented for the 3D flow regime). In this experiment, the vorticity extrema were found in bands at the front of the dipole and close to its symmetry axis, and a strong spanwise vortex developed like also observed in our experiments and numerical simulations.

We further characterize the flow by comparing the decay time τ_D of the vortex dipole with the Rayleigh decay time τ_R in the same way as it was done for the numerical simulations (see figure 6.15). The decay time for the Q2D flow (Re ≈ 50, $\delta^2\mathrm{Re} \approx 2.0$) is close to the Rayleigh decay time: $\tau_D \sim \tau_R/1.2$. However, as the Reynolds number increases and the flow becomes 3D, the decay time becomes
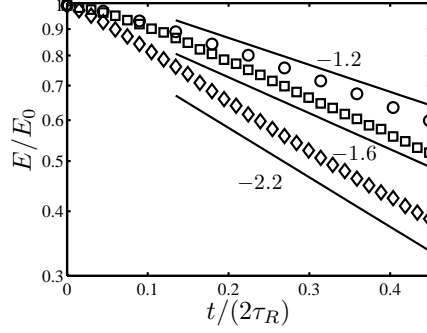
Figure 6.15 – *Normalized kinetic energy as a function of time for the three experiments in the horizontal plane $z = 0.6$ for three experiments with $\delta \approx 0.2$, and Re ≈ 50 ($\circ$), Re ≈ 160 ($\square$), and Re ≈ 390 ($\diamond$). The solid lines are exponential fits.*

much shorter: $\tau_D \sim \tau_R/1.6$ for Re ≈ 160 and $\tau_D \sim \tau_R/2.2$ for Re ≈ 390.

6.5   Discussion and conclusions

In the last decade, several studies have shown different results about the effects of shallowness on the two-dimensionalization of flows. A good example is found in the case of dipolar vortices (Sous et al., 2004, 2005; Akkermans et al., 2008b,a). On one hand, shallowness seems to reduce vertical motions, but on the other hand, complicated three-dimensional structures have been observed even for very shallow flows.

In the present work, we explain the apparently contradictory results from previous studies by performing a detailed exploration of the parameter space (Re, δ) both numerically and experimentally. It was found that the three-dimensionality of shallow dipolar vortices strongly depends on both the Reynolds number Re and the aspect ratio δ of the flow. However, for small values of δ (i.e. for shallow layers of fluid), the relative strength of the secondary motion only depends on the product δ^2Re. This dependence on δ^2Re and the existence of different flow regimes is in agreement with previous results for the monopolar vortex (Duran-Matute et al., 2010).

For shallow ($\delta \ll 1$) dipolar vortices and the range of Reynolds numbers investigated in this chapter, we observed three qualitatively different regimes:

1. **Q2D flow regime.** For low values of δ^2Re (δ^2Re $\lesssim 6$) the flow is dominated by viscous effects and the secondary motions can be neglected. Note that, even if the velocity field is z-dependent, the three-dimensional structure of the dipolar vortex, given by the λ_2-criterion, is clearly 2D in this regime (see figure 6.5).

2. **Transitional regime.** For intermediate values of δ^2Re ($6 \lesssim \delta^2$Re $\lesssim 15$),

even if the vortex remains a coherent structure, secondary motions cannot be neglected since they modify the primary dipolar vortex. In addition, a spanwise vortex is observed at the front of the dipolar vortex. However, this spanwise vortex is not strong enough to endure the viscous effects for a long time.

3. **3D regime.** For large values of $\delta^2 \mathrm{Re}$ ($\delta^2 \mathrm{Re} \gtrsim 15$) the distribution of the vertical vorticity component is intrinsically modified. The initial coherent horizontal distribution of vertical vorticity becomes 'hollow', with vorticity extrema close to the axis of the dipole and at its front. The overall structure of the dipole becomes three-dimensional due to strong secondary motions (both in the primary vortex cores and in the spanwise vortex located at the front of the dipole) that cannot be neglected.

The different initial conditions in both numerical and laboratory experiments result in small quantitative differences in the position of the transition regime in the parameter space. However, there is a strong qualitative similarity between experimentally and numerically obtained shallow ($\delta \ll 1$) dipolar vortices. This similarity suggests that the existence of the different flow regimes that depend only on the value of $\delta^2 \mathrm{Re}$ is a robust property of shallow dipolar vortices, irrespective of the initial condition. A similar conclusion was reached for shallow monopolar vortices (Duran-Matute et al., 2010). In this way, the three-dimensionalization of shallow flows depending exclusively on the parameter $\delta^2 \mathrm{Re}$ seems to be valid for numerous kinds of shallow vortical flows.

Chapter 7

Stationary dipolar structure[i]

7.1 Introduction

Electromagnetic (EM) forcing of conducting fluids is non-intrusive, and for this reason, it is an unparalleled tool for the study of a large variety of flows. In particular, EM forcing has been used in shallow layers of electrolytes to study, for example, quasi-two-dimensional turbulence (Tabeling et al., 1991; Clercx et al., 2003), shallow vortices (Akkermans et al., 2008b), stability of shear flows (Dolzhanskii et al., 1992), fully controllable multiscale flows (Rossi et al., 2006), and the principles of stretching and folding in quasi-two-dimensional flows (Voth et al., 2002). In addition, research of this type of forcing has been motivated by its applications on EM mixing and stirring in metallurgy (Davidson, 1999) and the enhancement of turbulent heat transfer (Kenjereš, 2008).

Due to the many uses of EM forcing, it is of interest to characterize the response of the flow to the forcing. In the case of a shallow layer of electrolyte, Bodarenko et al. (1979) considered, in the first reported experiments of this kind, that the induced fluid velocity is proportional to the magnitude of the EM forcing. Tabeling et al. (1987) also observed a linear dependence but only up to a well-defined forcing threshold. Above this threshold it was observed that the rate of increase of the velocity with the forcing is smaller. Despite its limitations at relatively strong forcing magnitudes, the linear relationship has been used in many theoretical studies; see e.g. Dauxois et al. (1996) and Thess (1992).

In more recent experiments on a system of four vortices, the maximum velocity was measured as a function of the forcing, and it was found that the deviations from the linear dependence were small (Danilov & Dovzhensko, 1996). However, the same experimental data were recently reanalyzed (Ponomarev et al., 2009), and for relatively high forcing magnitudes, the maximum velocity seemed to scale with

---

[i]The contents of this chapter, with minor modifications, have been submitted in the form of a paper to *Physical Review E.*
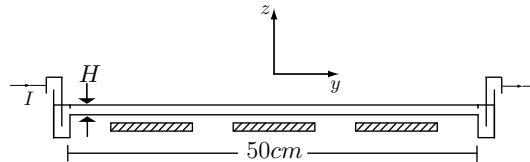
Figure 7.1 – *Side view of the experimental setup. The hatched rectangles denote the magnets below the tank.*

the forcing than linearly but to the power 2/3; the latter behavior is in agreement with theoretical results where secondary motions and different vertical velocity profiles were taken into account. Figueroa et al. (2009) examined the structure of a laminar dipolar vortex driven by a time-independent EM force in a shallow layer of electrolyte. They observed that the maximum velocity in the flow as a function of the forcing magnitude fits a second order polynomial. However, no physical reason was given for such a fit.

It is the aim of the present paper to determine experimentally the scaling of the magnitude of the flow velocity in a shallow layer of electrolyte forced electromagnetically as a function of the relevant parameters: the forcing magnitude (which is characterized by the Chandrasekhar number Ch) and the aspect ratio δ of the depth to the horizontal scale of the flow. In contrast with previous studies, we extend the parameter regime to strong forcing magnitudes and focus on the underlying physical mechanisms associated with the different flow behaviors. We quantify the response of the flow by measuring the horizontal velocity field of a simple electromagnetically forced flow — a dipolar flow structure — while exploring the parameter space. Two well-defined regimes were observed: the linear regime discussed previously and a regime where the velocity scales with the magnitude of the forcing to the power 1/2. Furthermore, it is found that the flow depends only on the parameter δ^2Ch for the whole range of parameters studied.

The chapter is organized as follows. The experimental setup is described in Section 7.2. Section 7.3 is devoted to the dimensional analysis of the problem. Section 7.4 presents the experimental results. Then, in Section 7.5 the implications for previous and future work are discussed, and finally, some conclusions are outlined in Section 7.6.

7.2 Experimental setup

The experimental setup consists of a fluid tank with a base of 30×50 cm^2, which is filled with a salt solution with a concentration of 178 g l^{-1} to a depth H and covered with a transparent perspex lid to avoid free-surface deformations (figure 7.1). To force the flow, two titanium electrodes (coated with Ir-MMO) are placed along two opposite sides of the tank, and three $28 \times 10 \times 1$ cm^3 rectangular permanent magnets are placed 1.1 cm underneath the tank bottom. The electrodes are placed in compartments which are connected to the measurement area of the tank by a
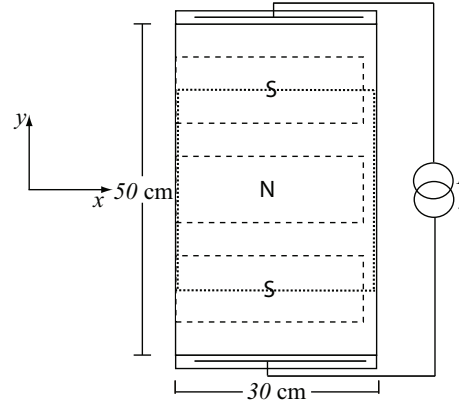
Figure 7.2 – *Top view of the experimental setup. The dashed lines represent the position of the three magnets, and the dotted lines represent the limits of the measurement area.*

system of thin horizontal slits through which the electric current easily passes. The system of slits isolates the chemical reaction products generated at the electrodes from the flow to be studied. As shown in figure 7.2, the magnet at the center has its North Pole facing up, while the two side magnets have their North Pole facing down. A constant electric current is applied through the fluid using a power supply with a precision of 10^{-2} A. Due to the interaction of the electric current and the magnetic field of the magnets, a Lorentz force,

$$\boldsymbol{F} = \boldsymbol{J} \times \boldsymbol{B}, \tag{7.1}$$

is generated (with $\boldsymbol{J}$ the current density and $\boldsymbol{B}$ the magnetic field), by which the fluid is set in motion.

We define a Cartesian coordinate system $\boldsymbol{x} = (x, y, z)$ with the origin at the center of the tank, x running parallel to the electrodes, y across the tank between the electrodes, and z in the vertical direction. Furthermore, we define the flow velocity $\boldsymbol{v} = (u, v, w)$.

We consider the electric current to be homogeneous and running only in the y-direction, while the main component of the magnetic field is in the z-direction. Hence, the principal component of the Lorentz force is in the x-direction.

To characterize the fluid, we consider two of its properties: the kinematic viscosity[ii] $\nu = 1.544 \cdot 10^{-6}$ m^{2}s^{-1} , and the density $\rho = 1190$ kg m^{-3}, which are kept constant for the experiments reported here.

We consider three characteristic length scales of the flow: the length of the tank in the x direction, $L_x = 30$ cm, the distance between the centers of the two lateral magnets, $L_y = 30$ cm, and the depth of the fluid H, which was varied for different experiments, taking the values $H = 1.2$, 2.0 or 3.2 cm.

[ii]The kinematic viscosity was measured for the solution used in the experiments at working temperature 21°C using a capillary viscometer 501 13 from Schott Instruments.

The magnitude of the Lorentz force is characterized by $[\boldsymbol{J} \times \boldsymbol{B}] = IB/(L_x H)$, where the brackets denote the order of magnitude, I is the magnitude of the electric current through the fluid, and $B = |\boldsymbol{B}|$ is the magnitude of the magnetic field at mid-depth above the center of each magnet.

Particle Image Velocimetry (PIV) was used to measure the horizontal velocity field of the flow in a plane at mid-depth. The fluid was seeded with 106–150 μm polymethylmethacrylate (PMMA) particles, which were illuminated at mid-depth with a double pulsed Nd:YAG laser sheet. Images of the central 30×30 cm^2 area of the tank (see figure 7.2) were taken, using a Megaplus ES 1.0 camera, at different time intervals (ranging from 10 ms to 1.3 s) depending on the maximum velocity in the flow. These images were then cross-correlated using PIV software from PIVTEC GmbH, Göttingen, Germany to calculate the horizontal velocity field.

To characterize the response of the flow, we focus on the velocity in the x-direction — in the direction of the principal component of the forcing — at $y = 0$. From now on, we refer to this velocity distribution as $\tilde{u}(x)$ which, as we shall see, corresponds to the velocity distribution along the symmetry axis of the dipolar structure at $y = 0$. Furthermore, we consider the mean value of this distribution

$$\langle \tilde{u}(x) \rangle \equiv \frac{1}{L_x} \int_{-L_x/2}^{L_x/2} \tilde{u}(x) \mathrm{d}x \tag{7.2}$$

as the characteristic velocity scale.

7.3 Dimensional analysis

Dimensional analysis shows that four independent dimensionless parameters can be defined for this flow problem. The geometry of the tank is represented by two aspect ratios:

$$\delta \equiv \frac{H}{L_x} \quad \text{and} \quad \delta_L \equiv \frac{L_x}{L_y}, \tag{7.3}$$

whereas the Chandrasekhar number

$$\mathrm{Ch} \equiv \frac{IBH}{\rho \nu^2} \tag{7.4}$$

characterizes the forcing and represents the ratio of the Lorentz force to the viscous force. Note that the definition of Ch introduced here is different from the one originally used by Chandrasekhar (1961). In the original definition, the current density $\boldsymbol{J}$ is considered to be primarily driven by $\boldsymbol{v} \times \boldsymbol{B}$ in Ohm's law, but in the present work, $\boldsymbol{J}$ is given by $\boldsymbol{J} = I/(L_x H)\hat{\boldsymbol{j}}$ (with $\hat{\boldsymbol{j}}$ the unit vector in the y-direction) since the induced effects can be neglected and the imposed Lorentz force dominates in electrolytes (Figueroa et al., 2009). This is not the case for other conductive fluids such as liquid metals (see e.g. Klein et al., 2009).

A similar definition for the ratio of Lorentz to viscous forces (7.4) is commonly referred to as *the Reynolds number based on the external force* (see e.g. Batchaev, 1990). However, in this study the term *Reynolds number* is reserved for the parameter characterizing the response of the flow, which is here defined as

$$\mathrm{Re} \equiv \frac{\langle \tilde{u} \rangle L_x}{\nu}, \tag{7.5}$$

with $\langle \tilde{u} \rangle$ the mean velocity, and which represents the ratio of inertia forces to viscous forces.

In the experiments, the aspect ratio δ was set by the depth of the fluid, yielding the values $\delta = 0.040$, 0.067 and 0.107. For each value of δ, the Chandrasekhar number Ch was varied by changing the magnitude of the electric current. The magnitude of the magnetic field at mid-depth above the center of each magnet B then takes the values $B = 0.018$, 0.017 and 0.015 T for the different values of δ, respectively. In the experiments described here, the horizontal aspect ratio $\delta_L = 1$ is kept constant.

We consider the flow to be governed by the Navier–Stokes equation including the Lorentz force

$$\rho \frac{\partial \boldsymbol{v}}{\partial t} + \rho (\boldsymbol{v} \cdot \boldsymbol{\nabla}) \boldsymbol{v} = -\boldsymbol{\nabla} p + \rho \nu \nabla^2 \boldsymbol{v} + \boldsymbol{J} \times \boldsymbol{B}, \tag{7.6}$$

where p is the pressure. From here on, the first term will be neglected since the flow attains a stationary state in the range of parameters studied.

To analyze the possible balances of forces in the flow, we consider the order of magnitude of each term in (7.6), where the pressure term is considered to be of the same order as the largest term in the equation. From this analysis, two different regimes are obtained.

7.3.1 Viscous regime

Due to the small depth, and hence, the predominance of friction at the bottom and the lid, we assume initially a Poiseuille-like vertical profile for the horizontal velocity field, i.e.

$$u(x, y, z) = u^*(x, y) \sin \left(\frac{\pi z}{H} \right), \tag{7.7}$$

where $\sin(\pi z / H)$ is the first term of the Fourier expansion of a Poiseuille profile. In this way, the order of magnitude of the viscous force is given by

$$[\rho \nu \nabla^2 \boldsymbol{v}] \approx \left[\rho \nu \frac{\partial^2 \boldsymbol{v}}{\partial z^2} \right] \sim \frac{\pi^2 \rho \nu \langle \tilde{u} \rangle}{H^2}, \tag{7.8}$$

considering that $\partial / \partial z \gg \partial / \partial x$.

The magnitude of the Lorentz force is given by

$$[\boldsymbol{J} \times \boldsymbol{B}] = \frac{IB}{L_x H}, \tag{7.9}$$

as mentioned before.

For relatively weak forcing and correspondingly small Reynolds numbers, inertia can be neglected, and the dominant balance is between the Lorentz and the viscous forces, i.e.

$$\frac{IB}{L_x H} \sim \frac{\pi^2 \rho \nu \langle \tilde{u} \rangle}{H^2}, \tag{7.10}$$

which is equivalent to

$$\mathrm{Re} \sim \frac{\mathrm{Ch}}{\pi^2}. \tag{7.11}$$

7.3.2   Advective regime

The order of magnitude of the advective term is given by

$$[\rho(\boldsymbol{v} \cdot \boldsymbol{\nabla})\boldsymbol{v}] \sim \frac{\rho \langle \tilde{u} \rangle^2}{L_x}, \tag{7.12}$$

where the velocity is considered to be of order $\langle \tilde{u} \rangle$, and L_x is taken as the characteristic length scale since advection takes place mainly in the horizontal plane.

For relatively strong forcing and correspondingly large Reynolds numbers, we may assume that the Lorentz force is of the same order as the inertia forces, so that

$$\frac{IB}{L_x H} \sim \frac{\rho \langle \tilde{u} \rangle^2}{L_x}, \tag{7.13}$$

which is equivalent to

$$\mathrm{Re} \sim \frac{\mathrm{Ch}^{1/2}}{\delta}. \tag{7.14}$$

In addition, we should recall that the flow is stationary, and hence, the input of energy due to the forcing has to be balanced by viscous dissipation. This means that the viscous forces in (7.6) must be also of the same order as the Lorentz forces, which cannot be achieved if the velocity has a Poiseuille-like vertical profile. That is, the presumption of (7.7) that the vertical gradient of the velocity is proportional to $\langle \tilde{u} \rangle / H$ is not valid in the advective regime. Hence, we assume that the velocity varies on a scale h such that

$$[\rho \nu \nabla^2 \boldsymbol{v}] \approx \left[\frac{\rho \nu}{h^2} \frac{\partial^2 \boldsymbol{v}}{\partial z'^2} \right] \sim \frac{\rho \nu \langle \tilde{u} \rangle}{h^2}, \tag{7.15}$$

where $h < H/\pi$. Finally, the balance of inertia and viscous forces yields the typical value

$$h \sim \frac{H}{\delta \mathrm{Re}^{1/2}} \tag{7.16}$$

for the vertical length scale h.

7.3.3 Transition between the viscous and advective regimes

The transition between the viscous regime and the advective regime is characterized by a change in the scaling of the Reynolds number as a function of the forcing. In this transition,

$$\mathrm{Re} \sim \frac{\mathrm{Ch}^{1/2}}{\delta} \sim \frac{\mathrm{Ch}}{\pi^2}, \tag{7.17}$$

which implies that the transition occurs when

$$\delta^2 \mathrm{Re} \sim \delta\, \mathrm{Ch}^{1/2} \sim \pi^2. \tag{7.18}$$

Note that, at this point, the critical value for the length scale h',

$$h \sim \frac{H}{\pi}, \tag{7.19}$$

can be obtained by comparing the magnitudes of the viscous forces in the advective and viscous regimes.

It is then convenient to define the normalized length scale

$$h^* = \frac{\pi h}{2}, \tag{7.20}$$

which can be regarded as the thickness of the boundary layers that form next to the bottom and the lid in the advective regime. This would imply that the transition occurs when the thickness of the boundary layer $\bar{h}$ is of the same order of half the total depth H, i.e. when

$$\frac{h^*}{H} \sim \frac{\pi}{2\mathrm{Re}^{1/2}\delta} \sim \frac{1}{2}, \tag{7.21}$$

and that in the advective regime, the thickness of the boundary layer h^* is smaller than half the total fluid depth.

7.4 Experimental results

Figure 7.3(a) shows characteristic flow lines tangential to the instantaneous horizontal velocity components in the measurement plane for $\mathrm{Ch} = 1.3 \cdot 10^3$ and
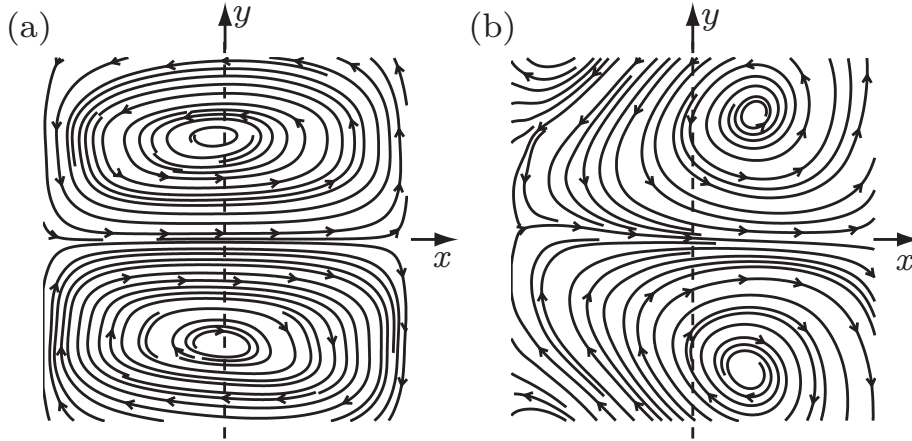
Figure 7.3 – *Flow lines tangential to the horizontal velocity components at mid-depth in the central 30×30 cm^2 region of the tank for (a) Ch $= 1.3 \cdot 10^3$, (b) Ch $= 8.8 \cdot 10^5$, and $\delta = 0.067$. The dashed line represents the line $x = 0$.*

$\delta = 0.067$. As can be seen, the forcing generates a dipolar structure with a symmetry axis $y = 0$. Apparently, for this value of Ch, the dipole is also nearly symmetric with respect to the line $x = 0$.

Figure 7.3(b) shows the flow lines for Ch $= 8.8 \cdot 10^5$, with the other parameters unchanged. A clear difference is observed between the flow lines in Fig. 7.3 (a) and figure 7.3(b). In particular, the flow lines for strong forcing spiral out of the vortex cores, in contrast with the quasi-closed flow lines for weak forcing. This suggests that there is a strong horizontal divergence for large Ch values. This divergence is due to pumping of fluid from the Bödewadt boundary layers at the bottom and at the lid to the inside of the vortex cores (Bödewadt, 1940). In addition, there is a strong asymmetry with respect to the line $x = 0$ for Ch $= 8.8 \cdot 10^5$. This asymmetry can be seen, for example, in the positions of the centers of the two cells which are no longer close to $x = 0$, but displaced in the positive x-direction.

To quantify some of the differences in the flow at different values of the forcing, we focus on $\tilde{u}(x)$, the velocity distribution along the symmetry axis of the dipolar structure at $y = 0$. Figure 7.4 shows the velocity distributions $\tilde{u}(x)$ for different values of Ch and $\delta = 0.04$. It can be seen that the magnitude of $\tilde{u}$ increases with increasing Ch-value, and that the asymmetry in this velocity distribution with respect to $x = 0$ becomes more pronounced for large Ch-values.

Measured values of the Reynolds number Re, based on (7.5), are plotted in figure 7.5 as a function of the Chandrasekhar number Ch for three different values of the aspect ratio δ. The axes have been rescaled with δ^2, and as can be seen, the curves for the different values of δ collapse. Furthermore, the experimental results are compared with the theoretical predictions Re $\sim$ Ch$/\pi^2$ and Re $\sim \delta^{-1}$Ch$^{1/2}$. The graph clearly shows the existence of the two characteristic scaling regimes:
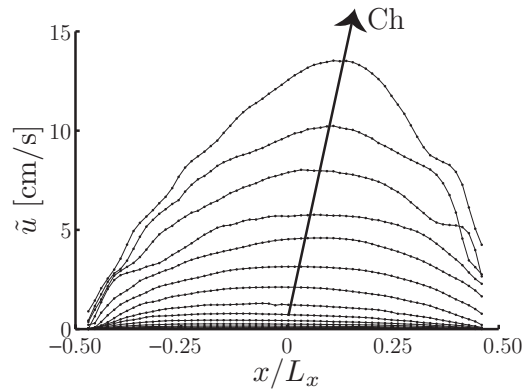
Figure 7.4 – *Measured velocity distributions $\tilde{u}(x/L_x)$ at $y = 0$ for different Ch-values, and $\delta = 0.04$.*
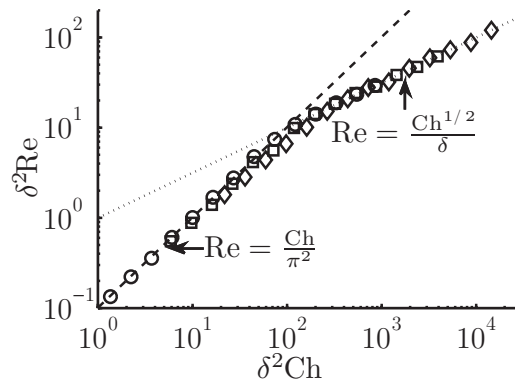
Figure 7.5 – *Magnitude of the response of the flow as a function of the forcing. Measured values of $\delta^2 \text{Re}$ as a function of the parameter $\delta^2 \text{Ch}$ for various values of Ch, and $\delta = 0.040$ ($\circ$), $\delta = 0.067$ ($\square$), $\delta = 0.107$ ($\diamond$). The dashed line represents $\text{Re} = \text{Ch}/\pi^2$ (viscous regime) and the dotted line represents $\text{Re} = \delta^{-1} \text{Ch}^{1/2}$ (advective regime). The intersection of the dashed and dotted lines represents the transition point $\delta^2 \text{Re} = \delta \, \text{Ch}^{1/2} = \pi^2$.*
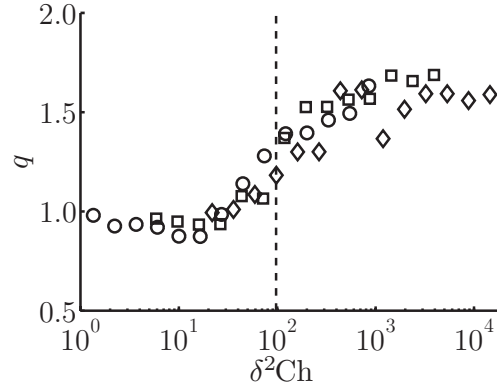
Figure 7.6 – *Measured asymmetry parameter q as a function of the input parameter $\delta^2\mathrm{Ch}$, for $\delta = 0.04$ ($\circ$), $\delta = 0.067$ ($\square$), $\delta = 0.107$ ($\diamond$). The dashed line represents the transition value $\mathrm{Ch}\delta^2 = \pi^4$.*

(i) $\mathrm{Re} \sim \mathrm{Ch}/\pi^2$ for $\delta\,\mathrm{Ch}^{1/2} < \pi^2$ and $\delta^2\mathrm{Re} < \pi^2$, where the inertia forces can be neglected, and (ii) $\mathrm{Re} \sim \delta^{-1}\mathrm{Ch}^{1/2}$ for $\delta\mathrm{Ch}^{1/2} = \delta^2\mathrm{Re} > \pi^2$, where the Lorentz and the inertia forces are of the same order. Furthermore, a rather sharp transition is observed at $\delta^2\mathrm{Re} \sim \delta\,\mathrm{Ch}^{1/2} \sim \pi^2$.

The collapse of the curves in figure 7.5 for different δ values indicates that the only two relevant parameters of the problem are: $\delta^2\mathrm{Ch}$, as the input parameter, and $\delta^2\mathrm{Re}$, as the response parameter. Note that $\delta^2\mathrm{Re}$ is inversely proportional to the square of the boundary layer thickness h^* defined in (7.20). This suggests that the dynamics of the flow are governed by the boundary layer dynamics. In a recent study of decaying shallow swirl flows (Duran-Matute et al., 2010), it was shown that such flows are also characterized by the nondimensional parameter $\delta^2\mathrm{Re}$.

It can also be observed in figure 7.5 that for the deepest layer ($\delta = 0.107$), there is a larger deviation with respect to the curve $\mathrm{Re} = \mathrm{Ch}/\pi^2$ as compared to the results from experiments with shallower layers. This deviation can be explained by the larger importance of horizontal viscous diffusion compared to the vertical viscous diffusion as the depth of the layer is increased.

The existence of the two scaling regimes is a very robust characteristic of the flow studied in the present chapter: the same scaling was found when considering additional velocity data at other locations instead of only the velocity along the symmetry axis of the dipole at $y = 0$.

To quantify the asymmetry in the flow, we define the ratio of the Reynolds number Re^+ characterizing the flow at $x > 0$ and the Reynolds number Re^- for

$x < 0$:

$$q \equiv \frac{\mathrm{Re}^+}{\mathrm{Re}^-} = \frac{\displaystyle\int_0^{L_x/2} \tilde{u}(x)\mathrm{d}x}{\displaystyle\int_{-L_x/2}^0 \tilde{u}(x)\mathrm{d}x}, \tag{7.22}$$

which is plotted in figure 7.6 as a function of $\delta^2 \mathrm{Ch}$ for $\delta = 0.04,\ 0.067$, and 0.0107. A reasonably good collapse of the experimental data for the three values of δ is observed, supporting the previous result that the flow only depends on the values of $\delta^2 \mathrm{Ch}$. For $\delta^2 \mathrm{Ch} \lesssim 30$, the asymmetry parameter $q \approx 1$. This suggests that the flow is almost symmetric with respect to $x = 0$. As the value of Ch increases, q sharply increases until $\mathrm{Ch} \approx 10^3$. For $\mathrm{Ch} \gtrsim 10^3$, the asymmetry in the flow remains almost constant with $q \approx 1.7$. This saturation of q is probably due to the presence of the lateral boundary at $x = L_x/2$ since $\tilde{u}(L_x/2) = 0$, and hence, the maximum of $\tilde{u}(x)$ must remain at a finite distance away from this boundary.

Note that the transition between $q \approx 1$ and $q \approx 1.7$ corresponds to the change in scaling between the viscous and the advective regimes shown in figure 7.5. Hence, it can be concluded that the increase in asymmetry is due to advection.

7.5 Implications for previous and future work

Shallow flows are generally modeled with the quasi-two-dimensional (Q2D) Navier–Stokes equation (Dolzhanskii et al., 1992):

$$\frac{\partial \boldsymbol{v}_{\mathrm{H}}}{\partial t} + (\boldsymbol{v}_{\mathrm{H}} \cdot \boldsymbol{\nabla}_{\mathrm{H}})\boldsymbol{v}_{\mathrm{H}} = -\frac{1}{\rho}\boldsymbol{\nabla}_{\mathrm{H}}p + \lambda\boldsymbol{v}_{\mathrm{H}} + \frac{\boldsymbol{F}}{\rho}, \tag{7.23}$$

and the continuity equation

$$\boldsymbol{\nabla}_{\mathrm{H}} \cdot \boldsymbol{v}_{\mathrm{H}} = 0 \tag{7.24}$$

where

$$\boldsymbol{\nabla}_{\mathrm{H}} \equiv \left(\frac{\partial}{\partial x}, \frac{\partial}{\partial y} \right);$$

$\boldsymbol{v}_{\mathrm{H}} = (u, v)$ is the horizontal velocity; $\boldsymbol{F}$ is an external body force, and λ is a constant known as the *external friction parameter* or the *Rayleigh friction parameter*. Over the years, many different expressions have been suggested for the friction parameter: $\lambda = 2\nu/H^2$ (Dolzhanskii et al., 1990), $\lambda = \pi^2\nu/(4H^2)$(Hansen et al., 1998; Duran-Matute et al., 2010), or $\lambda = 2\kappa\nu/H^2$ where κ is a fitting parameter that depends on the velocity field (Bodarenko et al., 1979; Dolzhanskii et al., 1992; Danilov & Dovzhensko, 1996). In these cases, H is the total depth of the fluid between a solid bottom and a free surface, instead of between a solid bottom

and a solid lid, as considered in the current paper. In general, a good agreement has been found between theory and experiments. These observations have lead to believe that the use of a linear damping term to parametrize the effect of bottom friction in shallow flows is well supported.

However, in the current chapter, we have found the well-defined limit $\delta^2 \text{Ch} = \pi^4$ for the use of (7.23) and (7.24) to model electromagnetically forced shallow flows. Above this limit, the damping rate due to bottom friction depends on the thickness of the boundary layer which, in turn, depends on the magnitude and distribution of the horizontal flow velocity.

In previous experiments on electromagnetically shallow flows, only the linear relationship between the forcing and the velocity has been reported, even though small deviations for strong forcing were also observed (see e.g. Tabeling et al., 1987). This implies that these experiments where performed mostly within the viscous regime, thus supporting previous experimental results.

Due to the success of (7.23) and (7.24) in describing shallow flows, this system of equations has been solved numerically to model an electromagnetically forced array of vortices in a shallow layer of electrolyte (Nakamura, 1996). In these simulations, the magnitude of the forcing was varied while λ was kept constant. For small forcing magnitudes, a good agreement with laboratory experiments was obtained, and a threshold equivalent to $\delta^2 \text{Ch} = \pi^4$ at which the vortices changed shape was observed. However, for stronger forcing magnitudes the numerical simulations started to differ significantly from the experimental data. This discrepancy can be easily explained since above the threshold $\delta^2 \text{Ch} = \pi^4$ the damping rate depends on the forcing, and λ is no longer a constant.

In addition, for $\delta^2 \text{Ch} > \pi^4$, the flow lines tangential to the horizontal velocity describe spirals originating at the vortex cores. This shape suggests a strong horizontal divergence, in disagreement with (7.24). In fact, it is for this type of flows with curvilinear flow lines tangential to the horizontal velocity vectors and an additional secondary motion that Ponomarev et al. (2009) proposed that $\text{Re} \propto \text{Ch}^{2/3}$. However, in our experiments, a clear regime with this scaling was not observed.

7.6 Conclusions

We studied experimentally the response of a generic electromagnetically forced flow. This response was quantified by measuring the Reynolds number Re as a function of the Chandrasekhar number Ch (the ratio of Lorentz forces to viscous forces). We found two scaling regimes: $\text{Re} \sim \text{Ch}/\pi^2$ (viscous regime) and $\text{Re} \sim \delta^{-1}\text{Ch}^{1/2}$ (advective regime), with a transition at $\delta^2\text{Re} \sim \delta\,\text{Ch}^{1/2}\delta \sim \pi^2$. This scaling is in good agreement with our theoretical predictions.

The transition between the two regimes is related to a qualitative change of the vertical velocity profile: from a Poiseuille-like profile in the viscous regime to a profile composed, in the advective regime, of an inviscid interior and two boundary layers, one at the bottom and one at the lid, each with a thickness

$h^* = \pi H / (2\delta\,\mathrm{Re}^{1/2})$. This transition marks the upper limit for the magnitudes of the forcing and the velocity where the Q2D Navier–Stokes equation (7.23) and the 2D continuity equation (7.24) can be used to model shallow flows.

Furthermore, it was found that the flow evolution is characterized by a single parameter, $\delta^2\mathrm{Re}$. Such a conclusion had already been reached by Dolzhanskiy (1987) for the viscous regime where the flow is described by (7.23) and (7.24). However, it has been shown in the current chapter that this dependence extends to the advective regime.

In the particular case of the dipolar structure studied here, nonlinear effects are reflected in the form of an asymmetry due to the self-advection of the two vortices composing the dipole, as it had been previously observed (Figueroa et al., 2009; Danilov & Dovzhenko, 1996). These nonlinear effects, in the form of vortex-vortex interactions, can be already observed for $\delta^2\mathrm{Ch} \gtrsim 30$ as inertia forces become increasingly important, and are predominant in the advective regime when $\mathrm{Re} \sim \delta^{-1}\mathrm{Ch}^{1/2}$, i.e. for $\delta^2\mathrm{Ch} > \pi^4$.

The current chapter presents new insight into the structure and dynamics of electromagnetically forced shallow flows in a shallow layer of electrolyte. The results presented can serve as a guideline for future experimental and numerical work on, for example, shallow flows, quasi-two-dimensional turbulence, or the stability of quasi-two-dimensional spatially periodic flows. Another interesting line for future research is the study of the response of the flow to the electromagnetic forcing in other conductive fluids such as liquid metals, which are of interest in metallurgical processing applications.

Chapter 8

Stationary dipolar structure with background rotation

8.1 Introduction

In attempts to obtain quasi-two-dimensional (Q2D) flows in the laboratory in order to study two-dimensional (2D) turbulence, experimentalists have recurred to background rotation (Afanasyev & Wells, 2005; Tenreiro et al., 2010) although less frequently than to shallow fluid layers. Strong enough background rotation tends to reduce the vertical gradients in the direction of the axis of rotation and the flow organizes in columnar structures (Hopfinger, 1982). However, Ekman boundary layers, which form next to the boundaries perpendicular to the axis of rotation, drive a vertical motion through what is called *Ekman pumping* (see Pedlosky, 1987). If linear Ekman theory holds, the vertical motion can be parametrized with a linear damping term in the 2D vorticity equation, so that the evolution of a freely evolving flow on a cross-section perpendicular to the axis of rotation can be modeled by

$$\frac{\mathrm{D}\omega_n}{\mathrm{D}t} = -\lambda_{\mathrm{Ek}}\omega_n, \tag{8.1}$$

where ω_n is the vorticity component parallel to the axis of rotation of the system, and $\lambda_{\mathrm{Ek}} = (\Omega\nu)^{1/2}/H$ is known as Ekman friction with Ω the rotation rate of the system, ν the kinematic viscosity, and H the depth of the fluid.

It is commonly assumed that (8.1) holds if the Rossby number Ro — which represents a ratio of the convective acceleration to the Coriolis acceleration — is small compared to unity.

Ekman boundary layer theory rests on the balance of viscous forces and the Coriolis force within the boundary layer. This theory is only valid a priori for flows that are not subjected to an additional non-conservative external body force,

113

such as (EM) electromagnetic forces, since this could disrupt the balance of forces necessary for Ekman theory to hold. Although time-independent electromagnetic forcing has been recently used to drive flows subjected to background rotation in hopes of obtaining Q2D flows (Afanasyev & Jewtoukoff, 2009), it has not yet been determined under which conditions it is possible to use a linear damping term as in (8.1), and hence, if such a flow can indeed be considered as Q2D.

It is the goal of this chapter to characterize the response of a flow with background rotation to the strength of an external body force perpendicular to the axis of rotation. In particular, we aim to determine if Ekman theory holds for such a flow, and if so, to obtain the limits of applicability.

To achieve these goals, we study experimentally and numerically a confined dipolar flow structure driven by time-independent electromagnetic forcing in a shallow layer of salt solution subjected to background rotation. In particular, we characterize the response of the flow by measuring the Reynolds number Re as a function of the Chandrasekhar number Ch (quantifying the ratio of Lorentz to viscous forces) and the Ekman number Ek (quantifying the ratio of viscous forces to the Coriolis force).

This chapter is organized as follows: Section 8.2 presents the experimental and numerical methods. In Section 8.3, we define the nondimensional parameters pertinent to the problem. Section 8.4 is devoted to the main results of this chapter, and finally, a discussion of the results and some conclusions are given in Section 8.5.

8.2   Methods

8.2.1   Experimental setup

The experimental setup is similar to the one described in the previous chapter and consists of a water tank with a base of 34×30 cm^2 which, in this case, is placed on top of a rotating table, which rotates at a frequency Ω. The tank is filled with a salt solution with a concentration of 178 g l^{-1} with a kinematic viscosity [i] $\nu = 1.50 \cdot 10^{-6}$ m^{2}s^{-1} and a density $\rho = 1190$ kg m^{-3} to a depth H and covered with a transparent perspex lid to avoid free-surface deformations [figure 7.1(a)]. To force the flow, two titanium electrodes are placed along two opposite sides of the tank, and three 30×10 cm^2 rectangular magnets are placed 1.1 cm underneath the tank bottom. The magnitude of the magnetic field of each these magnets is 0.018 T measured just above their center. As shown in figure 7.2, the magnet at the center has its North Pole facing up, while the two side magnets have their North Pole facing down. A constant electric current I is applied through the fluid using a power supply with a precision of 10^{-2} A.

We define a Cartesian coordinate system $\boldsymbol{x} = (x, y, z)$ with the origin at the

---

[i]The kinematic viscosity was measured for the solution used in the experiments at the temperature of the experiments 21°C using a capillary viscometer 501 13 from Schott Instruments.
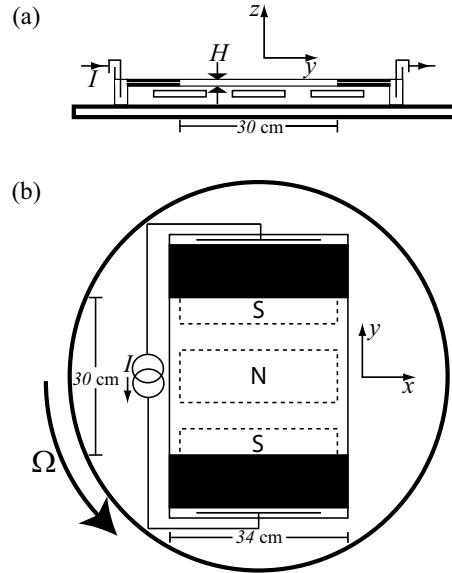
Figure 8.1 – *Schematic representation of the experimental setup. (a) Vertical cross-section of the experimental setup. (b) Upper view of the experimental setup.*

center of the tank, x running parallel to the electrodes, y across the tank between the electrodes, and z in the vertical direction. Furthermore, we define the flow velocity $\boldsymbol{v} = (u, v, w)$.

We consider the electric current to be homogeneous and running only in the y-direction, while the main component of the magnetic field is in the z-direction. Hence, the principal component of the Lorentz force is in the x-direction.

We consider three characteristic length scales of the flow: the length of the tank in the x-direction, $L_x = 34$ cm, and in the y-direction, $L_y = 30$ cm, and the depth of the fluid H, which was varied for different experiments taking the values $H = 1.2$ cm and 2.0 cm.

Particle Image Velocimetry (PIV) is used to measure the horizontal velocity field of the flow in a plane at mid-depth. The fluid is seeded with 106–150 μm polymethylmethacrylate (PMMA) particles, which are illuminated at mid-depth with a laser sheet produced by a double pulsed Nd:YAG laser. Both the laser and a Megaplus ES 1.0 camera are mounted on the rotating table. Images of the central 34×28 cm^2 area of the tank are taken, using the camera, at different time intervals (ranging from 10 ms to 1.3 s) depending on the maximum velocity in the flow. These images are then cross-correlated using PIV software from PIVTEC GmbH, Göttingen, Germany to calculate the horizontal velocity field.

Figure 8.2 – *Analytically obtained distribution of the vertical component of the magnetic field B_z. The grayscale denotes the magnitude of B_z (in Tesla) 0.6 cm above the bottom.*

8.2.2 Numerical simulations

Numerical simulations of the flow were performed to obtain the three-dimensional (3D) velocity field and results for parameters outside the possible range of parameters achievable in the laboratory.
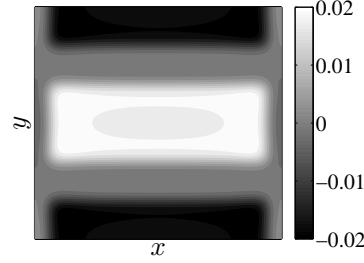
We consider the flow to be governed by the Navier–Stokes equations that include both the Coriolis force and the Lorentz force:

$$\frac{\partial \boldsymbol{v}}{\partial t} + \boldsymbol{v} \cdot \boldsymbol{\nabla}\boldsymbol{v} + 2\boldsymbol{\Omega} \times \boldsymbol{v} = \frac{1}{\rho}\boldsymbol{\nabla}P + \nu\nabla^2\boldsymbol{v} + \frac{1}{\rho}\boldsymbol{J} \times \boldsymbol{B}, \tag{8.2}$$

and the continuity equation for an incompressible fluid:

$$\boldsymbol{\nabla} \cdot \boldsymbol{v} = 0, \tag{8.3}$$

where $\boldsymbol{\Omega} = \Omega\hat{\boldsymbol{k}}$ is the rotation vector of the system; P is the reduced pressure; $\boldsymbol{B} = (B_x, B_y, B_z)$ is the magnetic field; and $\boldsymbol{J} = I/(L_xH)\hat{\boldsymbol{j}}$ is the current density, where $\hat{\boldsymbol{j}}$ is the unit vector in the y-direction.

Equations (8.2) and (8.3) were solved using a finite element code COMSOL (COMSOL AB, 2008), where the electromagnetic forcing was introduced using an analytical model for the vertical magnetic field, as described in Appendix D. Figure 8.2, shows the calculated distribution of the vertical component of the magnetic field 0.6 cm above the bottom of the tank. In this figure, the three magnets are clearly distinguishable.

The numerical domain simulates the experimental tank and is discretized using an unstructured mesh with triangular elements in the horizontal and a structured mesh with ten layers in the vertical direction. The equations were solved for approximately 350 000 degrees of freedom. Both the spatial and temporal resolution were checked by increasing them until the solution converged.

8.3 Nondimensional parameters

Dimensional analysis yields three independent dimensionless parameters as the control parameters of the problem. Here we consider the Chandrasekhar number

$$\mathrm{Ch} \equiv \frac{IBH}{\rho\nu^2}, \tag{8.4}$$

which characterizes the EM forcing and represents the ratio of the Lorentz force to the viscous force; the Ekman number

$$\mathrm{Ek} \equiv \frac{\nu}{\Omega H^2}, \tag{8.5}$$

which characterizes the system's rotation rate and represents the ratio of viscous forces to the Coriolis force; and the aspect ratio

$$\delta \equiv \frac{H}{L_x}, \tag{8.6}$$

which characterizes the geometry of the container. The horizontal dimensions of the container remain unchanged for all experiments.

In addition, as the response parameter of the problem, we define the Reynolds number

$$\mathrm{Re} \equiv \frac{UL_x}{\nu}, \tag{8.7}$$

which represents the ratio of inertia forces to viscous forces, with U a typical velocity scale of the flow. In other words,

$$\mathrm{Re} = \mathrm{Re}(\mathrm{Ch}, \mathrm{Ek}, \delta). \tag{8.8}$$

To characterize the velocity of the flow, we measured the horizontal velocity components $\boldsymbol{v}_{\mathrm{H}} = (u, v)$ at mid-depth $z = H/2$. Furthermore, we consider the time averaged value for the velocity (denoted $\bar{\boldsymbol{v}}_{\mathrm{H}}$) after a steady state is reached. The time average was computed with $100 < N < 1000$ image pairs, depending on the experiment. It was checked that the number of image pairs was large enough so that the value of Re did not vary anymore if the number of image pairs was further increased.

We consider the typical velocity scale U to be the spatial average of the horizontal velocity at mid-depth:

$$U = \langle |\bar{\boldsymbol{v}}_{\mathrm{H}}(x, y, H/2)| \rangle = \frac{1}{L_x L_y} \int_{-L_y/2}^{L_y/2} \int_{-L_x/2}^{L_x/2} |\bar{\boldsymbol{v}}_{\mathrm{H}}(x, y, z = H/2)| \mathrm{d}x \mathrm{d}y, \tag{8.9}$$

where $|...|$ denotes the magnitude of the vector. The average value of the velocity is not based solely on the magnitude of the velocity along the symmetry axis $y = 0$,
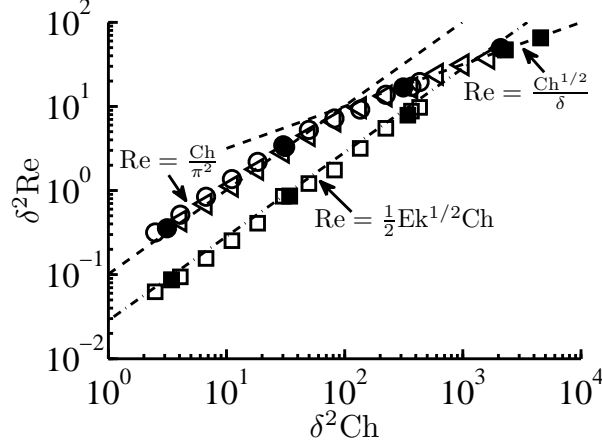
Figure 8.3 – *Response of the flow as a function of the forcing magnitude. Values of the Reynolds number* Re *as a function of the Chandrasekhar number* Ch *(the axes have been scaled with δ^2). Experimental results for* Ek $= \infty$ *and* $\delta = 0.035$ *(○), Ek $= \infty$ and* $\delta = 0.059$ *(◁), and for* Ek $= 3.5 \cdot 10^{-3}$ *and* $\delta = 0.035$ *(□). The filled symbols denote corresponding numerical results. The dashed lines denote the analytical estimation for the value of* Re *for* Ek $= \infty$ *according to (8.11) or (8.12). The dashed-dotted line represents the analytical estimation for the case of* Ek $= 3.5 \cdot 10^{-3}$ *according to (8.16).*

as in the previous chapter, since the symmetry with respect to such axis is broken for flows subjected to background rotation.

Since in the current chapter we consider the average magnitude of the horizontal velocity to compute the Reynolds number, it is then appropriate to consider the characteristic magnitude of the magnetic field B as the spatial average of the absolute value of B_z at mid-depth.

Note that the Rossby number Ro, commonly used to characterize flows subjected to background rotation, can be recovered from the nondimensional parameters previously defined:

$$\mathrm{Ro} \equiv \frac{1}{2}\delta^2 \mathrm{Ek}\,\mathrm{Re} = \frac{U}{\Omega L}. \tag{8.10}$$

8.4   Results

Figure 8.3 shows the measured values of the parameter $\delta^2 \mathrm{Re}$ as a function of the control parameter $\delta^2 \mathrm{Ch}$ for the case of no rotation (Ek $= \infty$) and two values of the aspect ratio: $\delta = 0.035$ and $\delta = 0.059$. In agreement with the results from the previous chapter, we observe two scaling regimes:

$$\mathrm{Re} \sim \frac{\mathrm{Ch}}{\pi^2} \tag{8.11}$$

for $\delta^2\mathrm{Ch} \lesssim \pi^4$, and

$$\mathrm{Re} \sim \frac{\mathrm{Ch}^{1/2}}{\delta} \tag{8.12}$$

for $\delta^2\mathrm{Ch} \gtrsim \pi^4$. The transition between the two regimes at

$$\delta^2\mathrm{Re} \sim \delta\,\mathrm{Ch}^{1/2} \sim \pi^2 \tag{8.13}$$

is easily distinguishable by the intersection of (8.11) and (8.12). As in the previous chapter, it can be clearly seen that the response of the flow is given only by the product $\delta^2\mathrm{Re}$, which depends exclusively on the control parameter $\delta^2\mathrm{Ch}$ for the case of no background rotation. Furthermore, a good agreement is observed between the numerical results, the experimental results, and the theoretical predictions.

Figure 8.3 also shows the measured values of $\delta^2\mathrm{Re}$ as a function of $\delta^2\mathrm{Ch}$ for simulations and experiments with $\mathrm{Ek} = 3.5 \cdot 10^{-3}$ (strong background rotation) and $\delta = 0.035$. For the case of small Ek-values, it is usually assumed that the damping of the system is due to Ekman friction (Dolzhanskii et al., 1992). This implies that the order of magnitude of the viscous terms is

$$[\nu\nabla^2\boldsymbol{v}] \sim 2\mathrm{Ek}^{1/2}\Omega\boldsymbol{v} \tag{8.14}$$

when considering two Ekman boundary layers: one at the bottom and one at the lid.

If the convective acceleration is neglected, a balance between the Lorentz force and Ekman friction yields

$$\frac{IB}{\rho HL} \sim 2\mathrm{Ek}^{1/2}\Omega\langle|\bar{\boldsymbol{v}}_{\mathrm{H}}(x,y,H/2)|\rangle, \tag{8.15}$$

which is equivalent to

$$\mathrm{Re} \sim \frac{1}{2}\mathrm{Ek}^{1/2}\mathrm{Ch}. \tag{8.16}$$

In this case, the Reynolds number increases linearly with the magnitude of the forcing, as for small Ch-values in the case of no background rotation. Within this linear dependence of the forcing, the damping rate increases by adding rotation, i.e. the value of the Reynolds number is smaller for the same Ch-value when the flow is subjected to strong background rotation.

From a comparison with the non-rotating case, it would be expected that as the convective acceleration becomes dominant over the Coriolis force, the response of the flow will again obey (8.12), yielding a transition at

$$\delta^2\mathrm{Re} \sim \delta\,\mathrm{Ch}^{1/2} \sim \frac{2}{\mathrm{Ek}^{1/2}}. \tag{8.17}$$

Figure 8.4 – *Measured values of the Reynolds number* Re *as a function of the Ekman number* Ek *for experiments with* $\delta = 0.35$ *and* $\text{Ch} = 2 \cdot 10^5$. *The dashed lines represent* $\text{Re} = \text{Ek}^{1/2}\text{Ch}/2$ *and* $\text{Re} = \delta^{-1}\text{Ch}^{1/2}$.

This transition suggests that the linear behavior will hold for larger Ch-values when the flow is subjected to background rotation, and hence, that higher Reynolds number can be reached where the linear dependence $\text{Re} \propto \text{Ch}$ still holds.

The results from numerical simulations support the existence of the transition when $\delta\,\text{Ch}^{1/2} \sim 2\text{Ek}^{-1/2}$, as seen in figure 8.3 where the data points for $\delta^2\text{Ch} = 2300$ and $\delta^2\text{Ch} = 4600$ lie on the line given by (8.12). However, it was not possible to perform experiments with $\text{Ek} = 3.5 \cdot 10^{-3}$ for $\delta^2\text{Ch} \gtrsim 450$ due to practical limitations. Instead, experiments with strong forcing ($\text{Ch} = 2 \cdot 10^5$, $\delta^2\text{Ch} = 245$) were performed at different rotation rates to experimentally validate the existence of the transition (8.17).
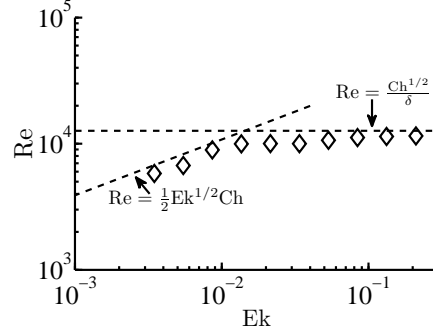
Figure 8.4 shows the measured values of the Reynolds number Re as a function of the Ekman number Ek for experiments with $\text{Ch} = 2 \cdot 10^5$ and $\delta = 0.035$. As can be seen, for $\text{Ek} \gtrsim 4\delta^{-2}\text{Ch}^{-1} = 0.016$ the Reynolds number varies little with the Ekman number and $\text{Re} \sim \delta^{-1}\text{Ch}^{1/2}$. On the other hand, $\text{Re} \sim \text{Ek}^{1/2}\text{Ch}/2$ for $\text{Ek} \lesssim 4\delta^{-2}\text{Ch}^{-1} = 0.016$, indicating that the damping is due to Ekman friction in this region of the parameter space.

The transition from the advection dominated regime towards the Ekman damping dominated regime, as given by (8.17), is clearly visible in figure 8.4. Writing (8.17) in terms of the control parameters of the problem yields

$$\frac{\delta^2\,\text{Ch}\,\text{Ek}}{4} \sim 1. \tag{8.18}$$

Writing (8.17) in terms of the Rossby number yields

$$\frac{\text{Ro}}{\text{Ek}^{1/2}} \sim 1, \tag{8.19}$$

indicating that this transition does not depend exclusively on the Rossby number. Instead, the product Ch Ek represents the ratio of the Lorentz force to the Coriolis force. This suggests that the transition depends on the ratio of these forces.
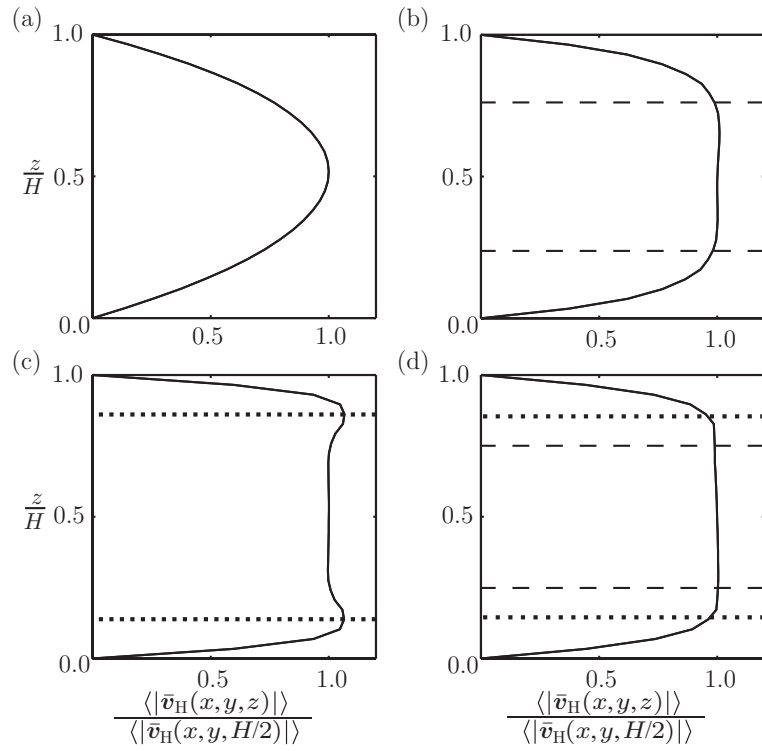
Figure 8.5 – *Numerically obtained vertical profiles of the horizontal velocity. The solid lines represent the horizontally averaged vertical profiles of the horizontal velocity for four simulations with $\delta = 0.035$: (a) $\mathrm{Ek} = \infty$, and $\mathrm{Ch} = 2.14 \cdot 10^4$; (b) $\mathrm{Ek} = \infty$, and $\mathrm{Ch} = 1.14 \cdot 10^6$; (c) $\mathrm{Ek} = 3.5 \cdot 10^{-3}$, and $\mathrm{Ch} = 2.14 \cdot 10^4$; and (d) $\mathrm{Ek} = 3.5 \cdot 10^{-3}$, and $\mathrm{Ch} = 1.14 \cdot 10^6$. The dashed lines denote the normalized thickness of the boundary layers: h_{Re}^* (dashed line), and h_{Ek}^* in (dotted line).*

To understand further the physical mechanism behind the transition, it is convenient to study the vertical profile of the horizontal velocity for different values of the problem parameters. Figure 8.5 shows the numerically obtained vertical velocity profiles for four characteristic simulations with $\delta = 0.035$: (a) Ek $= \infty$ and Ch $= 2.14 \cdot 10^4$; (b) Ek $= \infty$ and Ch $= 1.14 \cdot 10^6$ (within the large Ch-value regime); (c) Ek $= 3.5 \cdot 10^{-3}$ and Ch $= 2.14 \cdot 10^4$; and (d) Ek $= 3.5 \cdot 10^{-3}$ and Ch $= 1.14 \cdot 10^6$. It can be observed that for no background rotation and small Ch-values, the flow has a Poiseuille-like vertical profile [figure 8.5(a)]. On the other hand, the vertical profile consists of an inviscid interior and two boundary layers — one at the bottom and one at the lid — for large Ch-values and no background rotation [figure 8.5(b)]. As in the previous chapter, the dimensionless thickness of these boundary layers is defined as

$$h_{\mathrm{Re}}^* = \frac{\pi}{2\delta\,\mathrm{Re}^{1/2}}. \tag{8.20}$$

In this way, the transition between the viscosity dominated regime and the advective regime occurs when $h_{\mathrm{Re}}^* \sim 1/2$. In figure 8.5(b), it can be observed that h_{Re}^* is a good estimate for the actual boundary layer thickness.

For weak forcing and strong background rotation, the vertical profile tends towards a profile with an inviscid geostrophic interior, where the velocity is independent of the vertical coordinate, and two Ekman boundary layers [figure 8.5(c)]. Similarly to the case of no background rotation, a characteristic dimensionless boundary layer thickness can be defined as

$$h_{\mathrm{Ek}}^* = \frac{\pi^2}{4}h_{\mathrm{Ek}} = \frac{\pi^2}{4}\mathrm{Ek}^{1/2} \tag{8.21}$$

where $h_{\mathrm{Ek}} = \mathrm{Ek}^{1/2}$ is usually referred to as the *(nondimensional) Ekman boundary layer thickness*. Here, $h_{\mathrm{Ek}}^* \sim 1/2$ marks the transition between a viscosity dominated flow with a Poiseuille-like vertical profile to the Coriolis dominated flow, i.e. if $h_{\mathrm{Ek}}^* > 1/2$ and $\delta^2\mathrm{Ch} < \pi^4$, the flow will have a Poiseuille-like profile as in figure 8.5(a). In figure, 8.5(c) it can be seen that h_{Ek}^* gives a good estimate for the thickness of the boundary layers. Moreover, note two local maxima for the horizontal velocity at $z/H \approx h_{\mathrm{Ek}}^*$, which are characteristic of Ekman boundary layers and are related to the Ekman spiral.

As the magnitude of the forcing is increased in the case of strong rotation, the vertical profile is again deformed for values of $\delta^2\mathrm{Ch} \gtrsim 4\mathrm{Ek}^{-1}$. In particular, note in figure 8.5(d) that the characteristic shape of the Ekman boundary layers is lost; that h_{Ek}^* is no longer a good estimate for the boundary layer thickness; and that the vertical profile starts to resemble more the profile in the advective dominated regime [figure 8.5(b)].

8.5   Discussion and conclusions

In the current chapter, we studied the effect of background rotation on the response of a generic shallow flow to electromagnetic forcing. The response was quantified by measuring the Reynolds number Re as a function of both the Chandrasekhar number Ch (which characterizes the strength of the electromagnetic forcing) and the Ekman number Ek (which characterizes the strength of the Coriolis force). It was found that for small Ekman numbers and weak forcing, the flow responds in agreement with linear Ekman theory, so that $\mathrm{Re} \sim \mathrm{Ek}^{1/2}\mathrm{Ch}/2$. As the forcing strength is increased, while keeping the other parameters fixed, the response of the flow becomes nonlinear, so that $\mathrm{Re} \sim \delta^{-1}\mathrm{Ch}^{1/2}$. The transition between the two regimes is found at $\delta^2 \mathrm{Ek}\,\mathrm{Ch}/4 \sim 1$. It is of particular interest that this transition is not given solely in terms of the Rossby number, as in the case of a decaying vortex like the one studied in Chapter 4.

In the regime dominated by Ekman boundary layer friction, the flow can be considered as Q2D since 3D motions can be parametrized by a linear damping term. When $\delta^2 \mathrm{Ek}\,\mathrm{Ch}/4 > 1$ the flow is similar to the case of no background rotation with non-negligible non-linear effects and the a damping rate that cannot be considered as a constant.

It has been shown that the different scaling regimes are associated with typical vertical profiles of the horizontal velocity. A particular feature for both shallow flows and flows subjected to background rotation is that, when the forcing is larger than a certain threshold, the vertical profile changes in such a way that the damping rate increases. This property is obviously absent in perfectly 2D flows. Consequently, certain phenomena characteristic of perfectly 2D flows at high Reynolds numbers cannot be observed neither in shallow flows nor in flows subjected to background rotation.

Chapter 9

Conclusions

The work described in this thesis was mainly motivated by the interest in generating quasi-two-dimensional (Q2D) flows in the laboratory to validate theoretical and numerical results on two-dimensional (2D) flows, specially 2D turbulence and 2D spatially periodic flows. Perfectly 2D flows are characterized by the absence of vortex stretching. This property is responsible for the occurrence of phenomena such as the inverse energy cascade and the process of self-organization.

In this thesis, we have investigated two of the common methods used to enforce the two-dimensionality of flows: (i) reducing the fluid depth or (ii) subjecting the flow to background rotation. The goal of this work is to deepen the understanding of the dynamics of shallow flows with and without background rotation in order to gain more insight about their two-dimensional character. To achieve this goal, we study the dynamics of generic vortical structures (monopolar and dipolar structures), which are the building blocks of more complicated flows, such as Q2D turbulence. The thesis can be divided in two main parts. Firstly, the study focuses on the evolution of flow structures that are decaying in time (Chapters 3 to 6), and secondly, on flow structures that are continuously driven by time-independent forcing (Chapters 7 and 8).

Shallow flows are commonly considered to be Q2D due to their limited depth, which is thought to restrain the magnitude of the vertical velocities, as derived from dimensional analysis of the continuity equation for incompressible flows. Inspired by recent doubts that have risen about the two-dimensionality of shallow flows (Satijn et al., 2001; Akkermans et al., 2008b,a; Cieslik et al., 2009), we revised this argument by studying the dynamics of decaying shallow axisymmetric swirl flows. It was found that a small aspect ratio δ (of the vertical to horizontal length scales of the flow) is not sufficient for a flow to be Q2D. Instead, the two-dimensionality of a shallow flow depends — as its dynamics — on the parameter $\delta^2 \mathrm{Re}$, with Re the Reynolds number. It can be concluded that the usual argument to consider shallow flows as Q2D is not valid in general.

To understand the reasons why some shallow swirl flows with and without

background rotation behave in a 2D way and to find the limits for such behavior, a thorough parametric study of the flow dynamics was performed using numerical simulations and a perturbation analysis with $\delta \ll 1$ as the perturbation parameter. It was found that decaying shallow swirl flows over a no-slip bottom can be considered as Q2D when the flow is dominated by bottom friction over the whole depth and the primary flow has a Poiseuille-like vertical profile. In such a case, the effects of vortex stretching are negligible as compared to viscous effects. This was later supported by the study of a dipolar vortex propagating over a no-slip bottom. For small values of $\delta^2 \mathrm{Re}$, it was observed that each of the vortex cores has a columnar structure (as determined by the λ_2 vortex detection criterion) that is independent of the vertical direction during the whole flow evolution. In contrast, for larger values of $\delta^2 \mathrm{Re}$, bottom friction becomes less dominant, and the flow consists of a boundary layer at the bottom and an inviscid interior. In this case, the columnar structure is deformed due to vortex stretching and looses its 2D character. These conclusions contradict the general belief that the presence of a solid bottom is one of the main features responsible for the three-dimensionality of shallow flows. Instead, the solid bottom stabilizes the flow and enforces its two-dimensional character.

On the other hand, decaying shallow swirl flows subjected to background rotation can be considered as Q2D for strong enough rotation (i.e. for small Rossby numbers Ro) irrespective of the aspect ratio. This is due to the linear coupling between the primary swirling motion and the secondary motions, which exists both when the primary flow has a Poiseuille-like vertical profile and when the flow is composed of a thin Ekman boundary layer at the bottom and an inviscid geostrophic interior.

When the evolution of decaying shallow vortices is not dominated by bottom friction, inertial oscillations are superimposed on the secondary motion driven by the bottom boundary layer. For shallow flows without background rotation, these oscillations are confined to the vortex core, and they decay on a similar time scale as the primary swirl motion. In contrast, these oscillations extend throughout the flow domain and persist even after the vortex has been damped when the system is subjected to background rotation.

The results for decaying shallow flows suggest that it is possible to obtain Q2D flows in the laboratory. However, it is difficult to generate flows with high enough Reynolds number for the study of Q2D turbulence in the laboratory. For shallow flows without background rotation, the value of the parameter $\delta^2 \mathrm{Re}$ must be small, and hence, the aspect ratio must be very small for large Re-values. In addition, Q2D shallow flows tend to decay very fast due to the strong interaction with the bottom, so that the value of the Reynolds number decreases very quickly. To address this latter issue, bottom friction can be reduced in a two-layer configuration as previously done by e.g. Paret & Tabeling (1997); Shats et al. (2005) and Akkermans et al. (2010), but even in this configuration, the value of the parameter $\delta^2 \mathrm{Re}$ must be small.

For background rotation to render a decaying shallow flow to be Q2D, it is

required that the Rossby number is small: Ro $\ll$ 1. This means that the convective acceleration must be small compared to the Coriolis acceleration. In the laboratory, this can be achieved in two ways: (i) by increasing the rotation rate of the system or (ii) by increasing the size of the setup. Both of these two possibilities pose technical difficulties for the construction of suitable experimental setups.

For steadily forced shallow flows with and without background rotation, we found two scaling regimes for the Reynolds number Re as a function of the magnitude of the forcing (quantified in Chapters 7 and 8 by the Chandrasekhar number Ch): (i) a linear regime where Re $\propto$ Ch and (ii) a nonlinear regime where Re $\propto$ Ch$^{1/2}$. In the linear regime, the flow can be considered as Q2D and the damping of the flow can be parametrized by a linear damping term, while in the nonlinear regime the flow is 3D. Well-defined limits for the Q2D behavior of such flows are given by the transition between the linear and the nonlinear regimes. The change in the scaling is related to a change in the vertical profile of the horizontal velocity. It is obvious that such changes cannot be observed in perfectly 2D flows.

The present work has been inspired by recent observations of the complex 3D behavior of some shallow flows (Akkermans et al., 2008a,b; Cieslik et al., 2009). In this thesis, we have studied in detail the dependence of the two-dimensional character of laminar shallow flows on the various flow parameters. By exploring the parameter space, clear boundaries for the two-dimensional behavior of such flows were found. Of particular interest is the fact that these boundaries do not depend solely on the aspect ratio of the flow domain, but on the thickness of the boundary layer above the no-slip bottom.

Furthermore, we have studied the effect of background rotation on shallow flows in order to analyze if rotation can actually enforce the two-dimensional character of such flows. It was found that the degree of two-dimensionality depends in a complex way on the length scales of the flow, its typical velocity scales, and the magnitude of the Coriolis force. As a matter of fact, it was found that under certain conditions background rotation may even increase the degree of three-dimensionality of a shallow flow.

Since many environmental flows (e.g. flows in the oceans, atmosphere, lakes, and rivers) are shallow and/or strongly affected by the Earth's rotation, it is tempting to extrapolate the results and conclusions from this thesis to such flows. However, this must be done with great caution. Two critical differences between environmental flows and the flows studied here can be immediately recognized: firstly, many environmental flows are density-stratified due to variations in temperature or salinity; secondly, most (if not all) environmental flows are highly turbulent. In spite of such complications, it is believed that the work presented in this thesis is an important step towards a better understanding of quasi-two-dimensional environmental flows.

Appendix A

Detailed analytical solution for a shallow swirl flow

To solve (3.26), we perform a Laplace transform according to

$$\hat{\Psi}(z,s) = \mathcal{L}[\Psi(z,t)] = \int_0^\infty \Psi(z,t)e^{-st}\mathrm{d}t, \tag{A.1}$$

where s is complex, and the real part of s is positive and sufficiently large for the integral to exist. Applying (A.1) into (3.26) yields

$$\frac{\partial^4 \hat{\Psi}}{\partial z^4} - s\frac{\partial^2 \hat{\Psi}}{\partial z^2} = \frac{2\sin(\pi z)}{2s + \pi^2}. \tag{A.2}$$

The solution of this equation is of the form $\hat{\Psi} = \hat{\Psi}_h + \hat{\Psi}_p$, where

$$\hat{\Psi}_h(z,s) = A + B\pi z + C\sinh(\sqrt{s}z) + D\cosh(\sqrt{s}z) \tag{A.3}$$

is the general solution of the homogeneous equation with A, B, C, and D integration constants; and

$$\hat{\Psi}_p(z,s) = \frac{2\sin(\pi z)}{\pi^2(s + \pi^2)(2s + \pi^2)} \tag{A.4}$$

is a particular solution of (A.2). The integration constants A, B, C, and D need to be chosen such that the solution $\hat{\Psi} = \hat{\Psi}_h + \hat{\Psi}_p$ satisfies the four (Laplace transformed) boundary conditions (3.28). Hence,

$$\hat{\Psi}(0,s) = A + D = 0, \tag{A.5}$$

$$\hat{\Psi}(1,s) = A + B\pi + C\sinh(\sqrt{s}) + D\cosh(\sqrt{s}) = 0, \tag{A.6}$$

129

$$\left.\frac{\partial \hat{\Psi}(z,s)}{\partial z}\right|_{z=0} = B\pi + C\sqrt{s} + \frac{2}{\pi(s+\pi^2)(2s+\pi^2)} = 0, \tag{A.7}$$

and

$$\left.\frac{\partial^2 \hat{\Psi}(z,s)}{\partial z^2}\right|_{z=1} = sC\sinh(\sqrt{s}) + sD\cosh(\sqrt{s}) = 0. \tag{A.8}$$

Solving (A.5)–(A.8) for the unknown integration constants, yields

$$A = -D = \frac{2}{\pi(s+\pi^2)(2s+\pi^2)} \frac{\tanh(\sqrt{s})}{\tanh(\sqrt{s}) - \sqrt{s}}. \tag{A.9}$$

$$B = -\frac{2}{\pi^2(s+\pi^2)(2s+\pi^2)} \frac{\tanh(\sqrt{s})}{\tanh(\sqrt{s}) - \sqrt{s}}, \tag{A.10}$$

and

$$C = \frac{2}{\pi(s+\pi^2)(2s+\pi^2)} \frac{1}{\tanh(\sqrt{s}) - \sqrt{s}}. \tag{A.11}$$

Thus, the solution of (A.2) is

$$\hat{\Psi}(z,s) = \frac{2}{\pi(s+\pi^2)(2s+\pi^2)}$$
$$\times \left(\frac{1}{\tanh(\sqrt{s}) - \sqrt{s}} \{\tanh(\sqrt{s})[1 - z - \cosh(\sqrt{s}z)] + \sinh(\sqrt{s}z)\} + \frac{\sin(\pi z)}{\pi} \right). \tag{A.12}$$

In order to obtain the solution of (3.26), we now must invert the Laplace transform (A.1) using the so-called Bromwich integral that is given by

$$\Psi(z,t) = \frac{1}{2\pi i} \int_{c-i\infty}^{c+i\infty} \hat{\Psi}(z,s) e^{st} ds, \quad c > 0, \tag{A.13}$$

where s is treated as a complex variable and the integration is upward along a straight line. The position of this line, i.e. the value of the real constant c is dictated by the requirement that c is positive and that all the singularities of $\hat{\Psi}(z,s)$ lie to the left of this line in the complex s-plane. The singularities of $\hat{\Psi}(z,s)$ are at $s = -\pi^2/2$ and $s = -\gamma_n^2$, where γ_n are solutions of the transcendental equation $\tan(\gamma_n) = \gamma_n$ with $\gamma_n \neq 0$. Note that all these singularities are simple poles, and that $s = 0$ and $s = -\pi^2$ are removable singularities. Also note that despite terms like $\sqrt{s}$, the integrand of (A.13) is single valued and a branch cut is not needed.

Equation (A.13) may now be conveniently evaluated using contour integration and the residue theorem. For that, the integration path in (A.13) is made part
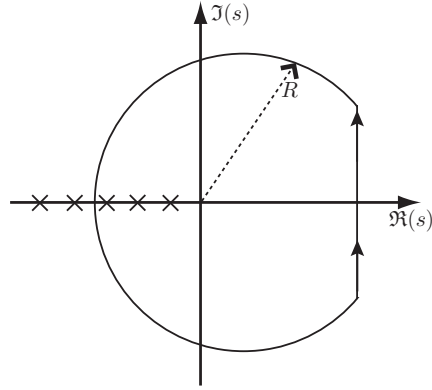
Figure A.1 – *The complex s-plane with the contour used for evaluating the Laplace inversion integral* (A.13). *The crosses on the real s-axis denote the simple poles of the integrand in* (A.13).

of a sequence of circular-arc completions of radius R that pass between the poles on the negative real s-axis; see figure A.1. It can be shown that the contribution of the circular-arc completions goes to zero if their radii $R \to \infty$. Therefore, the solution to (3.26), as determined by (A.13), is given by the sum of all the residues of $\hat{\Psi}(z, s)e^{st}$ at all the simple poles identified above. The final results is given by (3.30).

Appendix B

Perturbation analysis for a shallow monopolar vortex

Substitution of (4.16) into (4.6) and (4.7) yields

$$
\frac{\partial v_\theta}{\partial t} + A\delta^{k+2}\left(v_r\frac{\partial v_\theta}{\partial r} + \frac{v_\theta v_r}{r}\right) + A\delta^{k+1}v_z\frac{\partial v_\theta}{\partial z}
$$
$$
= -AB\delta^m v_r + \delta^2\left[\frac{\partial^2 v_\theta}{\partial r^2} + \frac{\partial}{\partial r}\left(\frac{v_\theta}{r}\right)\right] + \frac{\partial^2 v_\theta}{\partial z^2},
\tag{B.1}
$$

$$
\frac{\partial \omega_\theta}{\partial t} + A\delta^{k+2}\left(v_r\frac{\partial \omega_\theta}{\partial r} - \frac{\omega_\theta v_r}{r}\right) + A\delta^{k+1}v_z\frac{\partial \omega_\theta}{\partial z}
$$
$$
= A\delta^{k+2}\left(\frac{1}{r}\frac{\partial v_\theta^2}{\partial z} + B\delta^l\frac{\partial v_\theta}{\partial z}\right) + \delta^2\left[\frac{\partial^2 \omega_\theta}{\partial r^2} + \frac{\partial}{\partial r}\left(\frac{\omega_\theta}{r}\right)\right] + \frac{\partial^2 \omega_\theta}{\partial z^2},
\tag{B.2}
$$

where the expansions (4.14) of the velocity as a function of δ were also substituted.

B.1   Regime AI: $l > 0$, $k > -2$

We first consider the case where $l > 0$, $k > -2$, and hence, $m > 2$. In this case, $k + 2 > 0$ and (B.1) simplifies, at lowest order ($\delta \downarrow 0$), to

$$
\frac{\partial v_{\theta,0}}{\partial t} - \frac{\partial^2 v_{\theta,0}}{\partial z^2} = 0,
\tag{B.3}
$$

by neglecting all the terms of order δ^γ with $\gamma > 1$. Then, since $v_\theta = v_{\theta,0}$ at lowest order, (B.3) yields

$$
\frac{\partial v_\theta}{\partial t} - \frac{\partial^2 v_\theta}{\partial z^2} = 0.
\tag{B.4}
$$

133

For the secondary motion, the perturbation analysis yields

$$\frac{\partial \omega_{\theta,0}}{\partial t} - \frac{\partial^2 \omega_{\theta,0}}{\partial z^2} = 0 \tag{B.5}$$

at lowest order. Then $\omega_{\theta,n} = 0$ for $n = 1, ..., k+1$, and

$$\frac{\partial \omega_{\theta,k+2}}{\partial t} - \frac{\partial^2 \omega_{\theta,k+2}}{\partial z^2} = A \frac{1}{r} \frac{\partial v_{\theta,0}^2}{\partial z} \tag{B.6}$$

at order k. However, $\omega_{\theta,0} = 0$ since $v_{r,0} = v_{z,0}$ at $t = 0$, and finally,

$$\frac{\partial \omega_\theta}{\partial t} - \frac{\partial^2 \omega_\theta}{\partial z^2} = \delta^2 \mathrm{Re} \frac{1}{r} \frac{\partial v_\theta^2}{\partial z} \tag{B.7}$$

with

$$\omega_\theta = \delta^{k+2} \omega_{\theta,k+2} \tag{B.8}$$

at lowest order.

Since all the terms in (B.7) are of the same order, the velocity components must scale as

$$\frac{v_r}{v_\theta} = \mathcal{O}\left(\delta^2 \mathrm{Re}\right), \qquad \frac{v_z}{v_\theta} = \mathcal{O}\left(\delta^3 \mathrm{Re}\right). \tag{B.9}$$

B.2   Regime AII: $l > 0$, $k < -2$

If $k < -2$ and $l > 0$, (B.1) and (B.2) simplify into

$$\frac{\partial v_{\theta,0}}{\partial t} + A\delta^{k+2}\left(v_{r,0}\frac{\partial v_{\theta,0}}{\partial r} + \frac{v_{\theta,0}v_{r,0}}{r} + v_{z,1}\frac{\partial v_{\theta,0}}{\partial z}\right) = \frac{\partial^2 v_{\theta,0}}{\partial z^2}, \tag{B.10}$$

$$\frac{\partial \omega_{\theta,0}}{\partial t} + A\delta^{k+2}\left(v_{r,0}\frac{\partial \omega_{\theta,0}}{\partial r} - \frac{\omega_{\theta,0}v_{r,0}}{r} + v_{z,1}\frac{\partial \omega_{\theta,0}}{\partial z}\right) = A\delta^{k+2}\frac{1}{r}\frac{\partial v_{\theta,0}^2}{\partial z} + \frac{\partial^2 \omega_{\theta,0}}{\partial z^2} \tag{B.11}$$

with $v_\theta = v_{\theta,0}$ and $\omega_\theta = \omega_{\theta,0}$ by considering only the terms of order δ^γ with $\gamma \leq 0$.

If only the terms of order δ^{k+2} with $k + 2 < 0$ are considered in (B.10) and (B.11), bottom friction and the time dependence would be neglected. However, viscous effects must be important at least close to the bottom, where a boundary layer develops. To study the dynamics in the boundary layer, it is then convenient to stretch the vertical coordinate by defining the new variable $\tilde{z} = Re^{1/2}\delta z = A^{1/2}\delta^{k/2+1}z$. Equations (B.10) and (B.11) simplify to

$$v_{r,0}\frac{\partial v_{\theta,0}}{\partial r} + \frac{v_{\theta,0}v_{r,0}}{r} + v_{z,1}\frac{\partial v_{\theta,0}}{\partial z} = \frac{\partial^2 v_{\theta,0}}{\partial z^2}, \tag{B.12}$$

$$v_{r,0}\frac{\partial \omega_{\theta,0}}{\partial r} - \frac{\omega_{\theta,0}v_{r,0}}{r} + v_{z,1}\frac{\partial \omega_{\theta,0}}{\partial z} = \frac{1}{r}\frac{\partial v_{\theta,0}^2}{\partial z} + \frac{\partial^2 \omega_{\theta,0}}{\partial z^2}, \tag{B.13}$$

inside the boundary layer, where the convective acceleration and the viscous dissipation due to the bottom friction are of the same order.

However, if the full dynamics of the flow want to be solved in this regime,

$$\frac{\partial v_\theta}{\partial t} + \delta^2 \text{Re}\left(v_r\frac{\partial v_\theta}{\partial r} + \frac{v_\theta v_r}{r} + v_z\frac{\partial v_\theta}{\partial z}\right) = \frac{\partial^2 v_\theta}{\partial z^2}, \tag{B.14}$$

$$\frac{\partial \omega_\theta}{\partial t} + \delta^2 \text{Re}\left(v_r\frac{\partial \omega_\theta}{\partial r} - \frac{\omega_\theta v_r}{r} + v_z\frac{\partial \omega_\theta}{\partial z}\right) = \delta^2 \text{Re}\frac{1}{r}\frac{\partial v_\theta^2}{\partial z} + \frac{\partial^2 \omega_\theta}{\partial z^2}, \tag{B.15}$$

have to be solved.

Due to the non-linear nature of the governing equations in this regime, it has not been possible to analytically obtain a scaling law for the velocity components.

B.3   Regime AIII: $l > 0$, $k = -2$

In this regime, (B.1) and (B.2) simplify to (B.10) and (B.11) with $k+2 = 0$, which finally yields for this profile the governing equations:

$$\frac{\partial v_\theta}{\partial t} + \delta^2 \text{Re}\left(v_r\frac{\partial v_\theta}{\partial r} + \frac{v_\theta v_r}{r} + v_z\frac{\partial v_\theta}{\partial z}\right) = \frac{\partial^2 v_\theta}{\partial z^2}, \tag{B.16}$$

$$\frac{\partial \omega_\theta}{\partial t} + \delta^2 \text{Re}\left(v_r\frac{\partial \omega_\theta}{\partial r} - \frac{\omega_\theta v_r}{r} + v_z\frac{\partial \omega_\theta}{\partial z}\right) = \delta^2 \text{Re}\frac{1}{r}\frac{\partial v_\theta^2}{\partial z} + \frac{\partial^2 \omega_\theta}{\partial z^2}, \tag{B.17}$$

where only the Coriolis acceleration and horizontal viscous diffusion have been neglected at lowest order.

As in regime AII, it has not been possible to analytically obtain a scaling law for the velocity components due to the non-linear nature of the governing equations.

B.4   Regime BI: $l < 0$, $m > 0$

We now consider a regime where $l < 0$ and $m > 0$. Then $k + 2 > 1$, and the governing equation for v_θ at lowest order is

$$\frac{\partial v_{\theta,0}}{\partial t} - \frac{\partial^2 v_{\theta,0}}{\partial z^2} = 0, \tag{B.18}$$

by neglecting all the terms of order δ^γ with $\gamma > 1$. Then, since $v_\theta = v_{\theta,0}$ at lowest order, (B.18) yields

$$\frac{\partial v_\theta}{\partial t} - \frac{\partial^2 v_\theta}{\partial z^2} = 0 \tag{B.19}$$

as in regime AI.

For the secondary motion, the perturbation analysis yields

$$\frac{\partial \omega_{\theta,0}}{\partial t} - \frac{\partial^2 \omega_{\theta,0}}{\partial z^2} = 0, \tag{B.20}$$

and $\omega_{\theta,1} = ... = \omega_{\theta,m-1} = 0$. However, since $v_{r,0} = v_{z,0}$ at $t = 0$, then $\omega_{\theta,0} = 0$. Finally,

$$\frac{\partial \omega_{\theta,m}}{\partial t} - \frac{\partial^2 \omega_{\theta,m}}{\partial z^2} = AB\frac{\partial v_{\theta,0}}{\partial z} \tag{B.21}$$

at order m, so that at lowest order $(\delta \downarrow 0)$

$$\omega_\theta = \delta^m \omega_{\theta,m}. \tag{B.22}$$

Then (B.21) can be rewritten as

$$\frac{\partial \omega_\theta}{\partial t} - \frac{\partial^2 \omega_\theta}{\partial z^2} = \frac{2}{\text{Ek}}\frac{\partial v_\theta}{\partial z} \tag{B.23}$$

since $\text{Ek} = 2/(AB\delta^m)$. The previous equation implies that the velocity components scale as

$$\frac{v_r}{v_\theta} = \mathcal{O}\left(\frac{1}{\text{Ek}}\right), \qquad \frac{v_z}{v_\theta} = \mathcal{O}\left(\frac{\delta}{\text{Ek}}\right), \tag{B.24}$$

since all the terms must be of the same order.

B.5   Regime BII: $l < 0$, $m < 0$

If $l < 0$ and $m < 0$, $k + 2 < m$ and (B.2) yields

$$\frac{\partial v_{\theta,0}}{\partial z} = 0, \tag{B.25}$$

at lowest order. This equation would result in the trivial solution $v_{\theta,0} = 0$ due to the no-slip boundary condition at the bottom. However, from physical considerations, there must be a region close to the bottom where bottom friction is important. To examine this boundary layer region, the new vertical coordinate $\tilde{z} = \text{Ek}^{-1/2}z$ is defined. This definition implies that the relevant vertical scale is $h_{\text{Ek}} = \text{Ek}^{1/2}$, the Ekman boundary layer thickness.

B.5.1   The boundary layer

We define the new set of dimensionless variables, denoted by tildes, inside the boundary layer

$$\begin{aligned} \tilde{t} &= \text{Ek}^{-1/2}t, \quad \tilde{\omega}_\theta = \text{Ek}^{1/2}\omega_\theta, \\ \tilde{v}_r &= v_r, \qquad\quad \tilde{v}_\theta = v_\theta, \qquad \tilde{v}_z = \text{Ek}^{-1/2}v_z \end{aligned} \tag{B.26}$$

where the time scale is the Ekman time scale.

In this way, we obtain at lowest order the following equations:

$$\frac{\partial^2 \tilde{v}_\theta}{\partial \tilde{z}^2} - 2\tilde{v}_r = 0, \tag{B.27}$$

$$\frac{\partial^2 \tilde{\omega}_\theta}{\partial \tilde{z}^2} + 2\frac{\partial \tilde{v}_\theta}{\partial \tilde{z}} = 0, \tag{B.28}$$

$$\tilde{\omega}_\theta = \frac{\partial \tilde{v}_r}{\partial \tilde{z}}, \tag{B.29}$$

$$\frac{\delta}{r}\frac{\partial}{\partial r}(r\tilde{v}_r) + \frac{\partial \tilde{v}_z}{\partial \tilde{z}} = 0, \tag{B.30}$$

where all the terms are of order unity. Hence, the velocity components scale like

$$\frac{v_r}{v_\theta} = \mathcal{O}(1), \tag{B.31}$$

while the continuity equation (4.8) yields

$$\frac{v_z}{v_\theta} = \mathcal{O}(\mathrm{Ek}^{1/2}\delta), \tag{B.32}$$

in agreement with linear Ekman theory (see Pedlosky, 1987).

Combining (B.27)–(B.29) yields

$$\frac{\partial^2 \Phi}{\partial \tilde{z}^2} - 2i\Phi = iF(r, \tilde{t}), \tag{B.33}$$

where $\Phi = \tilde{v}_\theta + i\tilde{v}_r$, and $F(r, t)$ is an arbitrary integration function.

The general solution for equation (B.33) is

$$\Phi = -\frac{F(r, \tilde{t})}{2} + C_1 \exp\left[(1+i)\tilde{z}\right] + C_2 \exp\left[-(1+i)\tilde{z}\right], \tag{B.34}$$

where C_1 and C_2 are integration constants. Since Φ must be finite at $\tilde{z} \to \infty$, and $\Phi(\tilde{z} = 0) = 0$, then

$$C_1 = 0, \quad C_2 = F(r, \tilde{t})/2, \tag{B.35}$$

and

$$\Phi(r, \tilde{z}, \tilde{t}) = \frac{F(r, \tilde{t})}{2}\left[-1 + \exp(-\tilde{z})\cos(\tilde{z}) - i\exp(-\tilde{z})\sin(\tilde{z})\right]. \tag{B.36}$$

The vertical velocity component $\tilde{v}_z$ can be obtained by substituting (B.36) into (B.30) and integrating with respect to z:

$$
\begin{aligned}
\tilde{v}_z &= \delta \int_0^{\tilde{z}} \frac{1}{r}\frac{\partial}{\partial r}\{r\Im[\Phi(\tilde{t},r,s)]\}\mathrm{d}s \\
&= \frac{\delta}{2r}\frac{\partial}{\partial r}[r\Im(F)]\int_0^{\tilde{z}}[-1+\exp(-\tilde{z})\cos(\tilde{z})]\mathrm{d}s \\
&\quad -\frac{\delta}{2r}\frac{\partial}{\partial r}[r\Re(F)]\int_0^{\tilde{z}}[\exp(-\tilde{z})\sin(\tilde{z})]\mathrm{d}s
\end{aligned}
\tag{B.37}
$$

where $\Im$ denotes the imaginary part and $\Re$ the real part of the number.

B.5.2 The geostrophic interior

Equation (B.37) implies that there is a vertical velocity of order $\delta\mathrm{Ek}^{1/2}$ which is pumped towards the interior flow above the boundary layer. It is then convenient to define $V_z = \delta^{-1}\mathrm{Ek}^{-1/2}v_z$ in the interior flow. Substituting this into the continuity equation (4.8) yields

$$
\frac{\delta}{r}\frac{\partial}{\partial r}(rv_r) + \delta\,\mathrm{Ek}^{1/2}\frac{\partial V_z}{\partial z} = 0.
\tag{B.38}
$$

Then, by defining $V_r = \mathrm{Ek}^{-1/2}v_r$, (B.38) can be rewritten as

$$
\frac{1}{r}\frac{\partial}{\partial r}(rV_r) + \frac{\partial V_z}{\partial z} == 0,
\tag{B.39}
$$

where V_r and V_z are of the same order. Substituting the definitions of V_r and V_z into equations (B.27) and (B.28) yields

$$
\frac{\partial V_\theta}{\partial t} = -2V_r,
\tag{B.40}
$$

$$
\frac{\partial V_\theta}{\partial z} = 0,
\tag{B.41}
$$

$$
W_\theta = \frac{\partial V_r}{\partial z} = 0,
\tag{B.42}
$$

$$
\frac{1}{r}\frac{\partial}{\partial r}(rV_r) + \frac{\partial V_z}{\partial z} = 0
\tag{B.43}
$$

with $V_\theta = v_\theta$, and where all the variables denoted with a capital letter are of $\mathcal{O}(1)$. Therefore, the velocity components scale like

$$
\frac{v_r}{v_\theta} = \mathcal{O}(\mathrm{Ek}^{1/2}),
\tag{B.44}
$$

$$
\frac{v_z}{v_\theta} = \mathcal{O}(\delta\mathrm{Ek}^{1/2}),
\tag{B.45}
$$

in the interior flow.

Matching of the geostrophic interior and the boundary layer

From (B.41) and (B.42), it can be seen that $V_r = V_r(r,t)$ and $V_\theta = V_\theta(r,t)$. Now, it is possible to match the interior flow with the boundary layer ($\tilde{v}_r = \mathrm{Ek}^{1/2}V_r$ and $\tilde{v}_\theta = V_\theta$ as $\tilde{z} \to \infty$) yielding $F(r,t) = V_\theta + i\mathrm{Ek}^{1/2}V_r$. At lowest order $\delta \downarrow 0$ (i.e. $\mathrm{Ek}^{1/2} \downarrow 0$), $F(r,t) = -2V_\theta$ and integration of (B.37) for $\bar{z} \to \infty$ gives the Ekman pumping condition:

$$v_z(r, \tilde{z} \to 0, t) = \frac{\delta\,\mathrm{Ek}^{1/2}}{4r}\frac{\partial}{\partial r}(rV_\theta) = \frac{\delta\,\mathrm{Ek}^{1/2}}{2}\omega_z,\tag{B.46}$$

$$V_z(r, z \to 0, t) = -\frac{1}{2}\omega_z.\tag{B.47}$$

Integration of the continuity equation (B.43) yields

$$V_z = -\frac{z}{r}\frac{\partial}{\partial r}(rV_r) + G(r,t)\tag{B.48}$$

where $G(r,t)$ is an unknown integration function. Applying the boundary conditions

$$G(r,t) = \frac{1}{2}W_z \quad \text{for} \quad z = 0,\tag{B.49}$$

$$G(r,t) - \frac{1}{r}\frac{\partial}{\partial r}(rV_r) = 0 \quad \text{for} \quad z = 1,\tag{B.50}$$

yields, after elimination of G,

$$\frac{1}{r}\frac{\partial}{\partial r}(rV_r) = \frac{1}{\sqrt{2}}W_z,\tag{B.51}$$

and

$$V_r = \frac{1}{2}V_\theta.\tag{B.52}$$

Substituting (B.52) into (B.40) yields

$$\frac{\partial V_\theta}{\partial t} + V_\theta = 0.\tag{B.53}$$

This equation is solved using the initial condition $V_\theta(t=0) = R(r)$ yielding

$$V_\theta = R(r)e^{-t/\sqrt{2}},\tag{B.54}$$

which can be use to obtain expression for the other two velocity components:

$$V_r = \frac{1}{\sqrt{2}}R(r)e^{-t/\sqrt{2}},\tag{B.55}$$

$$V_z = \frac{1}{\sqrt{2}}(1-z)\frac{1}{r}\frac{\partial}{\partial r}[rR(r)]e^{-t/\sqrt{2}}.\tag{B.56}$$

B.6   Regime BIII: $l < 0$, $m = 0$

For $l < 0$ and $m = 0$ ($k + 2 > 1$), (B.1) and (B.2) simplify at lowest order into

$$\frac{\partial v_{\theta,0}}{\partial t} - \frac{\partial^2 v_{\theta,0}}{\partial z^2} = -\frac{2}{\text{Ek}} v_{r,0}, \tag{B.57}$$

$$\frac{\partial \omega_{\theta,0}}{\partial t} - \frac{\partial^2 \omega_{\theta,0}}{\partial z^2} = \frac{2}{\text{Ek}} \frac{\partial v_{\theta,0}}{\partial z}. \tag{B.58}$$

Since $m = 0$, from (4.17), $\text{Ek} = \mathcal{O}(1)$ and $h_{\text{Ek}} = \text{Ek}^{1/2} = (AB)^{-1/2}$. In other words, in this regime the thickness of the Ekman boundary layer is of the order of the fluid depth.

B.7   Regime CI: $m > 0$, $k > -2$, $l = 0$

For intermediate rotation rates $l = 0$, which means that the Coriolis acceleration is of the same order as the convective acceleration. If $m > 0$ and $k > -2$, viscous forces govern the evolution of the primary flow. Hence, the governing equation for v_θ is again

$$\frac{\partial v_{\theta,0}}{\partial t} - \frac{\partial^2 v_{\theta,0}}{\partial z^2} = 0, \tag{B.59}$$

and $\omega_{\theta,0} = ... = \omega_{\theta,k+1} = 0$. On the other hand, at order δ^{k+2} the governing equation for ω_θ is

$$\frac{\partial \omega_\theta}{\partial t} - \frac{\partial^2 \omega_\theta}{\partial z^2} = \delta^2 \text{Re} \left(\frac{\partial v_{\theta,0}^2}{\partial z} + \frac{1}{\text{Ro}} \frac{\partial v_{\theta,0}}{\partial z} \right). \tag{B.60}$$

with $\omega_\theta = \delta^{k+2} \omega_{\theta,k+2}$. Note that the solution for ω_θ is simply the linear combination of the solutions for regimes AI and BI.

B.8   Regime CII: $m < 0$, $k < -2$, $l = 0$

In this regime, the viscous terms can be neglected at lowest order, except next to the bottom where viscous effects must be important to satisfy the no-slip boundary condition. Hence, there must be a boundary layer close to the bottom under the inviscid interior, as in regimes AII and BII. However, in this case, the thickness of the boundary layer is neither h_{Re} nor h_{Ek}. Due to the non-linear nature of this regime and the boundary layer, no simplifications can be made to the equations and the flow is governed by the full equations (4.6) and (4.7).

B.9 Regime CIII: $m = 0$, $k = -2$

This last regime is straight forward. No single simplification can be made, and all the terms are of the same order. Hence, at lowest order the flow is governed by the full equations (4.6) and (4.7).

Appendix C

Radial dependence of inertial oscillations in a Rankine Vortex

This appendix presents the detailed solution of (5.24)

$$r\frac{\mathrm{d}}{\mathrm{d}r}\left(\frac{1}{r}\frac{\mathrm{d}R}{\mathrm{d}r}\right) - k_n^2 R = -k_n^2\frac{\eta(r)}{\xi^2}R, \tag{C.1}$$

for the Rankine vortex given in (5.33).

Interior $(r < 1)$

In the interior of the vortex, (C.1) can be rewritten as

$$\frac{\mathrm{d}^2 R^*}{\mathrm{d}r^2} + \frac{1}{r}\frac{\mathrm{d}R^*}{\mathrm{d}r} + \left[k_n^2\left(\frac{1}{\xi^2} - 1\right) - \frac{1}{r^2}\right]R^* = 0, \tag{C.2}$$

where $R^* = R/r$. This equation is known as a Bessel equation, and the solution is of the form

$$R^*(r) = C_1 J_1(\alpha r) + C_2 Y_1(\alpha r), \tag{C.3}$$

where

$$\alpha = \begin{cases} \sqrt{k_n^2\left(\dfrac{1}{\xi^2} - 1\right)} & \text{for} \quad \xi^2 < 1, \\[4mm] i\sqrt{k_n^2\left(1 - \dfrac{1}{\xi^2}\right)} & \text{for} \quad \xi^2 > 1, \end{cases} \tag{C.4}$$

143

is the wave number inside the vortex core; J_1 is the first-order Bessel function of the first kind, while Y_1 is the first-order Bessel function of the second kind. Since ψ_1 must be finite at $r = 0$, while $Y_1(0) = \infty$, we require $C_2 = 0$. The solution thus becomes:

$$R(r) = \begin{cases} C_1 r J_1(\alpha r) & \text{for} \quad \xi^2 < 1 \\ C_1 r I_1(\alpha r) & \text{for} \quad \xi^2 > 1 \end{cases} \tag{C.5}$$

Exterior $(r > 1)$

In the exterior of the vortex, the equation for $R^*(r)$ is

$$r^2 \frac{\mathrm{d}^2 R^*}{\mathrm{d}r^2} + r \frac{\mathrm{d}R^*}{\mathrm{d}r} - \left[1 - \frac{k_n^2}{\xi^2 \mathrm{N}^2 \mathrm{Ro}} + k_n^2 \left(1 - \frac{1}{\xi^2 \mathrm{N}^2 \mathrm{Ro}^2}\right) r^2\right] R^* = 0, \tag{C.6}$$

which can be rewritten as

$$r^2 \frac{\mathrm{d}^2 R^*}{\mathrm{d}r^2} + r \frac{\mathrm{d}R^*}{\mathrm{d}r} - \left[\gamma^2 + \frac{\beta^2}{\mathrm{R}_c^2} r^2\right] R^* = 0, \tag{C.7}$$

where R_c is the radius of the cylinder, $\gamma^2 = 1 - k_n^2/(\xi^2 \mathrm{N}^2 \mathrm{Ro})$, and $\beta^2 = k_n^2 \mathrm{R}_c^2 \{1 - [\xi(\mathrm{Ro}+1)]^{-2}\}$. Note that both γ and β can be either real or imaginary.

If $\xi^2 > (\mathrm{Ro}+1)^{-2}$, then we take $\beta = k_n \mathrm{R}_c \sqrt{1 - [\xi(\mathrm{Ro}+1)]^{-2}} \in \mathbb{R}^+$, and (C.7) can be solved in terms of the modified Bessel functions of order γ. For computational convenience, we wish to construct two linearly independent solutions of (C.7) that are real-valued irrespective of $\gamma \in \mathbb{R}$ or $\gamma \in \mathbb{I}$. It is thus found that

$$R(r) = C_3 r K_\gamma(\beta r/\mathrm{R}_c) + C_4 r L_\gamma(\beta r/\mathrm{R}_c), \tag{C.8}$$

where

$$L_\gamma(x) = \frac{1}{2}\left[I_\gamma(x) + I_{-\gamma}(x)\right]. \tag{C.9}$$

I_γ and K_γ are the modified Bessel functions of order γ of the first and second kind, respectively.

The boundary condition at the external wall requires $\psi(r = \mathrm{R}_c) = 0$, and hence

$$C_3 K_\gamma(\beta) + C_4 L_\gamma(\beta) = 0. \tag{C.10}$$

For large values of β, $K_\gamma(\beta) \to 0$ while $L_\gamma(\beta) \to \infty$. In this case C_4 must be very small, and the solution can be largely simplified. Nonetheless, the complete solution will be presented here.

The solutions in the interior and the exterior have to be matched. Since the frequency in the interior and the exterior are assumed to be the same, α must be related to β according to

$$\alpha^2 = \mathrm{N}^2 \mathrm{Ro}^2 \left(k_n^2 - \frac{\beta^2}{\mathrm{R}_c^2}\right) - k_n^2. \tag{C.11}$$

In addition, continuity in ψ and $\partial\psi/\partial r$ should be imposed at $r = 1$, which yields

$$C_1 = \frac{C_3}{J_1(\alpha)}\left[K_\gamma(\beta/\mathrm{R_c}) - \frac{K_\gamma(\beta)}{L_\gamma(\beta)}L_\gamma(\beta/\mathrm{R_c})\right] \tag{C.12}$$

and

$$\frac{\alpha J_0(\alpha)}{J_1(\alpha)} = \frac{\left.\dfrac{\partial}{\partial r}\left[rK_\gamma(\beta r/\mathrm{R_c})\right]\right|_{r=1} - \dfrac{K_\gamma(\beta)}{L_\gamma(\beta)}\dfrac{\partial}{\partial r}\left[rL_\gamma(\beta r/\mathrm{R_c})\right]\bigg|_{r=1}}{K_\gamma(\beta/\mathrm{R_c}) - \dfrac{K_\gamma(\beta)}{L_\gamma(\beta)}L_\gamma(\beta/\mathrm{R_c})}. \tag{C.13}$$

The latter equation is a transcendental equation for α, which can have several solutions, each of them corresponding to a different frequency ξ. For $\xi > 1$, the left-hand side of this transcendental equation has to be replaced by $|\alpha|I_0(|\alpha|)/I_1(|\alpha|)$.

If $\xi < (\mathrm{Ro} + 1)^{-2}$, $\beta = i\beta^*$ with $\beta^* = k_n\mathrm{R_c}\sqrt{[\xi(\mathrm{Ro} + 1)]^{-2} - 1} \in \mathbb{R}^+$, and (C.7) can be written as

$$r^2\frac{\mathrm{d}^2 R^*}{\mathrm{d}r^2} + r\frac{\mathrm{d}R^*}{\mathrm{d}r} + \left[\frac{\beta^{*2}}{\mathrm{R_c^2}}r^2 - \gamma^2\right]R^* = 0. \tag{C.14}$$

The solution to (C.14) can be written in terms of Bessel functions of the first and second kind. Again, for computational convenience, we introduce the following two real-valued, linearly independent solutions:

$$B_\gamma(x) = \frac{1}{2}[J_\gamma(x) + J_{-\gamma}(x)] \tag{C.15}$$

and

$$D_\gamma(x) = \frac{1}{2}[Y_\gamma(x) + Y_{-\gamma}(x)]. \tag{C.16}$$

A solution of (C.14) can then be written as

$$R(r) = C_3 r B_\gamma(\beta^* r/\mathrm{R_c}) + C_4 r D_\gamma(\beta^* r/\mathrm{R_c}). \tag{C.17}$$

Applying the boundary condition at the external wall yields

$$C_4 = -C_3\frac{B_\gamma(\beta^*)}{D_\gamma(\beta^*)}, \tag{C.18}$$

while continuity of ψ and $\partial\psi/\partial r$ at $r = 1$ yields

$$C_1 = \frac{C_4}{J_1(\alpha)}\left[B_\gamma(\beta^*/\mathrm{R_c}) - \frac{B_\gamma(\beta^*)}{D_\gamma(\beta^*)}D_\gamma(\beta^*/\mathrm{R_c})\right], \tag{C.19}$$

and

$$\frac{\alpha J_0(\alpha)}{J_1(\alpha)} = \frac{\left.\dfrac{\partial}{\partial r}\left[rB_\gamma(\beta^* r/\mathrm{R_c})\right]\right|_{r=1} - \dfrac{B_\gamma(\beta^*)}{D_\gamma(\beta^*)}\left.\dfrac{\partial}{\partial r}\left[rD_\gamma(\beta^* r/\mathrm{R_c})\right]\right|_{r=1}}{B_\gamma(\beta^*/\mathrm{R_c}) - \dfrac{B_\gamma(\beta^*)}{D_\gamma(\beta^*)}D_\gamma(\beta^*/\mathrm{R_c})}, \quad (\mathrm{C}.20)$$

which is again a transcendental equation for α. Here too, if $\xi > 1$, the left hand side of this expression has to be replaced by $|\alpha|I_0(|\alpha|)/I_1(|\alpha|)$.

On the other hand, it can be seen that the expression cannot satisfy the boundary condition $R(r) \to 0$ as $r \to \infty$ because the Bessel functions decay like $r^{-1/2}$ as $r \to \infty$, and hence, $R(r)$ grows like $r^{1/2}$ as $r \to \infty$.

Appendix D

The magnetic field of a rectangular magnet

The relevant equations to compute the magnetic field of the permanent magnet configuration used in Chapter 8 are

$$\nabla \cdot \boldsymbol{B} = 0, \tag{D.1}$$

$$\nabla \times \boldsymbol{H} = \boldsymbol{J}_{free} = 0 \quad \rightarrow \quad \boldsymbol{H} = -\nabla \Phi, \tag{D.2}$$

$$\boldsymbol{H} = \frac{\boldsymbol{B}}{\mu_0} - \boldsymbol{M}, \tag{D.3}$$

where $\boldsymbol{B}$ is the magnetic field; $\boldsymbol{J}_{free}$ is the free current density; Φ is the magnetic potential; μ_0 is the magnetic permeability; and $\boldsymbol{M}$ is the magnetization.

We consider a rectangular magnet with thickness d and sides $2L_m$ and $6L_m$ which is homogeneously magnetized in the z-direction, so that

$$\boldsymbol{M} = M_0 \hat{\boldsymbol{k}} \quad \text{for} \quad |x| < 3L_m, \ |y| < L_m, \text{ and } -d < z < 0 \tag{D.4}$$

with M_0 the magnitude of the magnetization.

It is convenient to define the following dimensionless variables denoted by tildes

$$\begin{aligned} (\tilde{x}, \tilde{y}, \tilde{z}) &= \frac{1}{L_m}(x, y, z), \quad \tilde{\Phi} = \frac{\Phi}{L_m M_0}, \quad \tilde{M} = \frac{M}{M_0}, \\ \tilde{\boldsymbol{B}} &= \frac{\boldsymbol{B}}{\mu_0 M_0} = \frac{\boldsymbol{B}}{B_0}, \quad \tilde{\eta} = \frac{d}{L_m} \end{aligned} \tag{D.5}$$

with $B_0 = \mu_0 M_0$ the typical magnitude of the magnetic field. From now on, the tildes will be omitted to simplify the notation.

Combining (D.1)–(D.3) results in a Poisson equation for the magnetic potential

$$
\nabla^2 \Phi = \nabla \cdot \boldsymbol{M}
$$
$$
= \begin{cases} \delta_D(z+\eta) - \delta_D(z) & \text{for} \quad |x| < 3 \cap |y| < 1, \\ 0 & \text{for} \quad |x| > 3 \cup |y| > 1, \end{cases} \tag{D.6}
$$

where δ_D is the Dirac delta function, and $\boldsymbol{M} = \hat{\boldsymbol{k}}$, for $|x| < 3$, $|y| < 1$, and $-\eta < z < 0$. The solution to (D.6) is then

$$
\Phi(x,y,z) = F(x,y,z) - F(x,y,z+\eta) \tag{D.7}
$$

with

$$
F(x,y,z) = \frac{1}{4\pi} \int_{x-3}^{x+3} d\kappa \int_{y-1}^{y+1} d\xi \frac{1}{\sqrt{\kappa^2 + \xi^2 + z^2}}, \tag{D.8}
$$

from which the solution for the magnetic field in the x and y directions easily follows. However, here we shall not develop the solution for B_y, the magnetic field in the y-direction, since it is parallel to the electric current and has no effect on the forcing. To calculate B_x, the magnetic field in the x-direction, we first integrate (D.8) with respect to ξ, so that

$$
F(x,y,z) = \frac{1}{4\pi} \int_{x-3}^{x+3} d\kappa \left\{ \ln\left[y+1+\sqrt{\kappa^2 + (y+1)^2 + z^2}\right] \right.
$$
$$
\left. - \ln\left[y-1+\sqrt{\kappa^2 + (y-1)^2 + z^2)}\right] \right\} \tag{D.9}
$$

and

$$
\begin{aligned}
B_x = -\frac{\partial \Phi}{\partial x} = &P(x+3,y+1,z+\eta) - P(x+3,y-1,z+\eta) \\
&+ P(x-3,y-1,z+\eta) - P(x-3,y+1,z+\eta) \\
&- P(x+3,y+1,z) + P(x+3,y-1,z) \\
&- P(x-3,y-1,z) + P(x-3,y+1,z)
\end{aligned} \tag{D.10}
$$

with

$$
P(x,y,z) = \frac{1}{4\pi} \ln(y+\sqrt{x^2+y^2+z^2}). \tag{D.11}
$$

To calculate the magnitude of the magnetic field in the z-direction B_z, we calculate the derivative of F in the z-direction

$$
\begin{aligned}
\frac{\partial F}{\partial z} = \frac{1}{4\pi} \int_{x-3}^{x+3} d\kappa \left[\frac{1}{y+1+\sqrt{\kappa^2+(y+1)^2+z^2}} \frac{z}{\sqrt{\kappa^2+(y+1)^2+z^2}} \right. \\
\left. - \frac{1}{y-1+\sqrt{\kappa^2+(y-1)^2+z^2}} \frac{z}{\sqrt{\kappa^2+(y-1)^2+z^2}} \right],
\end{aligned} \tag{D.12}
$$

which yields after integration

$$\frac{\partial F}{\partial z} = W(x+1, y+1, z) - W(x-1, y+1, z) \tag{D.13}$$

with

$$W(x, y, z) = \frac{1}{2\pi} \arctan\left(\frac{\sqrt{y^2 + z^2} - y}{z} \frac{\sqrt{x^2 + y^2 + z^2} - \sqrt{y^2 + z^2}}{x}\right). \tag{D.14}$$

Finally, the magnitude of the magnetic field in the z-direction for the rectangular magnet considered is given by

$$\begin{aligned} B_z =& W(x+3, y+1, z+\eta) - W(x-3, y+1, z+\eta) \\ &- W(x+3, y-1, z+\eta) + W(x-3, y-1, z+\eta) \\ &- W(x+3, y+1, z) + W(x-3, y+1, z) \\ &+ W(x+3, y-1, z) + W(x-3, y-1, z). \end{aligned} \tag{D.15}$$

Bibliography

Afanasyev, Y. & Wells, J. (2005). "Quasi-two-dimensional turbulence on the polar beta-plane: laboratory experiments". *Geophys. Astr. Fluid Dyn.*, 99, 1–17. 3, 31, 113

Afanasyev, Y. K. & Jewtoukoff, V. (2009). "Dipolar gyres generated by continuous forcing on a polar β-plane". *Phys Fluids*, 21, 066602–1–7. 114

Akkermans, R. A. D., Cieslik, A. R., Kamp, L. P. J., Trieling, R. R., Clercx, H. J. H., & Van Heijst, G. J. F. (2008a). "The three-dimensional structure of an electromagnetically generated dipolar vortex in a shallow fluid layer". *Phys. Fluids*, 554, 116601–1–15. 5, 15, 17, 35, 79, 82, 83, 93, 94, 96, 125, 127

Akkermans, R. A. D., Kamp, L. P. J., Clercx, H. J. H., & van Heijst, G. J. F. (2008b). "Intrinsic three-dimensionality in electromagnetically driven shallow flows". *EPL*, 83, 24001–1–6. 5, 15, 17, 28, 35, 74, 79, 80, 83, 93, 96, 99, 125, 127

Akkermans, R. A. D., Kamp, L. P. J., Clercx, H. J. H., & van Heijst, G. J. F. (2010). "Three-dimensional flow in electromagnetically driven two-layer fluids". *Phys. Rev. E.*, 82, 026314–1–11. 5, 126

Albagnac, J., Brancher, P., Eiff, O., Lacaze, L., & Moulin, F. (2010). "On the existence and evolution of a spanwise vortex in laminar shallow water dipoles". *Phys. Fluids*, in preparation. 80

Arendt, S., Fritts, D., & Andreassen, O. (1997). "The initial value problem for Kelvin vortex waves". *J. Fluid Mech.*, 344, 181–212. 55

Batchaev, A. M. (1990). "Self-oscillaiton regimes in a system of four quasi-two-dimensional vortices". *Zh. Prikl. Mekh. Tekh. Fiz.*, 4, 85–91. 103

Batchelor, G. K. (1969). "Computation of the energy spectrum in homogeneous two-dimensional turbulence". *Phys. Fluids (Suppl.)*, 12, II233–II239. 2

Berger, S. A., Talbot, L., & Yao, L.-S. (1983). "Flow in curved pipes". *Ann. Rev. Fluid Mech.*, 15, 461–512. 27

Billant, P. & Chomaz, J. (2000). "Experimental evidence for a new instability of a vertical columnar vortex pair in a strongly stratified fluid". *J. Fluid Mech.*, 418, 167–188. 82

Bodarenko, N. F., Z., G. M., & Dolzhanskiy, F. V. (1979). "Laboratory and theoretical models of plane periodic flows". *Izv. Acad. Sci. USSR Atmos. Oceanic Phys.*, 15, 711–716. 4, 99, 109

Bödewadt, U. (1940). "Die Drehströmung über festem Grund". *Z. Angew. Math. Mech*, 20, 241–253. 87, 106

Boffetta, G. (2007). "Energy and enstrophy fluxes in the double cascade of 2D turbulence". *J. Fluid Mech.*, 589, 253–260. 1

Boffetta, G., Cenedese, A., Espa, S., & Musacchio, S. (2005). "Effects of friction on 2D turbulence: An experimental study of the direct cascade". *Europhys. Lett.*, 71, 590–596. 14

van Bokhoven, L. J. A., Trieling, R. R., Clercx, H. J. H., & van Heijst, G. J. F. (2007). "The influence of initial conditions on decaying two-dimensional turbulence". *Phys. Fluids*, 19, 046601–1–12. 2

Bracco, A., McWilliams, J. C., Murante, G., Provenzale, A., & Weiss, J. (2000). "Revisiting freely decaying two-dimensional turbulence at milennial resolution". *Phys. Fluids*, 12, 2931–2941. 2

Brink, K. H. (1997). "Time-dependent motions and the nonlinear bottom Ekman layer". *J. Mar. Res.*, 55, 613–631. 54

Carnevale, G., McWilliams, J., Pomeau, Y., Weiss, J., & Young, W. R. (1991). "Evolution of vortex statistics in two-dimensional turbulence". *Phys. Rev. Lett.*, 66, 2735–2737. 2, 5

Carnevale, G. F., Briscolini, M., Kloosterziel, R. C., & Vallis, G. K. (1997). "Three-dimensionally perturbed vortex tubes in a rotating flow". *J. Fluid Mech.*, 341, 127–163. 6, 44, 56

Chandrasekhar, S. (1961). *"Hydrodynamic and hydromagnetic stability"*. The Clarendon Press, Oxford. 102

Cieslik, A. R., Kamp, L. P. J., Clercx, H. J. H., & van Heijst, G. J. F. (2009). "Meandering streams in a shallow fluid layer". *Europhys. Lett.*, 85, 54001–1–6. 5, 17, 125, 127

Clercx, H. J. H. & Nielsen, A. H. (2000). "Vortex statistics for turbulence in a container with rigid boundaries". *Phys. Rev. Lett.*, 85, 752–755. 2

Clercx, H. J. H. & van Heijst, G. J. F. (2009). "Two-dimensional Navier-Stokes turbulence in bounded domains". *App. Mech. Rev.*, 62, 020802–1–25. 2, 5, 11

Clercx, H. J. H., van Heijst, G. J. F., & Zoetewij, M. L. (2003). "Quasi-tow-dimensional turbulence in shallow fluid layers: the role of bottom friction and fluid layer depth". *Phys. Rev. E*, 67, 066303–1–9. 14, 28, 99

COMSOL AB (2008). "Comsol 3.5 User's guide". available as of May 2008 at http:\\www.comsol.com. 24, 68, 71, 82, 116

Couder, Y. (1984). "Two-dimensional grid turbulence in a thin liquid-film". *J. Physique Lett.*, 45, L353–L360. 4

Danilov, S. D. & Dovzhensko, V. A. (1996). "Subcritical flow in a system of four vortices". *Atmos. Oceanic Phys.*, 31, 593–598. 99, 109, 111

Danilov, S. D. & Gurarie, D. (2000). "Quasi-two-dimensional turbulence". *Phys. Usp*, 43, 863–900. 2

Dauxois, T., Fauve, S., & Tuckerman, L. (1996). "Stability of periodic arrays of vortices". *Phys. Fluids*, 8, 487–495. 99

Davidson, P. A. (1989). "The interaction between swirling and recirculating velocity components in unsteady, inviscid flow". *J. Fluid Mech.*, 209, 35–55. 34

Davidson, P. A. (1999). "Magnetohydrodynamics in materials processing". *Annu. Rev. Fluid Mech.*, 31, 273–300. 99

Davidson, P. A., Staplehurst, P. J., & Dalziel, S. B. (2006). "On the evolution of eddies in a rapidly rotating system". *J. Fluid Mech.*, 557, 135–144. 6

Dean, W. R. (1927). "XVI. Note on the motion of fluid in a curved pipe". *Phil. Mag. S. 7*, 4, 208–223. 26

Dolzhanskii, F. V., Krymov, V. A., & Manin, D. Y. (1990). "Stability and vortex structures of quasi-two-dimensional shear flows". *Sov. Phys. Usp.*, 33, 495–520. 2, 31, 109

Dolzhanskii, F. V., Krymov, V. A., & Manin, D. Y. (1992). "An advanced experimental investigation of quasi-two-dimensional shear flows". *J. Fluid Mech.*, 241, 705–722. 14, 22, 99, 109, 119

Dolzhanskiy, F. V. (1987). "Effect of external friction on the stability of plane-parallel flows in a homogeneous incompressible liquid". *Izv. Atmos. Oceanic Phys.*, 23, 262–268. 4, 111

Dritschel, D. G. (1993). "Vortex properties of two-dimensional turbulence". *Phys. Fluids A*, 5, 984–997. 2

Duran-Matute, M., Kamp, L. P. J., Trieling, R. R., & van Heijst, G. J. F. (2009). "Inertial oscillations in a confined monopolar vortex subjected to background rotation". *Phys. Fluids*, 21, 116602–1–13. 55

Duran-Matute, M., Kamp, L. P. J., Trieling, R. R., & van Heijst, G. J. F. (2010). "Scaling of decaying shallow axisymmetric swirl flows". *J. Fluid Mech.*, 648, 509–519. 17, 37, 71, 79, 80, 84, 85, 96, 97, 108, 109

Einstein, A. (1926). "Die Ursache der Mäanderbildung der Flu/ssläufe und des sogenanten Baerschen Gesetzes". *Naturwissenschaften*, 14, 223–224. 17

Fabre, D., Sipp, D., & Jacquin, L. (2006). "Kelvin waves and the singular modes of the Lamb-Oseen vortex". *J. Fluid Mech.*, 551, 235–274. 56, 68, 69

Figueroa, A., Demiaux, F., Cuevas, S., & Ramos, E. (2009). "Electrically driven vortices in a weak dipolar magnetic field in a shallow electrolytic layer". *J. Fluid Mech.*, 641, 245–261. 100, 102, 111

Flòr, J. & Van Heijst, G. (1994). "An experimental study of dipolar vortex structures in a stratified fluid". *J. Fluid Mech.*, 279, 101–133. 82

Frisch, U. & Sulem, P.-L. (1984). "Numerical simulation of the inverse energy cascade in two-dimensional turbulence". *Phys. Fluids*, 27, 1921–1923. 1

Fultz, D. (1959). "A note on overstability and the elastoid-inertia oscillations of Kelvin, Solberg, and Bjerknes". *J. Atmos. Sci.*, 16, 199–208. 55, 64, 65

Gotoh, K. & Yamada, M. (1984). "Instability of a cellular flow". *J. Phys. Soc. Jpn.*, 53, 3395–3398. 2

Hansen, A. E., Marteau, D., & Tabeling, P. (1998). "Two-dimensional turbulence and dispersion in a freely decaying system". *Phys. Rev. E.*, 58, 7261–7271. 5, 109

Hart, J. E. (2000). "A note on nonlinear correction to the Ekman layer pumping velocity". *Phys. Fluids*, 12, 131–135. 54

van Heijst, G. J. F. & Clercx, H. J. H. (2009a). "Laboratory modelling of geophysical vortices". *Ann. Rev. Fluid Mech.*, 41, 143–164. 6

van Heijst, G. J. F. & Clercx, H. J. H. (2009b). "Studies on quasi-2D turbulencethe effect of boundaries". *Fluid Dyn. Res.*, 41, 064002–1–18. 5, 13, 14

Hopfinger, E. J. (1982). "Turbulence and waves in a rotating tank". *Ann. Rev. Fluid Mech.*, 125, 505–534. 6, 55, 113

Hopfinger, E. J. & van Heijst, G. J. F. (1993). "Vortices in rotating fluids". *Ann. Rev. Fluid Mech.*, 25, 241–289. 24, 33, 56, 60, 67

Ishida, S. & Iwayama, T. (2006). "A comprehensive analysis of nonlinear corrections to the classical Ekman pumping". *J. Met. Soc. Jpn.*, 89, 839–851. 54

Jacquin, L., Leuchter, O., Cambon, C., & Mathieu, J. (1990). "Homogeneous turbulence in the presence of rotation". *J. Fluid Mech.*, 220, 1–52. 6

Jeong, J. & Hussain, F. (1995). "On the identification of a vortex". *J. Fluid Mech.*, 285, 69–94. 80, 86

Jirka, G. H. & Uijttewaal, W. W. J. (2004). "Shallow flows: a definition". In G. H. Jirka & W. W. J. Uijttewaal (Eds.), *Shallow flows*: Taylor and Francis. 28

Kellay, H. & Goldburg, W. I. (2002). "Two-dimensional turbulence: a review of some recent experiments". *Rep. Prog. Phys.*, 65, 845–894. 3, 5

Kellay, H., Wu, X. L., & Goldburg, W. I. (1995). "Experiments with tubulent soap films". *Phys. Rev. Lett.*, 74, 3975–3978. 4

Kenjereš, S. (2008). "Electromagnetic enhancement of turbulent heat transfer". *Phys. Rev. E*, 78, 066309–1–5. 99

Klein, R., Pothérat, A., & Alferenok, A. (2009). "Experiment on a confined electrically driven vortex pair". *Phys. Rev. E*, 79, 016304–1–14. 102

Kloosterziel, R. C., Carnevale, G. F., & Orlandi, P. (2007). "Inertial instability in rotating and stratified fluids: barotropic vortices". *J. Fluid Mech.*, 583, 379–412. 56

Kloosterziel, R. C. & van Heijst, G. J. F. (1991). "An experimental study of unstable barotropic vortices in a rotating fluid". *J. Fluid Mech.*, 223, 1–24. 13, 16, 44, 50, 51

Kloosterziel, R. C. & van Heijst, G. J. F. (1992). "The evolution of stable barotropic vortices in a rotating free-surface fluid". *J. Fluid Mech.*, 239, 607–629. 6

Kraichnan, R. H. (1967). "Inertial ranges in two-dimensional turbulenc"e. *Phys. Fluids*, 80, 1417–1423. 1

Lacaze, L., Brancher, P., Eiff, O., & Labat, L. (2010). "Experimental characterization of the 3D dynamics of a laminar shallow vortex dipole". *Exp. Fluids*, 48(2), 225–231. 80, 95

Lamb, H. (1932). *Hydrodynamics, 6th ed.* Cambridge University Press. 80

Le Dizès, S. (2008). "Inviscid waves on a Lamb-Oseen vortex in a rotating stratified fluid: consequences for the elliptic instability". *J. Fluid Mech.*, 597, 283–303. 56, 62

Le Dizès, S. & Lacaze, L. (2005). "An asymptotic description of vortex Kelvin modes". *J. Fluid Mech.*, 542, 69–96. 56

Lilly, D. K. (1969). "Numerical simulation of two-dimensional turbulence" . *Phys. Fluids, S2,*, 12, 240–249. 1

Lin, J., Ozgoren, M., & Rockwell, D. (2003). "Space-time development of the onset of a shallow-water vortex". *J. Fluid. Mech.*, 485, 33–66. 79

Maas, L. R. M. (1993). "Nonlinear and free-surface effects on the spin-down of barotropic axisymmetric vortices". *J. Fluid Mech.*, 246, 117–141. 16

Maassen, S. R., Clercx, H. J. H., & van Heijst, G. J. F. (2003). "Self organization of decaying quasi-two-dimensional turbulence in stratified fluid in rectangular containers". *J. Fluid Mech.*, 495, 19–33. 3

Mattaeus, W. H. & Montgomery, D. C. (1980). "Selective decay hypothesis at high mechanical and magnetic Reynolds numbers". *Ann. N.Y. Acad. Sci.*, 357, 203–222. 2

Melander, M. V. & Hussain, F. (1994). "Core dynamics on a vortex column". *Fluid Dyn. Res.*, 13, 1–37. 56

Meshalkin, L. D. & Sinai, Y. G. (1961). "Investigation of the stability of a stationary solution of a system of equations for the plane movement of an incompressible viscous fluid". *J. Appl. Math. Mech (Prikl. Mat. Mekh.)*, 25, 1700–1705. 2

Morize, C., Moizy, F., & Rabaud, M. (2005). "Decaying grid-generated turbulence in a rotating tank". *Phys. Fluids*, 17, 095105–1–11. 6

Nakamura, Y. (1996). "Transition to turbulence from a localized vortex array". *J. Phys. Soc. Jpn.*, 65, 1666–1672. 110

Orlandi, P. & Carnevale, G. F. (1999). "Evolution of isolated vortices in a rotating fluid of finite depth". *J. Fluid Mech.*, 381, 239–269. 51

Paret, J., Marteau, D., Paireau, O., & Tabeling, P. (1997). "Are flows electromagnetically forced in thin stratified layers two-dimensional?". *Phys. Fluids*, 9, 3102–3104. 5, 85

Paret, J. & Tabeling, P. (1997). "Experimental Observation ot the two-dimensional Inverse Energy Cascade". *Phys. Rev. Lett.*, 79, 4162–4165. 5, 31, 126

Pedlosky, J. (1987). *Geophysical Fluid Dynamics.* Springer-Verlag, 2nd edition edition. 3, 6, 42, 44, 86, 113, 137

Ponomarev, V. M., Khapaev, A. A., & Yakushkin, I. G. (2009). "Vertical structure of the quasi-two-dimensional velocity field of a viscous incompressible flow and the problem of nonlinear friction". *Izv. Atmos. Oceanic Phys.*, 44, 45–52. 99, 110

Rossi, L., Vassilicos, J. C., & Hardalupas, Y. (2006). "Electromagnetically controlled multi-scale flows". *J. Fluid Mech.*, 558, 207–242. 99

Rutgers, M. A. (1998). "Forced 2D turbulence: Experimental evidence of simultaneous inverse energy and forward enstrophy cascades". *Phys. Rev. Lett.*, 81, 2244–2247. 4

Saffman, P. G. (1992). *Vortex Dynamics.* Cambridge University Press. 56, 67

Satijn, M. P., Cense, A. W., Verzicco, R., Clercx, H. J. H., & van Heijst, G. J. F. (2001). "Three-dimensional structure and decay properties of vortices in shallow fluid layers". *Phys. Fluids*, 13(7), 1932–1945. 5, 15, 17, 22, 28, 35, 40, 79, 82, 84, 85, 125

Shats, M. G., Xia, H., & Punzmann, H. (2005). "Spectral condensation of turbulence in plasmas and fluids and its role in low-to-high phase transitions in toroidal plasma". *Phys. Rev. E.*, 71, 046409–1–9. 5, 126

Sipp, D. & Jacquin, L. (2003). "Widnall instabilities in vortex pairs". *Phys. Fluids*, 15(7), 1861–1874. 56

Sipp, D., Jacquin, L., & Cossu, C. (2000). "Self-adaptation and viscous selection in concentrated two-dimensional vortex dipoles". *Phys. Fluids*, 12, 245–248. 82

Sivashinsky, G. I. & Yakhot, V. (1985). "Negative viscosity effect in large-scale flows". *Phys. Fluids*, 28, 1040–1042. 2

Smith, L. M. & Yakhot, V. (1993). "Bose condensation and small-scale structure generation in a random force driven 2D turbulence". *Phys. Rev. Lett.*, 71, 352–355. 1

Sommeria, J. (1982). "Why, how, and when, MHD turbulence becomes two-dimensional". *J. Fluid Mech.*, 118, 507–518. 4

Sommeria, J. (1986). "Experimental study of the two-dimensional inverse energy cascade in a square box". *J. Fluid Mech.*, 170, 139–168. 4

Sous, D., Bonneton, N., & Sommeria, J. (2004). "Turbulent vortex dipoles in a shallow water layer". *Phys. Fluids*, 16, 2886–898. 79, 80, 82, 83, 96

Sous, D., Bonneton, N., & Sommeria, J. (2005). "Transition from deep to shallow water layer: formation of vortex dipoles". *Eurpean J. Mech B/Fluids*, 24, 19–32. 15, 79, 82, 96

Staplehurst, P. J., Davidson, P. A., & Dalziel, S. B. (2008). "Structure formation in homogeneous freely decaying rotating turbulence". *J. Fluid Mech.*, 598, 81–105. 3, 6

Tabeling, P. (2002). "Two-dimensional turbulence: a Physicist Approach". *Phys. Rep.*, 362, 1–62. 2

Tabeling, P., Burkhart, S., Cardoso, O., & Willaime, H. (1991). "Experimental study of freely decaying two-dimensional turbulence". *Phys. Rev. Lett.*, 67, 3772–3775. 3, 5, 31, 99

Tabeling, P., Perrin, B., & Fauve, S. (1987). "Instability of a Linear Array of Forced Vortices". *Europhys. Lett.*, 3, 459–465. 4, 99, 110

Takaoka, M. (1989). "Stability of triangular cell flows". *J. Phys. Soc. Jpn.*, 58, 2223–2226. 2

Tenreiro, M., Zavala Sansón, L., van Heijst, G. J. F., & Trieling, R. R. (2010). "Experiments and simulations on self-organization of confined quasi-two-dimensional turbulent flows with discontinuous topography". *Phys Fluids*, 22, 025101–1–14. 113

Thess, A. (1992). "Instabilities in two-dimensional spatially periodic flows. Part I: Kolmogorov flow". *Phys. Fluids*, 4, 1385–1395. 3, 4, 99

Thomson, W. (1880). "Vibrations of a columnar vortex". *Philos. Mag.*, 10, 155–168. 13, 55, 59, 63, 65

Velasco Fuentes, O. U. (2009). "Kelvin's discovery of Taylor columns". *European J. Mech. - B/Fluids*, 28, 469–472. 3, 5

Voth, G. A., Haller, G., & Gollub, J. P. (2002). "Experimental measurements of stretching fields in fluid mixing". *Phys. Rev. Lett.*, 88, 254501–1–4. 99

Weiss, J. B. & McWilliams, J. C. (1993). "Temporal scaling behavior of decaying two-dimensional turbulence". *Phys. Fluids A*, 5, 608–621. 2

Wu, J., Ma, H., & Zhou, M. (2006). *"Vorticity and vortex dynamics"*. Springer. 80, 86

Zavala Sansón, L. & van Heijst, G. J. F. (2000). "Nonlinear Ekman effects in rotating barotropic flows". *J. Fluid Mech.*, 412, 75–91. 6, 16, 51, 54

Summary

Dynamics of shallow flows
with and without background rotation

Large-scale oceanic and atmospheric flows tend to behave in a two-dimensional way. To further understand such flows, a large scientific effort has been devoted to the study of perfect two-dimensional flows. For the last 30 years, there has been a large interest in experimentally validating the results from numerical and theoretical studies concerning two-dimensional flows, particularly two-dimensional turbulence and spatially periodic two-dimensional flows. Inspired by geophysical flows, experimentalists have used stratification, shallow fluid layer configurations, and background rotation to enforce the two-dimensionality of flows in the laboratory. However, as all these methods have shortcomings, it is difficult to achieve a perfectly two-dimensional flow in the laboratory.

The work presented in this thesis focuses on two of the common methods used to enforce the two-dimensionality of flows: the shallow layer configuration and background rotation. To further understand the effect of these methods on the two-dimensionality of flows, we studied the dynamics of generic elementary vortical structures in a shallow fluid layer with and without background rotation.

Through the analytical and numerical study of a decaying axisymmetric monopolar vortex, we revised the usual argument for considering shallow flows as two-dimensional. This argument is based on the continuity equation, and it states that the vertical velocity can be neglected if the ratio of vertical to horizontal length scales of the flow is small. By performing numerical simulations and a perturbation analysis for shallow flows, it was shown that this argument is not valid in general, and that the two-dimensionality of the flow does not depend exclusively on the aspect ratio. Instead, it also depends on the dynamics of the flow; particularly, a shallow flow behaves in a two-dimensional way if the flow evolution is dominated by bottom friction over the whole fluid depth. These results were supported by the numerical and experimental study of a more complex flow structure, namely a dipolar vortex, in a shallow fluid layer.

For the study of decaying dipolar vortices, numerical simulations were performed using a finite element code. The flow was initialized with a Lamb–Chaplygin dipolar vortex with a Poiseuille-like vertical profile, after which it was left to evolve

159

freely. The 3D structure of the vortex was obtained using the λ_2 vortex detection criterion. Using this tool, it was observed how the vortex is gradually distorted due to the secondary 3D motions. An experimental investigation of an electromagnetically forced dipolar vortex, where Particle Image Velocimetry (PIV) was used to calculate the velocity field in a horizontal cross-section of the flow, supports the numerically obtained results.

It is assumed that flows subjected to strong background rotation behave like two-dimensional flows due to the reduction of gradients in the direction parallel to the rotation axis, as stated by the Taylor–Proudman theorem. This phenomenon results in the formation of columnar structures. In the current work, it was found that the flow can behave in a two-dimensional way as long as the rotation rate is fast enough, irrespective of the aspect ratio. In other words, this is true even if the fluid depth is of the same order as the thickness of the Ekman boundary layer, for which case no columnar structures are formed. This is attributed to the linear coupling between primary and secondary motions.

From the study of decaying vortical structures, it was concluded that neither adding background rotation to a shallow flow nor decreasing the depth of a rotating flow necessarily increases the degree of two-dimensionality of the flow.

The last two chapters of this thesis are dedicated to the study of a shallow dipolar structure that is continuously driven by time-independent electromagnetic forcing. For a shallow structure without background rotation, it was observed that for weak forcing the flow can be considered indeed as two-dimensional. However, every shallow flow, even for very small fluid depths, becomes three-dimensional for a sufficiently high forcing magnitude. An equivalent result was obtained for a similar flow subjected to background rotation. The change in behavior is associated with a change in the vertical profile of the horizontal velocity, which is clearly absent in perfectly two-dimensional flow.

The results presented in this thesis confirm that under certain conditions shallow flows and flows subjected to background rotation can behave as a two-dimensional flow. However, more importantly, it is shown that there are clear limits to this behavior. This work presents a better understanding of the basic dynamics of shallow flows with and without background rotation and of the extent to which these flows can be considered as quasi-two-dimensional.

List of publications

This thesis is based on the following publications:

- *Scaling of decaying shallow axisymmetric swirl flows.* Duran-Matute, M., Kamp, L. P. J., Trieling, R. R., & van Heijst, G. J. F., *J. Fluid Mech.*, 648, 509–519 (2010). **(Chapter 3)**

- *Scaling of decaying shallow axisymmetric swirl flows subjected to background rotation.* Duran-Matute, M., Kamp, L. P. J., Trieling, R. R., & van Heijst, G. J. F., in preparation. **(Chapter 4)**

- *Inertial oscillations in a confined monopolar vortex subjected to background rotation.* Duran-Matute, M., Kamp, L. P. J., Trieling, R. R., & van Heijst, G. J. F., *Phys. Fluids*, 21, 116602 (2009). **(Chapter 5)**

- *Dynamics and structure of decaying shallow dipolar vortices.* Duran-Matute, M., Albagnac, J., Kamp, L. P. J., & van Heijst, G. J. F., accepted for publication in *Phys. Fluids*. **(Chapter 6)**

- *Scaling and asymmetry in an electromagnetically forced dipolar flow structure.* Duran-Matute, M., Trieling, R. R. & van Heijst, G. J. F., submitted to *Physical Review E*. **(Chapter 7)**

Acknowledgments

The path that led to this dissertation was full of hard work, problems, setbacks, and frustration, but most of all, it was full of surprises, smiles, laughter, and good times. Those good times and this dissertation would not have been possible without all the great people that have been part of my life in the past four years.

I would like to thank GertJan van Heijst for his advice and for always making me feel welcomed in his office for our discussions on fluid dynamics, this dissertation, scientific papers, the future, science, academics, etc. I am also very thankful to Leon Kamp and Ruben Trieling for their continuous help, support, and guidance. I have certainly learned a lot from all of them.

I thank the members of the doctoral core committee Leo Maas, Wim Uijttewaal, and Federico Toschi for their valuable comments, which are highly appreciated.

During the four years, I had the chance to collaborate with several colleagues. With Julie Albagnac, I worked on what is now Chapter 6 and a scientific publication. I really enjoyed the time we worked together both in Eindhoven and Toulouse, and I hope for similar times in the future. With Francisco Fontenele Araujo, I had long fruitful discussions through which I learned to see fluid dynamics in a different way. Some of these discussions served as an inspiration for Chapter 7. Finally, with Gabriella Di Nitto, I had the chance to work on the experiments described in Chapter 8. I hope lasers will not break down on Gabriella too often.

I would also like to thank Ad "The Magician" Holten for his help with the experiments. I am still amazed about how he can make everything work; it is just like magic. Thanks also to Gerald Oerlemans and Freek van Uittert for their help in building the experimental setup. I express my gratitude to Marjan for all her help with too many and varied problems, for the nice chats, and for the friendly feeling around the *secretariat*.

I would like to thank Willem van de Water for our discussions on fluid dynamics and his help in organizing the Talking About Fluid Dynamics sessions and the Fluid Dynamics seminar.

I thank also the people in Cascade who are responsible for the good environment at work and all the related academic/social activities. Thanks to Jurriën (my office-mate for almost four years), Alejandro, Andrzej, Anita, Anton, Ariel, Bas, Berend, Brigitte, Christian, Daniel, David, Devis, Elke, Evelyn, Ergün, Eric, Florian (Günther and Janoschek), Folkert, Geert, Gunes, Henny, Herman,

Jan (Lodewijk and Willems), Jørgen, Jos, Jens, Jemil, Laurens, Margit, Marleen, Mico, Mira, Neehar, Oleksii, Paul (Aben and Bleomen), Petra, Rudie, Raoul, Rafal, Richard, Rini, Rinie, Sebastian, Stefan, Theo, Valentina, Vincent, Werner, Yan, Zeinab.

Ik wil alle mensen die me een beetje Nederlands geleerd hebben, bedanken (in het bijzonder Jurriën, GertJan, Marjan, Ad en Gerald).

I had the opportunity to supervise three Master's theses. To Monique, Joost, and Judith, I wish the best, and I thank them for the unintentional lessons on fluid dynamics and life.

I acknowledge the support of the Mexican people, who made my stay in the Netherlands possible through a graduate scholarship from the CONACYT. I am grateful to Oscar Velasco Fuentes (CICESE, México) and Dr. Anatoliy Filonov (UdeG, México) for their support on my way to the Netherlands.

I thank Lesly García Chávez for teaching me how to measure the viscosity of the salt solution employed in the experiments described in Chapters 7 and 8. More importantly, I thank her together with Oscar for their friendship. I hope to see both of them in the Alps again .

Thanks to all my friends in Eindhoven for their friendship and support; fortunately you are too many to be named here, but you know who you are. Thanks to the Mexican community at the TUE, to the broader Latin American community (Colombians, Venezuelans, Bolivians, Peruvians, Chileans...), to all my friends from the other many nationalities (Italians, Turkish, Germans, French, Portuguese, US citizens, South Africans...), and obviously, to my Dutch friends. Special thanks to Carlos, Christina, Maria Gustaffson, Maria Eriksson, the Polish Dynamic Duo (Ola and Gosia), Armando, Can, Humberto, and Jorge. Thanks to all who came to the DJ30 dinners and parties. Thanks to the Aikidokas. I enjoyed very much sailing a catamaran in Texel. Muchas gracias Fer por tantas tantas sonrisas.

Finalmente agradezco a mi familia y amigos en México (y la Républica Checa). En especial agradezco a mis padres por su apoyo durante tantos años. Estoy seguro de que si no fuera por lo que ellos me enseñaron, no hubiera disfrutado tanto estos años. Termino esta tesis como empezó: dedicándola a mi hermana Inés y a mi hermano Octavio.

Curriculum vitae

April 19, 1981:   Born in Guadalajara, México

1999–2004:   B.Sc. in Physics
Universidad de Guadalajara
Guadalajara, México

2001–2002:   Visiting student
Physics Department
University of Washington
Seattle, U.S.A.

2004–2006:   M.Sc. in Physical Oceanography
CICESE
Ensenada, México

2006–2010:   Ph.D. candidate
Fluid Dynamics Laboratory
Eindhoven University of Technology
Eindhoven, The Netherlands